Optics-Based Quantum Information and Sensing Platforms Utilizing the Nitrogen-Vacancy Center in Diamond

Michael Gould

A dissertation
submitted in partial fulfillment of the
requirements for the degree of

Doctor of Philosophy

University of Washington

2016

Reading Committee:

Kai-Mei C. Fu, Chair

Lih Lin

Arka Majumdar

Program Authorized to Offer Degree:
Electrical Engineering

University of Washington

Abstract

Optics-Based Quantum Information and Sensing Platforms Utilizing the Nitrogen-Vacancy Center in Diamond

Michael Gould

Chair of the Supervisory Committee:
Assistant Professor Kai-Mei C. Fu
Physics and Electrical Engineering

The nitrogen-vacancy (NV) center is a point defect in the diamond crystal lattice, forming a localized-electron system with unique optical and spin properties. In particular, optical control and read-out of the spin state, combined with long spin coherence times, make it an attractive candidate for both high-sensitivity magnetometry and as a solid-state spin qubit for quantum information processing (QIP). This dissertation documents the design, implementation, and characterization of systems aimed at each of these applications.

First, the development of a GaP-on-diamond integrated photonics platform for QIP is presented. This work is motivated in part by the scalability advantages that are inherent to photonic device integration, and more fundamentally by the large potential improvements in performance. Specifically, coupling NV centers to integrated optical resonators should enable orders of magnitude improvement in entanglement generation rate through improved photon collection efficiency. This will be crucial for the development of even small-scale QIP systems, as NV-NV spin entanglement has so far only been demonstrated at rates far below the spin decoherence rate, effectively limiting NV-based QIP to two-qubit systems. Large numbers of integrated optical devices were fabricated, including optical resonators. Passive transmission measurements were performed on hundreds of individual devices, enabling statistical performance metrics and device yields to be extracted for several components.

Device-coupled single-photon measurements are also presented, indicating photon collection efficiencies as high as 9%, corresponding to an efficiency-limited entanglement rate far exceeding the best reported spin decoherence rate. These results put the GaP-on-diamond platform in a competitive position relative to other photonic integration efforts for QIP.

Next, a magneto-optical microscope for bio-sensing applications is presented. The microscope images photoluminescence emitted from a thin, dense sheet of NV centers within the top 200 nm of a diamond chip. Changes in the photoluminescence associated with the spin population of the defects allow for optically detected magnetic resonance (ODMR), with the resonant frequency depending on the local magnetic field. Two-dimensional images of the magnetic field at the surface of the diamond are thus obtained, with a magnetic field sensitivity of 2.4 μT. The microscope was able to detect magnetic-field disturbances due to the presence of single 19-nm-diameter super-paramagnetic nanoparticles (SPNs) in wide-field ODMR images taken at room temperature. This is the first demonstration of wide-field detection of individual sub-μm magnetic particles under ambient conditions, and should enable a new class of biological imaging and sensing systems based on SPN labels.

TABLE OF CONTENTS

LIST OF FIGURES

ACKNOWLEDGMENTS

This material is based upon work supported by the National Science Foundation under Grant Number 1506473. I would like to thank Ian R. Christen and Maya Dunn for assistance with graphics; Ian R. Christen, Srivatsa Chakravarthi and Emma Schmidgall for device testing; Yaxuan Zhou and Seth Hyra for FDTD simulations; Fariba Hatami and Minjoo Larry Lee for providing epitaxial GaP samples; and Rick Bojko for e-beam lithography support. Devices were fabricated at the Washington Nanofabrication Facility, a part of the National Nanotechnology Coordinated Infrastructure network.

DEDICATION

To my dearest parents, Lynn and Allin, without whom none of this would have been possible.

Part I

GAP-ON-DIAMOND INTEGRATED PHOTONICS FOR QUANTUM INFORMATION PROCESSING

Chapter 1

INTRODUCTION

1.1 The Nitrogen-Vacancy Center in Diamond

The nitrogen-vacancy (NV) center is a point defect in diamond consisting of a substitutional nitrogen atom and a vacancy occupying nearest-neighbor lattice sites (see Fig.1.1(a)). Two charge states are known to exist with ground-state energy levels within the bandgap of diamond: neutral (NV^0) and negatively charged (NV^-) [1–4]. A third, positive charge state (NV^+) has been observed, though its ground-state energy is not known [1,5]. The preferred charge state of an NV center is determined by the local Fermi level [2,4,5]. The charge state of interest for the work presented in this dissertation is NV^-, and for the remainder of this document NV centers can be assumed to be negatively charged unless otherwise specified.

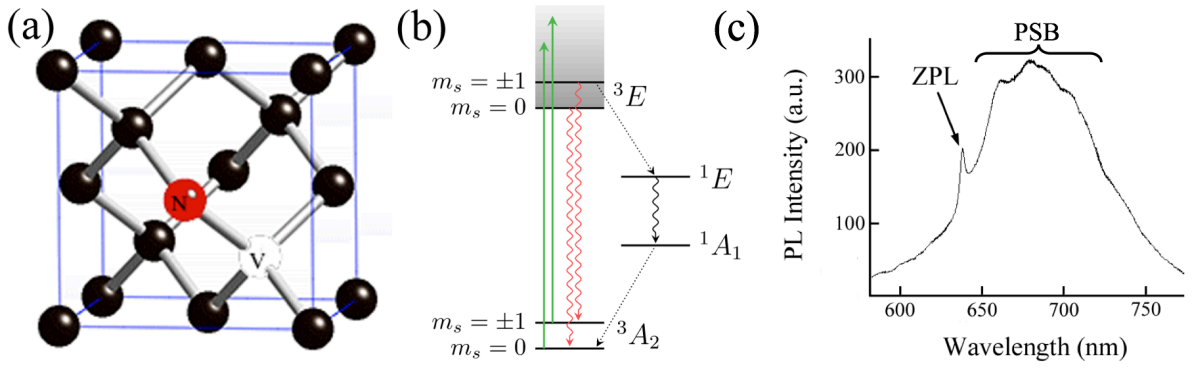

Figure 1.1: (a) Schematic of crystal defect structure of an NV center. (b) Energy-level diagram for the negatively charged NV center (NV^-), showing phonon-sideband excitation and zero-phonon emission. (c) Photoluminescence spectrum of an NV center taken at room temperature, with zero-phonon line (ZPL) and phonon sidebands (PSB) indicated.

NV centers can be viewed as a localized two-electron (or two-hole) system with C_{3v}

symmetry, whose energy-level diagram is illustrated in Fig. 1.1(b). The ground state of the system is a spin-triplet ($^3A_2$) for which the $m_s = \pm 1$ spin states are degenerate under zero applied magnetic field, and split from the $m_s = 0$ spin state by an energy $E_{ss} \approx 12$ μeV due to spin-spin interaction [6–9]. This spin-spin interaction is significantly reduced for the excited state spin-triplet (^3E), resulting in spin-dependent optical transition energies with energy difference $\Delta E \approx \frac{1}{2}E_{ss}$. Two singlet states ($^1A_1$, ^1E), with energies between those of the ground and excited spin-triplets, give rise to a non-spin-conserving decay path from the $m_s = \pm 1$ excited triplet state to the $m_s = 0$ ground state [10].

The combination of spin-dependent optical transitions and an asymmetric non-spin-conserving decay path enables both optical pumping and optical read-out of the spin state. By resonantly addressing the $m_s = \pm 1$ zero-phonon optical transition with continuous-wave (CW) excitation, the system can be initialized to the $m_s = 0$ ground state, with an experimentally demonstrated fidelity of 99.7% and an initialization time of only a few microseconds. By resonantly addressing the $m_s = 0$ cycling transition and monitoring emission, the spin state can be measured with a fidelity of 93% and read-out time of 40 μs [11]. Together with a microwave (MW) magnetic field resonant on the ground-state spin transition, these functionalities allow for complete control and accurate measurement of the NV center spin state. Additionally, ground-state spin coherence times exceeding 1 ms at room temperature [12], and approaching 1 s at cryogenic temperatures [13] have been demonstrated. The unique combination of optical spin initialization and read-out with long spin coherence times has led to the NV center in diamond being one of the best studied solid-state defects, both for sensing applications as well as quantum information processing (QIP). The latter is the focus of the remainder of Part I, while Part II is focused on magnetic sensing.

1.2 Measurement-Based Quantum Information Processing with NV Centers

The NV center in diamond shows significant promise as a solid-state qubit register [14–16] for measurement-based quantum information processing (MBQIP) [17–19]. The computational resource in MBQIP is a network of entangled qubit registers known as a cluster state [17].

Cluster states can be schematically represented as an array of nodes connected by edges (Fig. 1.2(a)), with each node representing a quantum register and each edge representing an entanglement operation between the connected nodes [18].

Cluster states can in principle be grown by sequentially performing controlled-phase operations on selected pairs of nodes, with all nodes initially prepared in a superposition state [20]. However in real systems there is a non-zero probability of damaging the existing state at each entanglement operation, which can significantly impede growth. This limitation can be overcome by using 'brokered' cluster state generation (Fig. 1.2(b)), wherein each node is composed of two qubits: a client and a broker [21]. NV centers are ideal candidates for the implementation of 'brokered' cluster state generation, as each defect contains a ^{14}N nuclear spin in addition to the electron spin described in Section 1.1. Experimental state swapping between the electron spin (broker) and nuclear spin (client) has been demonstrated, enabling electron-mediated optical read-out of the nuclear spin [11], room-temperature spin coherence exceeding 1 s [22], room-temperature spin entanglement [23], and coherence-protected quantum gates [24, 25].

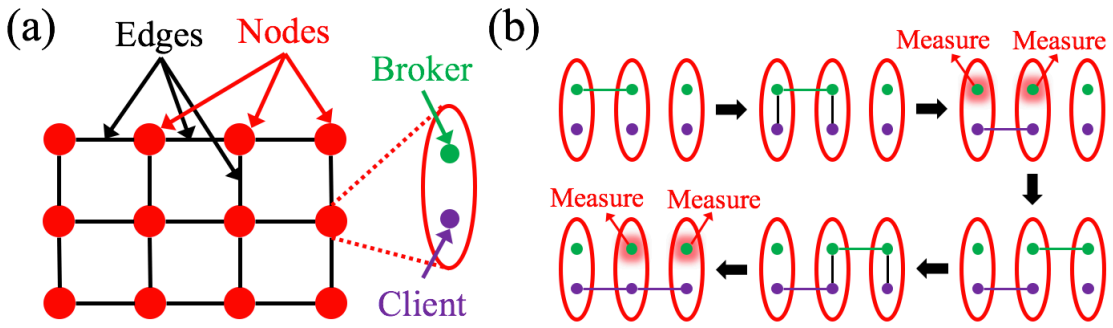

Figure 1.2: (a) Illustration of a cluster state. Inset: Nodes can be made up of multiple qubits, in this case 2, allowing for brokered cluster state generation. (b) Illustration of brokered 3-qubit cluster state generation: individual edges are first created between the brokers before being transferred to the clients through single-qubit measurement.

For NV centers, individual cluster-state edges (NV-NV electron spin entanglement) can be

created via single-photon measurement of zero-phonon-line (ZPL) emission from the selected nodes [18, 26]. This procedure makes use of the NV center's spin-selective optical transitions to first generate spin-photon entanglement at the individual nodes (Fig. 1.3(a)). To do this, two NV centers are initialized to the $m_s = 0$ ground state, which we will write as $\psi = |\downarrow\rangle$. A subsequent MW $\pi/2$-pulse resonant with the ground-state spin transition prepares each NV center in a spin superposition state $\psi = \frac{1}{\sqrt{2}}(|\downarrow\rangle + |\uparrow\rangle)$, where $\downarrow$ and $\uparrow$ represent the $m_s = 0$ and $m_s = 1$ spin states respectively. Resonant excitation of the $m_s = 0$ optical transition with an optical π-pulse then results in spin-conditional spontaneous emission, and the spin state of each NV center is entangled with photon-number in an associated optical mode. We will refer to the optical modes associated with individual NV centers as collection modes. The spin-photon entangled state for each single-center system is $\psi = \frac{1}{\sqrt{2}}(|\downarrow 1\rangle + |\uparrow 0\rangle)$, where 0 and 1 represent photon-number states in the collection mode. The state of the combined system is thus

$$\begin{aligned}\Psi &= \frac{1}{2}\Big(\Big(|\downarrow 1\rangle + |\uparrow 0\rangle\Big) \otimes \Big(|\downarrow 1\rangle + |\uparrow 0\rangle\Big)\Big) \\ &= \frac{1}{2}\Big(|\downarrow\downarrow 11\rangle + |\downarrow\uparrow 10\rangle + |\uparrow\downarrow 01\rangle + |\uparrow\uparrow 00\rangle\Big). \end{aligned} \tag{1.1}$$

Interference of the collection modes on a beam-splitter results in a rotation of the single-photon measurement basis: eigenstates of the beam-splitter output-mode photon-number operators ($\hat{n}_1$ and $\hat{n}_2$) are superpositions of collection-mode number states. We will refer to the beam-splitter output modes simply as output modes. Collection modes and output modes are represented in Fig. 1.3(b) by red arrows pointing into and away from the beam-splitter, respectively. To make the rotation of the measurement basis clear, we can write out the matrix-form of the output-mode photon-number operator $\hat{n}_1$ in the collection-mode number-state basis, for the $\langle n_{tot}\rangle \leq 1$ sub-space:

$$\hat{n}_1 = \frac{1}{2}\begin{bmatrix} 0 & 0 & 0 \\ 0 & 1 & -i \\ 0 & i & 1 \end{bmatrix}, \tag{1.2}$$

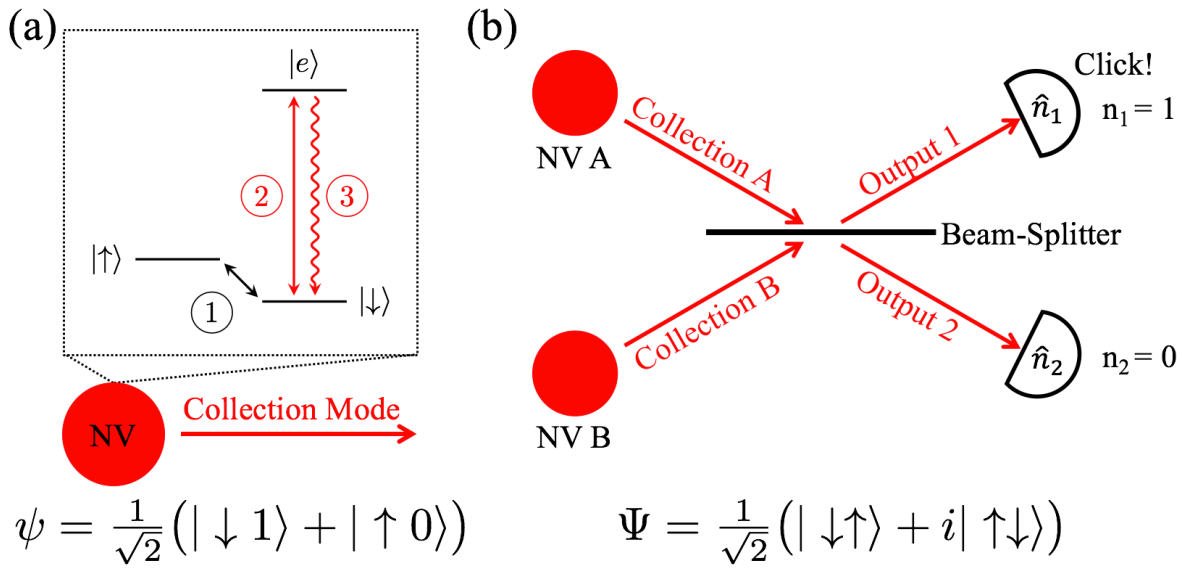

Figure 1.3: (a) Illustration of procedure for single-NV spin-photon entanglement generation, assuming initialization to the $m_s = 0$ ground state. 1: An RF $\pi/2$-pulse resonant on the ground-state spin transition results in spin superposition state. 2: A spin-selective optical π-pulse resonant on the $m_s = 0$ optical transition results in 3: spin-conditional spontaneous emission, and thus a spin-photon entangled state. (b) Illustration of spin-spin entanglement generation between two NV centers, each already prepared in the spin-photon entangled state shown in (a). Interfering the collection modes associated with each emitter on a balanced beam-splitter rotates the photon-number measurement basis, and a subsequent single-photon detection event in either output mode yields a spin-spin entangled state.

where the relevant collection-mode number-states are $\{|00\rangle, |01\rangle, |10\rangle\}$. Solving for the eigenvalues and eigenvectors of this matrix, we have:

$$\phi_1 = |00\rangle, n_1 = 0$$

$$\phi_2 = \frac{1}{\sqrt{2}}\left(|01\rangle - i|10\rangle\right), n_1 = 0$$

$$\phi_3 = \frac{1}{\sqrt{2}}\left(|01\rangle + i|10\rangle\right), n_1 = 1. \tag{1.3}$$

Within the $\langle n_{tot}\rangle \leq 1$ sub-space, detection of a single photon in output mode 1 projects the spin-state of the system onto the ϕ_3 sub-space, resulting in the destruction of spatial 'which-

path' information. Similarly, a single photon detected in output mode 2 projects the spin-state onto the ϕ_2 sub-space. Re-writing Eq. 1.1 in terms of the output-mode measurement-basis states from Eq. 1.3, we obtain

$$\Psi = \frac{1}{2}\left(|\downarrow\downarrow\rangle \otimes |11\rangle + |\uparrow\uparrow\rangle \otimes \phi_1 + \frac{i}{\sqrt{2}}\Big((|\downarrow\uparrow\rangle + i|\uparrow\downarrow\rangle) \otimes \phi_3 + (|\downarrow\uparrow\rangle - i|\uparrow\downarrow\rangle) \otimes \phi_2 \Big) \right). \tag{1.4}$$

From Eq. 1.4 it can be seen that in an ideal system, detection of a single photon in either (but not both) of the beam-splitter output modes leaves the NV centers in a spin-entangled state $\Psi = \frac{1}{\sqrt{2}}(|\downarrow\uparrow\rangle \pm i|\uparrow\downarrow\rangle)$. However, for lossy systems and/or non-photon-number-resolving detectors this entanglement is only partial, due to a remaining $|\downarrow\downarrow\rangle$ component associated with the possibility of a second, undetected photon. In this case, the combined spin-state of the system after a single photon-detection event is

$$\Psi = \frac{1}{\sqrt{2+\alpha^2}}(|\downarrow\uparrow\rangle \pm i|\uparrow\downarrow\rangle - i\alpha|\downarrow\downarrow\rangle), \tag{1.5}$$

where α depends on the probability of a photon going undetected. A subsequent spin-flip operation followed by a second single-photon detection event at either output will project out this undesired component, leaving the system in a maximally entangled state

$$\Psi = \frac{1}{\sqrt{2}}(|\downarrow\uparrow\rangle \pm |\uparrow\downarrow\rangle). \tag{1.6}$$

Thus spin-spin entanglement generation in a real system relies on two independent photon detection events. A more rigorous description of this protocol can be found in Ref. [18].

Spin-spin entanglement between two NV centers has been heralded in this manner using free-space collection optics [27–29]. However, the demonstrated entanglement generation rate was significantly slower than the electron spin decoherence rate, and thus far too slow to allow multi-qubit entanglement. The limiting factor in reported entanglement rates is the low probability of detecting a ZPL photon upon excitation of an NV center. We will call this probability the total quantum efficiency, η. Because successful entanglement is heralded by two independent ZPL photon detection events [30], the entanglement generation rate scales as η^2. Low achieved η values are primarily the result of two effects inherent to NV

centers in diamond. First, the high refractive index of diamond limits free-space collection efficiency through total internal reflection. Second, phonon interactions result in only ∼3% of radiative emission occurring via the ZPL transition [31–33], as shown in Fig. 1.1(c). The remaining 97% of photons are emitted in the phonon sidebands (PSB), and cannot be used for entanglement generation. Photonic device integration can mitigate both effects, and may provide a scalable platform for building quantum networks.

1.3 GaP-on-Diamond Integrated Photonics for High Entanglement Rates

In this work we demonstrate a key step toward realizing a quantum network in a GaP-on-diamond integrated photonics platform: the efficient optical coupling of single NV centers to single-mode waveguides. We show that the probability of emitting a ZPL photon into the guided mode after optical excitation can reach 9% [34]. This represents an order of magnitude improvement over achieved efficiencies into free-space collection optics using solid-immersion lenses (SILs) [35], and nearly two orders of magnitude improvement over the achieved efficiencies in reported entanglement generation work [28]. Furthermore, the photon collection devices were fabricated on the same chip as large numbers of passive integrated photonic components necessary for on-chip entanglement generation networks [36]. Combined, these results indicate the promise of the GaP-on-diamond platform for scalable quantum networks.

Fig. 1.4 shows a proposed integrated entanglement generation circuit for which several of the component parts have been individually demonstrated as part of this work. The circuit is composed of two resonant photon-collection devices, each coupled to a separate waveguide. Waveguide modes act as the collection modes for spin-entangled photons shown in Fig. 1.3(b). Collection-mode interference is performed on-chip, and single-photon detection can be implemented either on-chip, as illustrated on the left-hand side of the circuit, or off-chip by means of grating couplers.

Our platform utilizes a 125 nm thick GaP membrane to guide optical modes at the surface of the diamond chip [31, 36], taking advantage of the high refractive index of GaP (n = 3.3) compared to that of diamond (n = 2.4) (see Fig. 1.5(a)). This is in contrast to the more com-

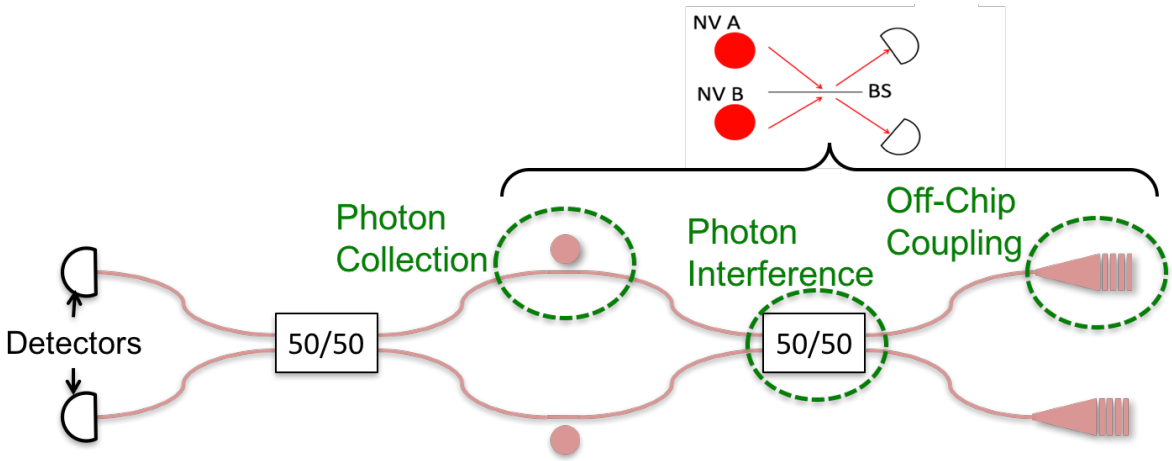

Figure 1.4: Diagram of proposed integrated entanglement generation circuit, showing both on-chip detection and grating couplers for off-chip detection. Elements circled in green have been individually demonstrated as part of this work.

mon approach utilizing the diamond itself as the waveguiding material [37]. A key advantage of the hybrid platform is fabrication scalability. Specifically, diamond waveguides require either undercutting of the diamond [38,39] or working with thin diamond membranes on a low index substrate [40, 41]. Undercutting requires a three-dimensional dry etch, significantly constraining the device layout. Thin diamond membranes with large area and uniformity have yet to be demonstrated, resulting in poor device uniformity across a chip. On the other hand, large-area (cm-scale) highly uniform GaP membranes can be grown epitaxially and transferred to bulk single-crystal diamond chips, enabling the fabrication of large numbers of photonic devices with good cross-chip uniformity. For complex photonic circuits, additional features of the GaP-on-diamond platform include the introduction of a second-order optical non-linearity [42], which should enable active photonic routing, and sub-nm top-surface roughness suitable for the development of on-chip superconducting nanowire single-photon detectors [43–45]. The primary disadvantage associated with the hybrid-material platform is the inherently weaker coupling between the emitters located in the diamond and the guided optical modes primarily localized in the GaP (see Fig. 1.5). However, as we demonstrate in

Chapter 5, this effect is mitigated with resonant devices of sufficiently high quality factor. Specifically, we make use of the fundamental transverse-electric (TE)-polarized whispering-gallery mode of 1.3-μm-diameter disk resonators to efficiently couple near-surface NV centers to single-mode waveguides. Demonstrated efficiencies are higher than what has been demonstrated in all-diamond waveguide-coupled devices, and exceed the theoretical limit for free-space collection by nearly an order of magnitude.

The remainder of Part I is organized as follows: Chapter 2 details the current fabrication process for the GaP-on-diamond platform, including key improvements made by the author; Chapter 3 describes the design methodology used for several key photonic components; Chapter 4 presents large-scale transmission measurement results for fabricated components; Chapter 5 presents single-photon measurements for several individual device-coupled NV centers; and Chapter 6 discusses the outlook for the future of the GaP-on-diamond platform.

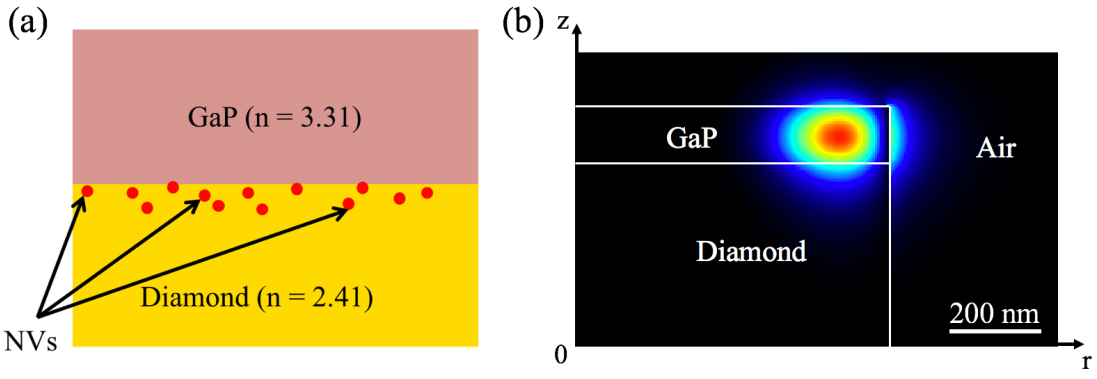

Figure 1.5: (a) Schematic cross-section of device layers. (b) Plot of radial electric field component (E_r) for fundamental TE-polarized whispering gallery mode in a 1.3-μm diameter GaP-on-diamond disk.

Chapter 2

FABRICATION PROCESS

In this chapter, we detail the fabrication process used to realize devices in the GaP-on-diamond platform. Section 2.1 gives an overview of the entire process flow from initial materials through final devices, and Section 2.2 details several key improvements over previous work.

2.1 Process Overview

Device chips were fabricated using a process based on doctoral work from a former student in our research group [46, 47]. NV centers were created approximately 15 nm below the surface of a 2 mm × 2 mm commercially available electronic grade diamond chip (Element6) by ion implantation (CuttingEdge Ions) and annealing. A first anneal at 850°C in 95%/5% Ar/H_2 forming gas allowed for vacancies to diffuse, resulting in the formation of NV centers and removal of crystal damage. A subsequent low-temperature anneal at 450°C was performed to promote the desired negatively charged NV^- state for the implanted NV centers by raising the surface Fermi level [48]. The diamond was then cleaned with a solution of KNO_3 in fuming H_2SO_4 and treated with hexamethyldisilazane (HMDS) vapor, resulting in a clean hydrophobic top surface.

Separately, a 300 nm thick $Al_{0.8}Ga_{0.2}P$ sacrificial layer and 125 nm thick GaP top layer were epitaxially grown on a single-crystal GaP substrate (Fariba Hatami, Humboldt-Universität zu Berlin). A 1.5 mm × 1.5 mm square membrane with an array of etch vias was defined by contact optical lithography. Reactive ion etching (RIE) was used to etch through both the top GaP layer and the sacrificial layer, exposing the $Al_{0.8}Ga_{0.2}P$ to the environment, both around the membrane perimeter as well as within the etch vias. The membrane was

released via wet etching in a 1.5% hydrofluoric acid (HF) solution in water, and transferred to the cleaned and treated diamond surface (Fig. 2.1).

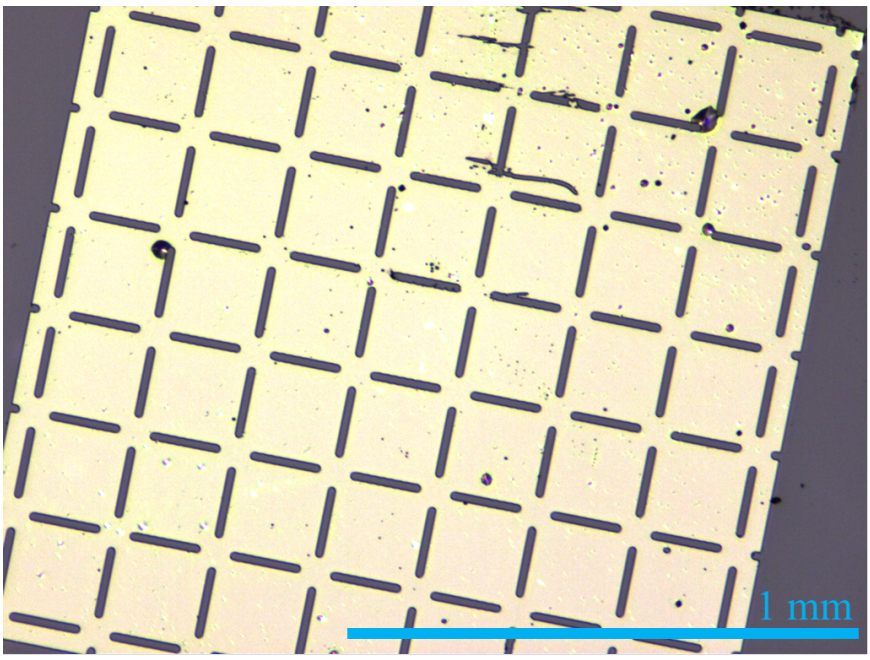

Figure 2.1: Optical microscope image of transferred GaP membrane (yellow) on diamond chip (dark background). Etch vias used for release from native substrate are visible as regularly spaced dark lines defining 200 μm squares.

The resulting chip (GaP-on-diamond) was then patterned via electron-beam lithography, using hydrogen silsesquioxane (HSQ) as a negative resist. A $Cl_2/N_2/Ar$ RIE step was performed to etch through the GaP, followed by an O_2 RIE step to etch approximately 600 nm into the diamond substrate. The resulting device cross-section consists of the 125 nm GaP layer on top of a 600 nm diamond pedestal, with a sparse layer of near-surface NV centers within $\sim$15 nm of the GaP-diamond interface. A schematic of the full process flow is shown in Fig. 2.2 and detailed step-by-step fabrication recipes can be found in Appendix B.

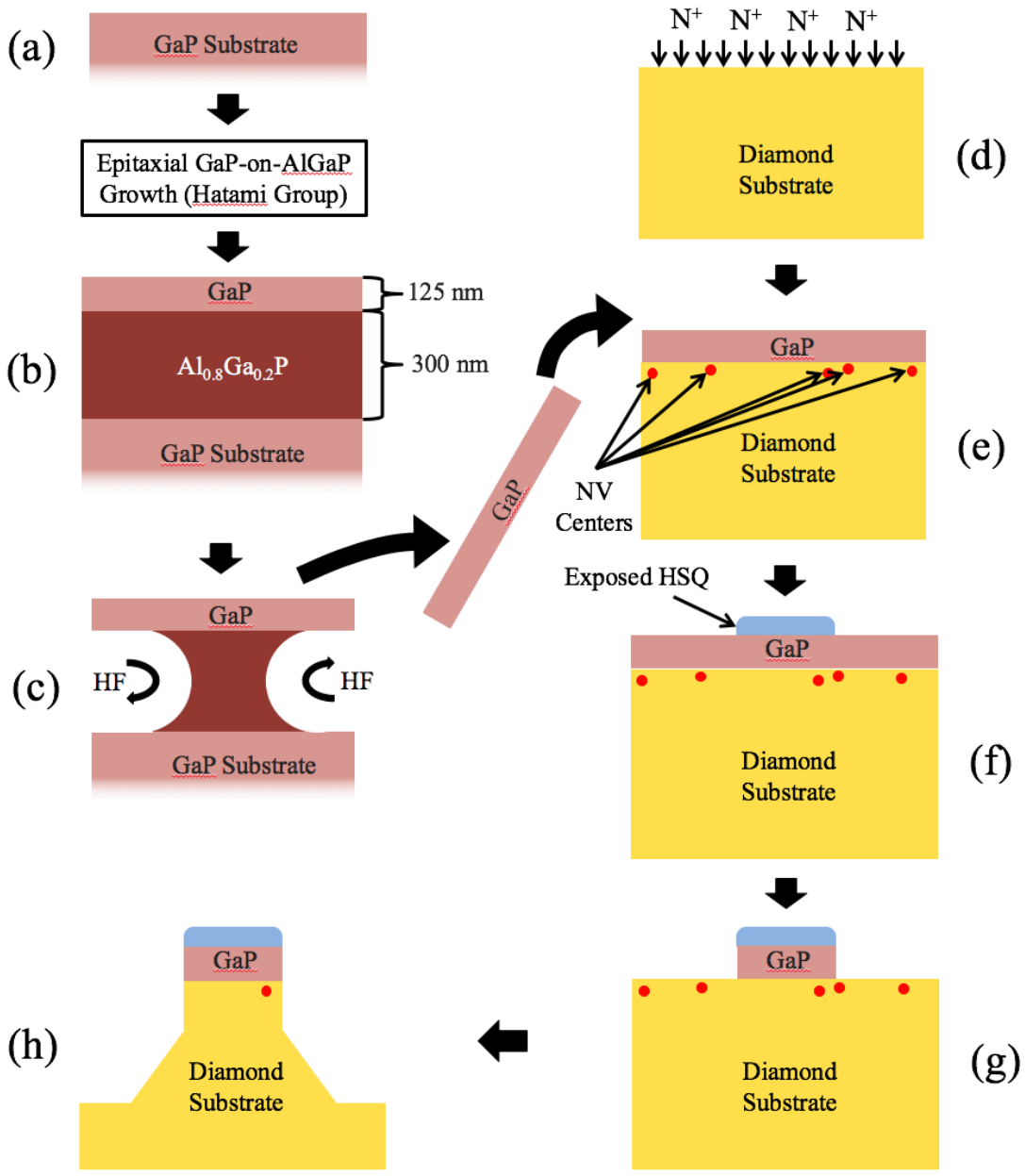

Figure 2.2: Schematic flow chart for full fabrication process. (a) Initial commercially available single-crystal GaP substrate. (b) GaP-on-$Al_{0.8}Ga_{0.2}P$ epitaxially grown on GaP substrate. (c) HF wet etching of sacrificial $Al_{0.8}Ga_{0.2}P$ layer to release top GaP membrane. (d) Initial electronic grade single-crystal diamond chip, implanted with N^+ ions to create near-surface NV centers. (e) GaP membrane transferred and van der Waals bonded to diamond chip. (f) Device pattern defined by electron-beam lithography using HSQ as resist. (g) GaP etched by $Cl_2/Ar/N_2$ RIE. (h) Diamond etched by O_2 RIE. Not shown: GaP membrane definition by optical lithography and RIE; diamond annealing to convert implanted N to NV centers.

2.2 Process Improvements

Though the fabrication process had largely been established prior to the work described in Part I of this dissertation, several key improvements over prior work [46, 47] were implemented. These improvements included modifying the GaP RIE to remove a problematic lateral etch bias, the identification of a plasma-enhanced chemical vapor deposition (PECVD) step as the cause of NV charge state switching, and the fabrication of simple tools to improve the GaP membrane transfer. Details are included in the following sub-sections.

2.2.1 GaP Etch Development

A key step in the fabrication process is the GaP etch. Initial fabrication rounds made use of a previously developed etch recipe. However, increased levels of design in more recent devices made apparent a crucial limitation of the original etch: significant lateral etch bias. Figure 2.3 shows a patterned grating after the GaP etch, with lateral dimensions reduced by approximately 20 nm on all sides compared to the lithography.

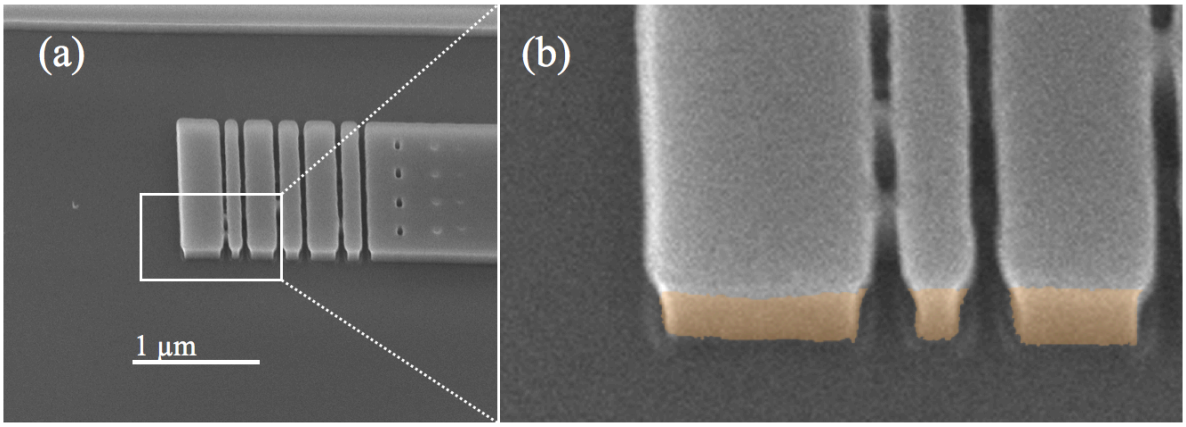

Figure 2.3: (a) SEM image of GaP-etched grating coupler on un-etched diamond showing ∼20 nm of lateral etch bias. (b) Digital zoom of 3 first grates of the grating, with false-color highlighting applied to GaP.

This caused many devices to work very differently than designed (or not to work at

all). Perhaps most crucially, coupling regions between disk resonators and bus waveguides were designed with very narrow sections of waveguide (see Figs. 3.2(a) and 4.1(a)). When subjected to 20 nm of etch bias on either side, these waveguides approach the cut-off condition for the fundamental TE mode and thus start to exhibit high optical losses into the substrate. While the bias could be accounted for in the pattern design, doing so would increase the minimum achievable spacing from ∼40 nm to ∼80 nm, a significant limitation. There is thus a strong motivation to remove the lateral etch bias from the process.

The original etch recipe parameters are listed in Table 2.1 under Recipe 1. SEM images of test structures (500 nm posts) in bulk GaP are shown in Fig. 2.5(a), resulting from 90 s of etching with the original recipe. The undercutting of the etch is clearly apparent in this image, suggesting either an isotropic component of the etch or non-normal angle of incidence for incoming ions. In the case of etch isotropy, the amount of undercutting should depend on the character of the etch (mechanical vs. chemical). We therefore attempted to alter the etch character in two ways: by varying the ratio of inductive (ICP) to capacitive (RF) power (Recipes 2 and 3), and by varying the relative flow rates of Cl_2 and Ar (Recipes 4 and 5).

Though recipes 1-5 showed significant differences in etch rates, all showed similar sidewall angle. Based on this result, it is likely that undercutting is a result of angular distribution in incident ions. Unfortunately there is no simple way to reduce this angular spread using the parameters available on the etching system. However, inspired by promising results with GaAs [49, 50], we hoped that the addition of N_2 to the etch chemistry would help to protect etched sidewalls with a thin passivating layer of GaN. Indeed, nearly vertical and much smoother sidewalls are obtained after 120 s of etching with Recipe 6, as can be seen in Fig. 2.5(b). All devices for which results are presented in Chapters 5 and 4 were fabricated using the N_2-added etch (Recipe 6). It is worth noting that while far more recipes were tested than those presented in Table 2.1, only two N_2-added recipes were tested. It is therefore likely that further optimization is possible. In particular it may be worth attempting to increase the etch rate, and even smoother sidewalls may be possible.

Recipe #	**1**	2	3	4	5	**6**
Chiller Temp (°C)	**10**	10	10	20	20	**20**
He Backing Pressure (Torr)	**2.0**	2.0	2.0	2.0	2.0	**3.0**
Chamber Pressure (mTorr)	**3.0**	3.0	3.0	3.0	3.0	**3.0**
Cl_2 Flow (sccm)	**1.0**	1.0	1.0	0.5	2.0	**1.0**
Ar Flow (sccm)	**9.5**	9.5	9.5	10.0	8.5	**6.0**
N_2 Flow (sccm)	**0**	0	0	0	0	**3.0**
ICP Power (W)	**55**	30	60	60	60	**60**
RF Power (W)	**72**	210	20	40	40	**50**
DC Bias (V)	**275**	530	120	170	170	**230**

Table 2.1: Summary of selected GaP etch test recipes.

2.2.2 Oxide Deposition

An outstanding issue with the original process flow was the effect of fabrication on the charge state of near-surface NV centers. It was known that near-surface NV centers were mostly in the desired negatively charged state (NV^-) at the beginning of the process. However, after fabrication they were mostly in the undesired neutral charge state (NV^0). By taking spectra after selected processing steps, the cause of this was identified as a PECVD oxide deposition step used to promote adhesion of the HSQ electron-beam resist. One possible reason for this effect is H^+ ions changing the surface termination of the diamond, thereby changing the charge state of near-surface NV centers [4]. H^+ ions would have been present in the deposition chamber due to the precursor silane (SiH_4). Replacing PECVD deposition with electron-beam evaporation of SiO_2 led to a much higher percentage of PL from the desired charge state through the end of the fabrication process. Figure 3.3(a) shows estimated charge state ratios for near-surface NV centers after different processing steps for a given sample. Estimates were obtained by comparing the maximum intensity of the zero-phonon

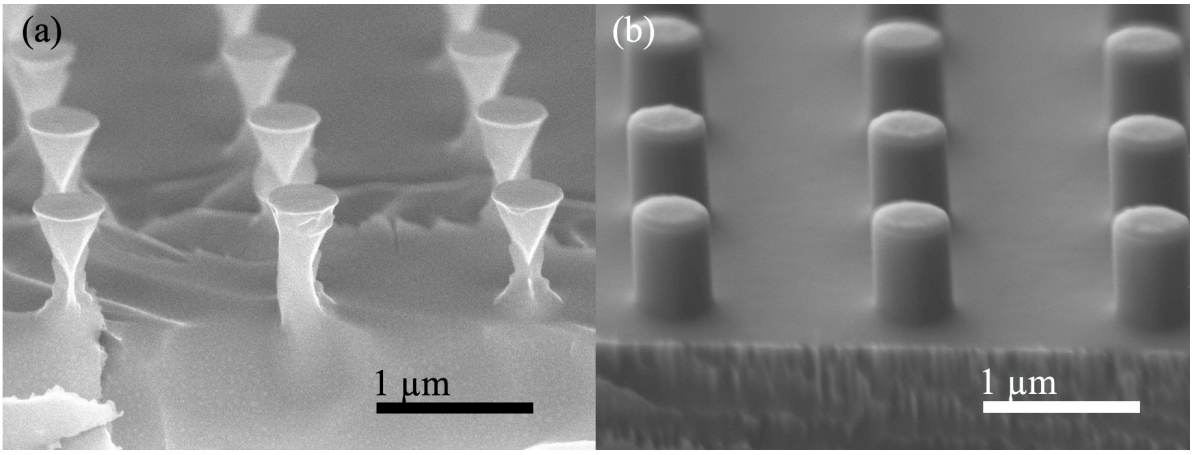

Figure 2.4: (a) SEM image of 500 nm posts etched in bulk GaP, after 90 s of Recipe 1. (b) SEM image of the same lithographic pattern, but after 120 s of Recipe 6.

lines (ZPLs) associated with each charge state, shown in Figure 3.3(b). Steps are shown in chronological order. The oxide deposition steps are labeled as 'PECVD' and 'Evap'. Note that the desired charge state can be recovered with a H_2SO_4/KNO_3 clean after PECVD oxide deposition, supporting the theory that the effect of the PECVD is caused by a change in surface termination. Interestingly, the effect of the PECVD step was observed for areas protected by a GaP membrane, as well as areas of bare diamond. This suggests that at the process temperature of 350° C, H^+ ions are able to diffuse through ∼130 nm of solid GaP on timescales of only a few seconds.

2.2.3 GaP Membrane Transfer

One of the lowest-yield process steps in the initial fabrication flow was the transfer of the GaP membrane to the diamond chip, with a success rate between ∼25% and ∼33%. Furthermore, even transfers that were considered successful typically resulted in some damage to the membranes. The primary reason for these problems was that the transfer of the released membrane from the wet etch (HF) bath to a water bath, as well as the final transfer to the diamond chip, were both done by hand with tweezers. As a first step in improving the yield,

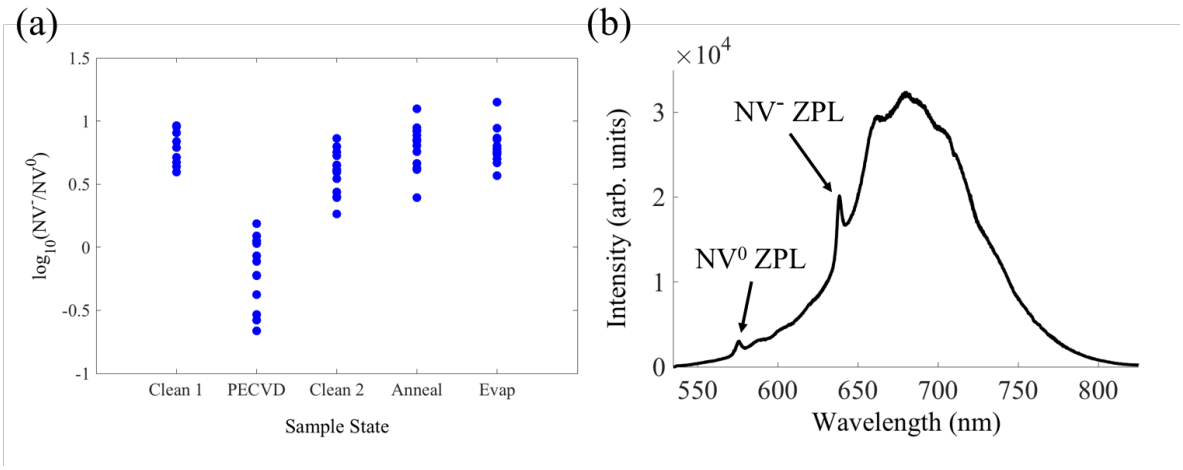

Figure 2.5: (a) Log-scale plot of the charge state ratio of ensembles of near-surface NV centers after different processing steps. Steps are shown in chronological order. (b) Ensemble photoluminescence spectrum showing ZPLs associated with both negatively-charged (NV^-) and neutral (NV^0) NV centers.

quality, and repeatability of the transfer process, we designed and fabricated two 'bucket' tools to allow for both transfers to be accomplished without having the membrane come into contact with any solid surfaces. The principle was to use bucket-shaped tools made of hydrophilic material which would partially drain when dipped into and lifted out of water (or dilute HF). This would allow a released membrane to be captured by the tool, with a small amount of remaining liquid. The hydrophilic nature of the tool material would ensure the floating membrane would not come into direct contact with the tool, as illustrated in Fig. 2.6(a).

The tool described thus far is enough to allow for safe transfer of a released membrane from the wet etch bath to a water bath (Fig. 2.6(b)). In order to enable the final transfer of the membrane to the diamond chip from the water bath, a mechanism for clamping the diamond into the bottom of the tool was included, as well as a mechanism to completely drain the bucket. Securing of the diamond was accomplished with a removable bottom plate, within which a small pocket was milled out for alignment. Small (sub-mm) channels were

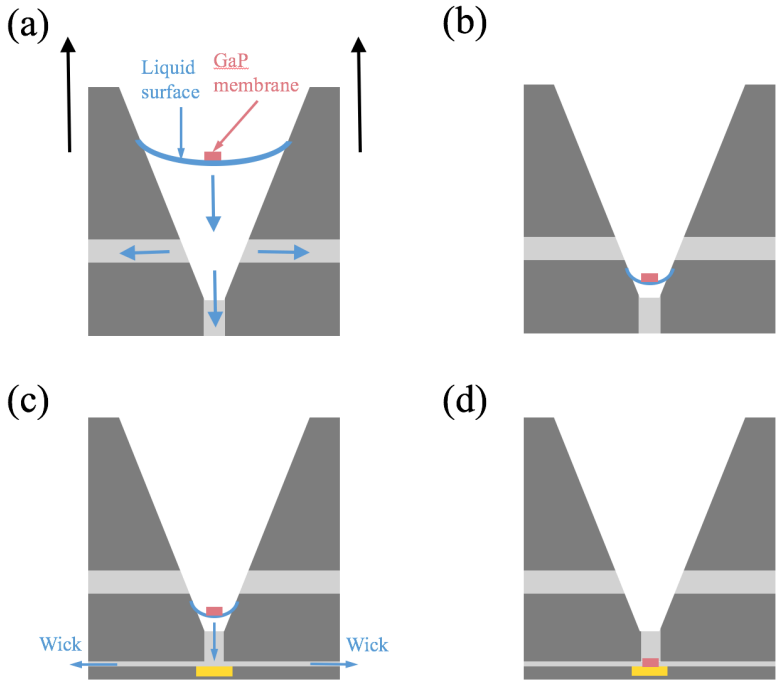

Figure 2.6: Illustration of 'bucket' transfer mechanism. (a) Membrane is trapped as 'bucket' is raised out of bath. Surface tension keeps membrane away from hydrophilic surfaces of tool. (b) Surface tension causes a small amount of liquid to remain trapped in bottom of bucket after removal from bath. (c) Diamond chip is clamped to bottom of 'bucket', and capillary channels are used to wick away remaining liquid. (d) Membrane is left on diamond chip.

milled into the bottom of the upper bucket piece in order to allow for capillary-based draining of remaining liquid. In practice, this final draining step was accomplished by bringing a cleanroom wipe into contact with the ends of some capillary channels, thus quickly wicking up the small amount of remaining liquid and leaving the membrane to settle onto the diamond chip at the bottom of the bucket (Figs. 2.6(c,d)).

We elected to used aluminum as the material for the tool(s) due to its compatibility with machining tools and its naturally hydrophilic surface. This worked well for the final water-to-diamond transfer, but aluminum is not compatible with HF. Though HF is typically

considered a weak acid, the 1.5% dilution used to release GaP membranes still immediately begins to attack the metal, creating too many bubbles to controllably capture a floating membrane. For this reason, a second bucket was fabricated out of polytetrafluoroethylene (PTFE, a.k.a. Teflon) for the initial transfer from the acid solution to the water bath. While PTFE is actually quite hydrophobic, we have still had a nearly 100% success rate with the initial transfer using the tool. The success rate of the final transfer step is lower (between ∼66% and ∼75%), but still represents a large improvement in yield and repeatability over the free-hand process. The 'bucket' technique also typically results in well-centered and undamaged transferred membranes. The main failure mechanism for the bucket-enabled final transfer is the membrane coming into contact with the bucket sidewall during the final draining, and remaining stuck to the bucket surface.

Given the promising results obtained using the prototype 'bucket' tools, it appears likely that further design iteration could lead to near-unity yield for membrane transfer. In particular, use of larger diamond chips and GaP membranes, and careful design of the final drainage mechanism can likely significantly increase the success rate of the final water-to-diamond transfer step.

Chapter 3
DEVICE DESIGN

This chapter outlines the methodologies used to design several photonic components required for the implementation of fully integrated NV-based MBQIP. In particular, device designs for the three circled elements in Fig. 1.4 are presented: waveguide-coupled disk resonators for enhanced photon collection; grating couplers for off-chip photon routing; and directional couplers for photon interference (Sections 3.1, 3.2, and 3.3, respectively). Designs for Y-junctions (not shown in Fig. 1.4) are also presented in Section 3.4.

3.1 Disk Resonators

As mentioned in Section 1.3, disk resonators play a crucial role in the GaP-on-diamond platform. Specifically, they are aimed at efficiently collecting and enhancing ZPL emission from coupled NV centers through the Purcell effect [51]. Further, because this work is largely motivated by long-term scalability, it is also important that ZPL photons collected into the resonator mode be efficiently coupled to single-mode waveguides as part of an eventual larger photonic network (See Fig. 3.1). Thus the relevant figure of merit for bus-coupled disk resonators in this work is the total quantum efficiency *into the bus waveguide*:

$$\eta_{wg} = \frac{\eta_{out} F_P}{F_P + \gamma_0/\gamma_{ZPL}}, \tag{3.1}$$

where η_{out} is the disk-to-bus out-coupling efficiency, $\gamma_0/\gamma_{ZPL} \approx 30$ is the ratio of total photon emission rate to ZPL photon emission rate for an un-enhanced emitter, and F_P is the Purcell enhancement factor. The Purcell factor is given by:

$$F_P = \frac{3}{4\pi^2}\left(\frac{\lambda}{n_{GaP}}\right)^3 \left(\frac{n_{GaP}}{n_C}\right) \left(\frac{\hat{\mu}\cdot\vec{E}_{NV}}{|\vec{E}_{max}|}\right)^2 \left(\frac{Q}{V}\right), \tag{3.2}$$

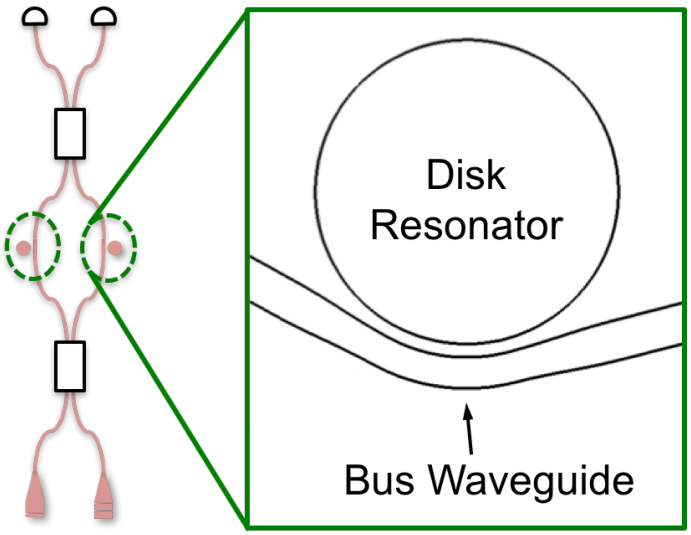

Figure 3.1: Schematic of integrated entanglement generation circuit proposed in Chapter 1 indicating the location of disk resonators for high-efficiency coupling of ZPL photons into the circuit. Inset: Schematic top-view of an example waveguide-coupled disk resonator.

where λ is the wavelength of light ($\sim$637 nm), n_{GaP} and n_C are the refractive indices of GaP and diamond respectively, $\hat{\mu}$ is a unit vector aligned with the dipole moment of the coupled NV center, $\vec{E}_{NV}$ and $\vec{E}_{max}$ are the electric field of the resonator mode at the NV and at the mode field maximum respectively, and Q and V are the quality factor and mode volume of the resonator respectively. From Eqs. 3.1 and 3.2, it can be seen that in order to maximize η_{wg}, the resonator out-coupling efficiency and quality factor should be maximized while the mode volume should be minimized. However, there are fundamental tradeoffs between these three quantities. Increasing the out-coupling strength of a resonator will decrease its quality factor, as can decreasing the mode volume. Thus for a given material platform with known NV center depth, there exists an optimal device configuration (disk geometry and coupling strength).

While the determination of this optimal design can mostly be accomplished with electromagnetic simulations and material properties taken from literature [52], one particular measured quantity was required for our specific materials and fabrication process: optical

loss, or equivalently, the intrinsic quality factor of fabricated resonators. To this end, an initial chip was fabricated with minimal design and only simple structures: straight waveguide sections tapered to uniform grating couplers at either end, with coupled disk resonators (SEM images shown in Fig. 3.2). This initial data was important in determining minimum disk radii as well as the desired disk-to-bus coupling strength, as discussed in the following sub-sections.

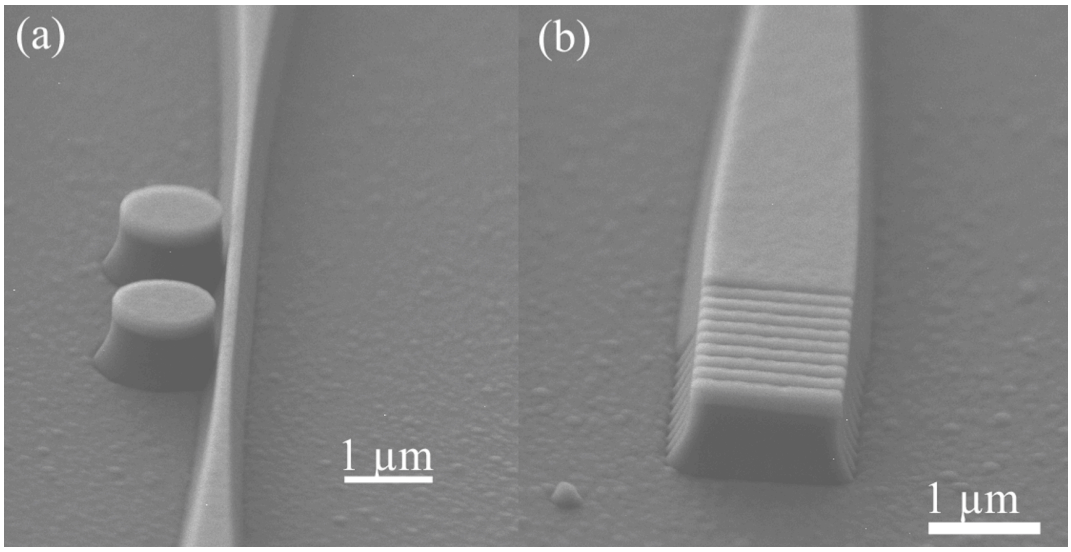

Figure 3.2: SEM images of initial devices. (a) Disk resonators coupled to a section of single-mode waveguide, and beginnings of tapers at either end. (b) Grating coupler for off-chip coupling.

3.1.1 Disk Geometry

We began the design of the resonators by determining an optimal geometry for GaP-on-diamond disks, as defined by the GaP thickness and the disk radius. For well-confined modes, the effects of these two parameters are relatively decoupled and can thus be optimized independently. The thickness of the GaP waveguiding layer was determined as a tradeoff between the slab mode size and the mode field at a depth of ∼15 nm in the diamond

(the expected location of implanted NV centers), as well as waveguide and resonator loss. Fig. 3.3(a) shows a plot of the relevant parameter $F_{slab} = |\vec{E}_{NV}|^2 / \left(h|\vec{E}_{max}|^2\right)$ as a function of GaP thickness, where h is the slab-mode height. As can be seen from the plot, there is a clear maximum near a 50-nm slab thickness. There is a steep drop-off for thinner GaP thicknesses, corresponding to the rapid expansion of the mode as the cutoff condition is approached. As the slab thickness is increased above 60 nm, F_{slab} decreases in an exponential manner due to better mode confinement within the GaP. In this work, we opted for a slab thickness of 125 nm, accepting a factor of ∼3 below the optimal value of F_{slab} as a tradeoff for confidence in low-loss propagation. Specifically, the degree to which top and bottom surfaces contribute to waveguide/resonator loss was not known, and these contributions will increase with lower field confinement. However, slab thicknesses in the 60-90 nm range should be explored in future work (see Section 6.1).

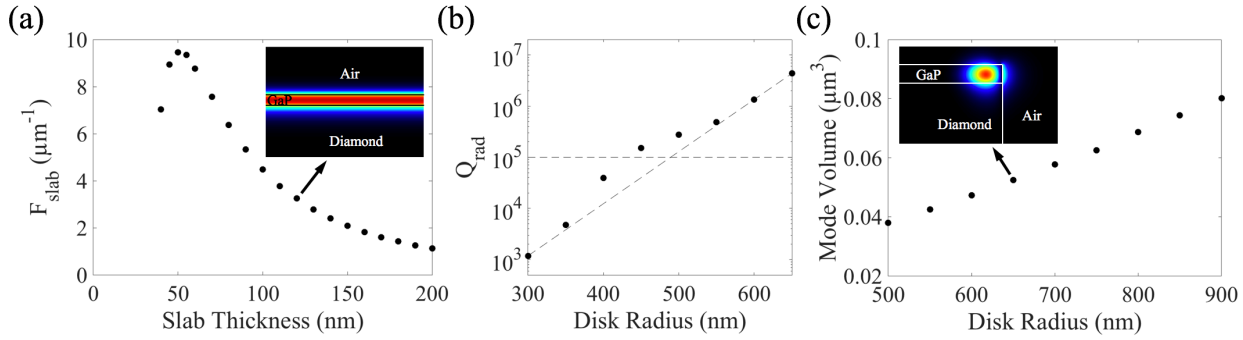

Figure 3.3: (a) Plot of NV-slab coupling parameter $F_{slab} = |\vec{E}_{NV}|^2 / \left(h|\vec{E}_{max}|^2\right)$ as a function of GaP thickness. Inset: Plot of E_x for slab mode near selected thickness of 125 nm. (b) Plot of radiation-limited quality factor (Q_{rad}) as a function of disk radius for the selected GaP thickness of 125 nm. (c) Plot of mode volume V as a function of disk radius for the selected GaP thickness of 125 nm. Inset: Plot of E_r for disk mode with a radius of 650 nm.

We next determined an ideal disk radius for the platform, initially trading off between radiation-loss limited quality factor and mode volume: while the vertical mode size is largely determined by our choice of GaP membrane thickness, confinement in the two in-plane spatial

dimensions is determined by the radius of curvature of the resonant mode. Finite-difference time-domain (FDTD) electromagnetic simulations showed that disk radii above ∼500 nm should exhibit radiation-limited quality factors exceeding 1×10^5, an order of magnitude higher than the measured quality factors exhibited by initial devices. However, there is an exponential drop-off in radiation-limited quality factor as the disk radius is further decreased (see Fig. 3.3(b)). This suggests that a disk radius of ∼500 nm is likely optimal, and the quality factor will be limited by material absorption and/or scattering losses. Further, it turns out that disks with radii between 400 nm and 500 nm exhibit hybrid-polarization eigenmodes (see Appendix C). While this is not fundamentally problematic for coupling to NV centers, it would significantly complicate device measurements as well as the integration of the resonators into larger systems. Once again trading off optimal performance for confidence in successful device yield, we opted for disks with radii between 650 nm and 700 nm, accepting a ∼40% larger-than-optimal mode volume. Fig. 3.3(c) shows a plot of mode volume as a function of disk radius.

3.1.2 Coupling Geometry

The final design parameter we looked at was the disk-to-waveguide out-coupling strength, which determines the out-coupling efficiency as well as the quality factor of a resonator, given an intrinsic quality factor Q_i. Measured quality factors from the initial device chip were between Q = 5,000 and Q = 10,000, and eigenmode simulations indicated that the disks were significantly under-coupled, in good agreement with low extinction ratios exhibited in resonator transmission spectra. Based on these initial measurements, we assumed $Q_i \approx$ 10,000 in our design models. For a given Q_i, device quality factor Q can be determined as a function of coupling quality factor Q_c, using:

$$Q = \left(\frac{1}{Q_i} + \frac{1}{Q_c} \right)^{-1} \tag{3.3}$$

$$Q_c = \frac{2\pi\tilde{\beta}_g}{\kappa^2} \tag{3.4}$$

where $\tilde{\beta}_g$ is the angular group propagation constant of the resonant mode, and κ is the field out-coupling coefficient. Using Eqs. 3.1-3.4, η_{wg} can be calculated as a function of coupling strength for our selected geometry, as shown in Fig. 3.4. In order to mitigate uncertainty in

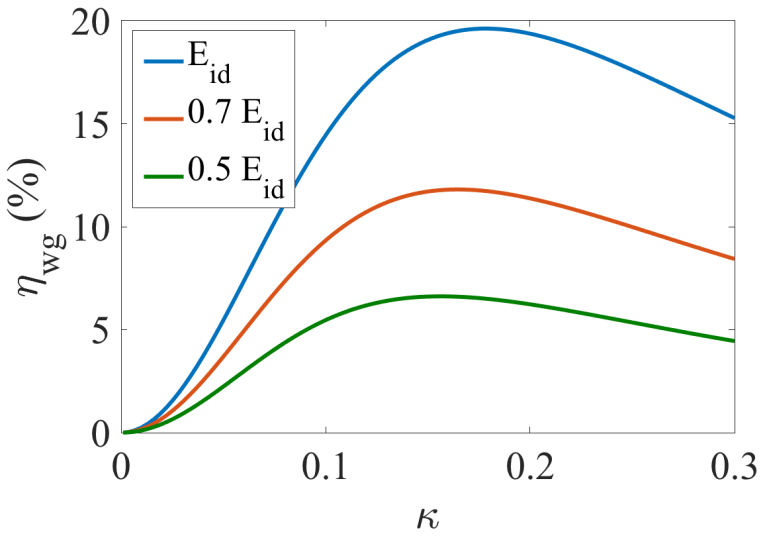

Figure 3.4: Simulated total quantum efficiency into the waveguide mode (η_{wg}) as a function of coupling strength (κ) for an NV center ideally located and oriented 15 nm below the GaP-diamond interface, as well as for NV centers with reduced mode interaction as indicated by effective mode fields of 0.7 and 0.5 times the ideal field. An intrinsic quality factor of Q_i = 10,000 is assumed, based on initial device measurements.

both the intrinsic quality factor of fabricated disks and the mode interaction with coupled NV centers, we elected to design and fabricate devices with a relatively wide range of field coupling coefficients, from $\kappa = 0.05$ to $\kappa = 0.3$. The total quantum efficiency achieved in fabricated devices can be obtained from single-photon measurements of device-coupled ZPL emission from single NV centers (see Chapter 5, Section 5.3.4).

Coupling can be described as the result of the uncoupled disk and waveguide modes being projected onto the eigenbasis of the coupled system. Interference between the system eigenmodes results in a sinusoidal flow of power between the un-coupled modes over the length of the interaction region. Assuming all power is initially in only one of the un-coupled

modes, we can write an expression for power in the second mode as a function of interaction length:

$$P_c = Asin\left(\beta L_i\right). \tag{3.5}$$

Neglecting unguided radiation modes, coupling is completely determined by projections of the uncoupled modes onto the coupled system's eigenbasis, the difference in propagation constant between the two system eigenmodes, and the length of the coupled region. There are three geometric parameters that define a disk-to-bus coupling region, all of which can affect the coupling strength: the waveguide width, the disk-to-waveguide spacing, and the interaction length. Waveguide width predominantly affects the mode projections, and thus the amplitude of the sinusoidal power flow (A); disk-to-waveguide spacing predominantly affects the propagation constant splitting of the system eigenmodes, and thus the length-scale of the sinusoidal power flow (β); interaction length (L_i) is left as the effective argument of the sinusoid.

Coupling regions were designed using eigenmode simulations of both uncoupled disks and waveguides, and of the coupled system. Fig. 3.5 shows the field coupling coefficient as a function of interaction length for 3 different coupler types, as defined by the coupling region cross-section. Coupler Types 1, 2 and 3 use waveguide widths of 160 nm, 140 nm and 130 nm, respectively, and disk-to-waveguide spacings of 80 nm, 80 nm and 100 nm, respectively. For each cross-section, three interaction lengths were selected for fabrication, corresponding to different expected coupling coefficients as indicated in Fig. 3.5. Achieved coupling coefficients can be obtained from waveguide-coupled transmission measurements of fabricated devices (see Chapter 4, Section 4.2.1).

Disk-to-waveguide coupling can also be described by perturbation analysis, and in the limit of small field interaction, the perturbation analysis should match the eigenbasis projection analysis. For additional coupled disk resonator analysis, including perturbation analysis of disk-to-waveguide coupling, see Appendix A.

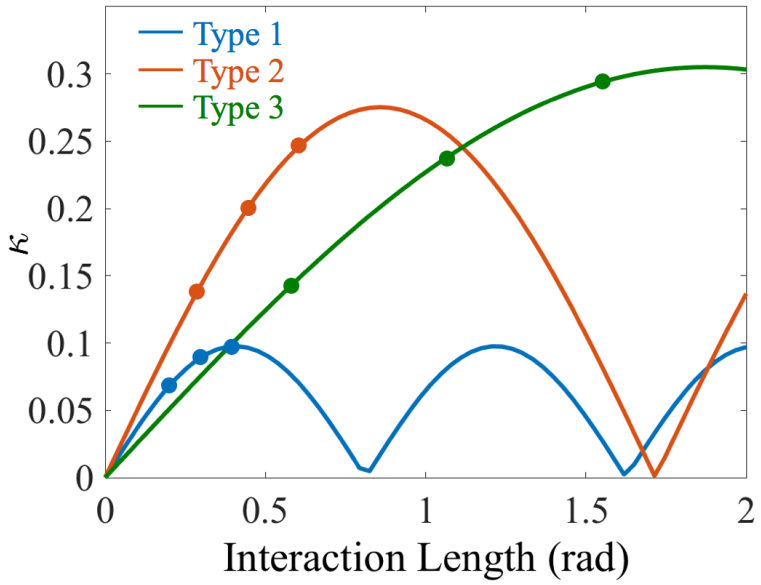

Figure 3.5: Plot of field coupling coefficient (κ) as a function of interaction length for Coupler Types 1, 2 and 3. Interaction lengths selected for fabrication, and expected coupling coefficients, are indicated as circular markers. Interaction length is specified in radians, as the device radii are on the order of the coupler geometry, and effective lengths are not well defined.

3.2 Grating Couplers

The purpose of grating couplers [53] is to efficiently couple on-chip waveguide modes to directional free-space modes, typically for off-chip photo-detection. In particular, grating couplers can be placed at the output ports of an integrated entanglement generation circuit for off-chip single-photon detection (see Fig. 3.6). The main challenge in designing efficient grating couplers in the GaP-on-diamond platform arises from the combination of high-index-contrast materials and the single full etch in the fabrication process. As a result of these two characteristics, individual grating-lines both scatter into free-space *and* reflect into the counter-propagating waveguide mode (see Fig. 3.7(a)). In more mature photonics platforms, a very shallow etch is typically included in the fabrication process specifically to enable

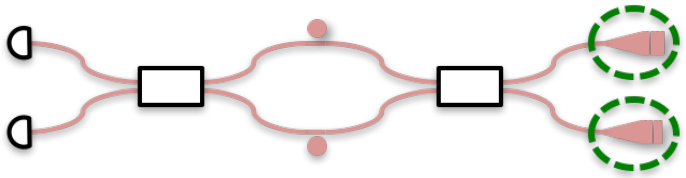

Figure 3.6: Schematic of integrated entanglement generation circuit proposed in Chapter 1 indicating the location of grating couplers for off-chip detection at two of the four output ports. Note that the integrated detectors on the remaining two output ports could also be replaced with grating couplers.

grating-lines that effectively only scatter out of the waveguide. In such cases, back-reflections from the lines can be ignored (see Fig. 3.7(b)). The phase and amplitude of scatter from each grating-line are then determined by the line's position and scattering strength, respectively. This allows for analytical design of a grating coupler's output beam profile. In the case of fully etched GaP-on-diamond grating couplers, reflections must be taken into account. The scatter from each grating-line then depends on the position and scattering strength of *all* of the lines in the structure. For line numbers larger than 2 or 3, analytical design of the output beam quickly becomes impractical, if not impossible.

In order to deal with strong in-waveguide reflections, grating coupler design was performed using a simulated-annealing optimization algorithm. The objective function to be optimized was an inner product between the upward scattered field coefficients and the field distribution of the desired free-space beam:

$$\langle S|\Psi\rangle = \sum_{i=1}^{N} S_i^* E_\Psi(z_i), \tag{3.6}$$

where S_i are the upward scattered field coefficients from each line, and $E_\Psi(z_i)$ is the complex field coefficient of the desired output beam at the location of the i^{th} line (see Fig. 3.8). For each iteration of the optimization, the field distribution along the length of the grating structure was calculated using a transfer-matrix approach. The upward scatter coefficients were then determined as $S_i = s_i E_i$, where s_i are the scattering coefficients for each grating-

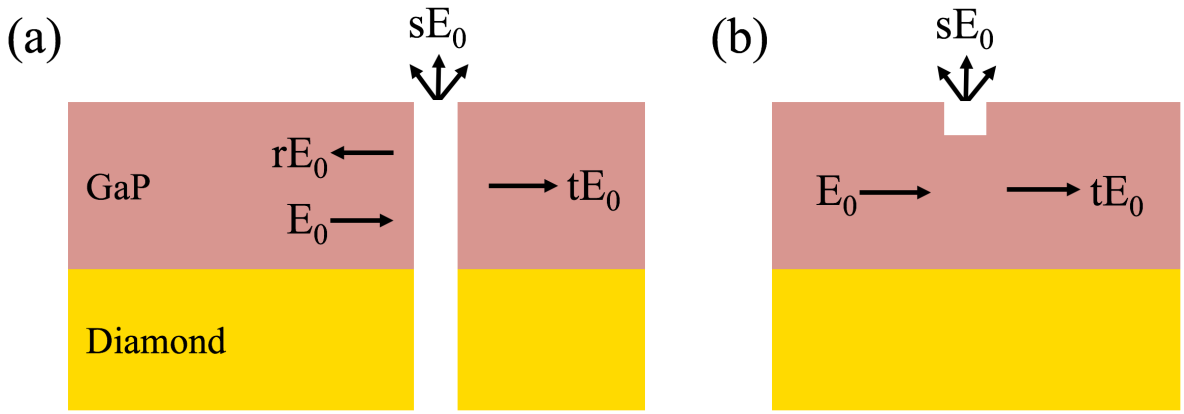

Figure 3.7: Schematic cross-sections of two types of grating-lines. (a) A fully-etched line like those in our platform, showing reflection as well as scattering and transmission. (b) A shallow line typically included in more mature integrated photonics platforms, showing only scattering and transmission.

line and E_i are the in-waveguide fields at each grating-line. The output from the optimizer consists of two lists: a list of grating-line positions and a list of line types, with line types defined by s, r and t (see Fig. 3.7(a)). Promising output designs from the optimization software were first simulated using 2-dimensional FDTD for refinement, and final designs were simulated with full 3-dimensional FDTD for verification.

Fig. 3.9 shows a top-view of the standard grating coupler design, as well as FDTD simulation results. All grating-lines were designed with a size of 50 nm along the guided-mode propagation direction (z). Different scatter/reflection strengths were achieved using either full trenches spanning the width of the structure, or 4 evenly spaced 'sub-trenches' of variable width. In the case of this design, the 3 first lines were manually forced to be weaker scatterers/reflectors in an attempt to increase the bandwidth of the device and reduce back-reflections. The coupler was designed to match a vertical-incidence, free-space Gaussian beam with a full-width half-maximum (FWHM) beam-width of 750 nm. Simulated performance indicates an expected coupling efficiency of 20.8% at the design wavelength of 637 nm. The coupling efficiency of fabricated devices can be obtained from transmission

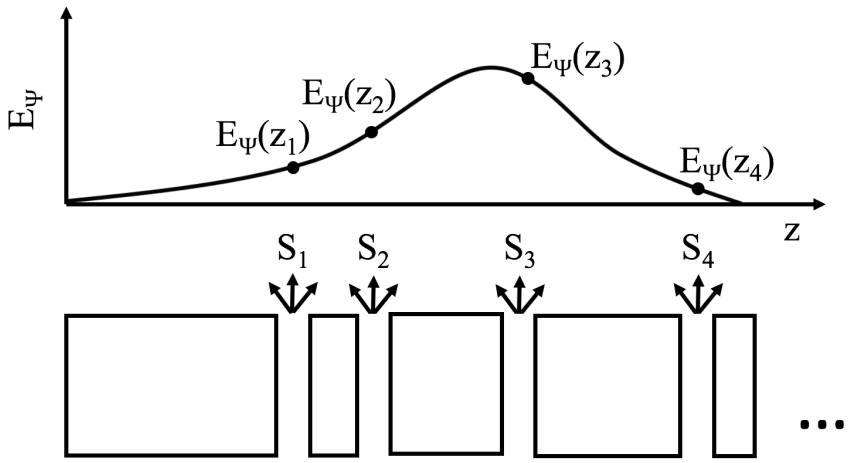

Figure 3.8: Illustration of inner product objective function for grating design optimization.

measurements, for which results are presented in Chapter 4, Section 4.2.3.

3.3 Directional Couplers

Directional couplers allow low-loss, arbitrary coupling between two waveguide modes, and can be thought of as the integrated optics equivalent of a free-space beam-splitter or beam-sampler [54, 55]. GaP-on-diamond directional couplers were designed primarily to act as low-loss beam splitters in an eventual entanglement generation circuit (see Fig. 3.10), but will also likely be used for beam sampling as more complex photonic circuits are implemented in the GaP-on-diamond platform. The design of directional couplers is very similar to that of the coupling region for waveguide-coupled disks (see Section 3.1.2), with the primary difference being that coupling occurs between two waveguide modes. As in the case of disk-to-bus coupling regions, design was performed using eigenmode simulations (see Figs. 3.11(a,b)). The design parameters were waveguide width, inter-waveguide spacing and interaction length.

Two coupler cross-sections were selected for fabrication, as defined by waveguide width and inter-waveguide spacing. Waveguide widths of 160 nm and 180 nm were selected, both

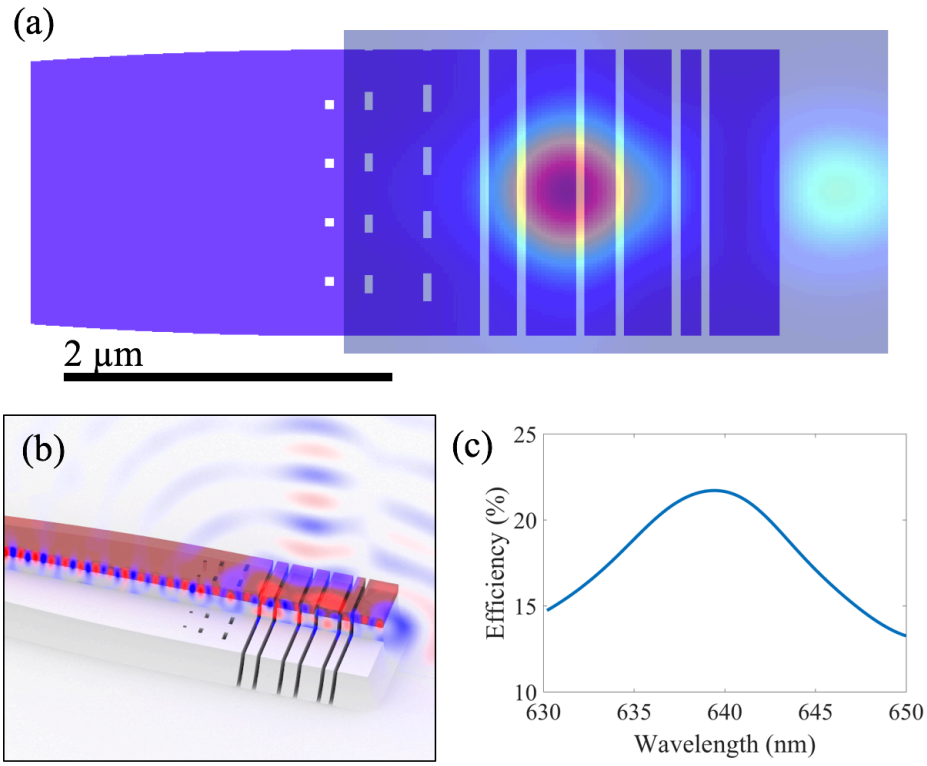

Figure 3.9: (a) Scaled schematic top view of standard grating design, with overlaid output beam profile 1 μm above grating (simulated). (b) Profile view showing 3D model of grating structure with simulated fields overlaid. (c) Simulated coupling efficiency as a function of wavelength. Simulations by S. Hyra and Y. Zhou.

paired with an inter-waveguide spacing of 80 nm. Simulated beat lengths were 10.0 μm for the 160 nm waveguides, and 16.8 μm for the 180 nm waveguides (see Fig. 3.11(c)). Here, beat length is defined as the length over which power flows completely from one waveguide mode to the other, and back again.

Coupling ratios for individual fabricated devices can be obtained from transmission measurements. Characteristic beat lengths for fabricated devices can be extracted from measured coupling ratios of groups of devices, within which the interaction length is varied. The results of such measurements are presented in Chapter 4, Section 4.2.2.

Identical waveguide widths were used in the design of these devices in order to reduce the

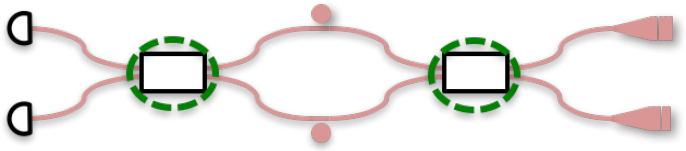

Figure 3.10: Schematic of integrated entanglement generation circuit proposed in Chapter 1 indicating the location of direction couplers for on-chip photon interference.

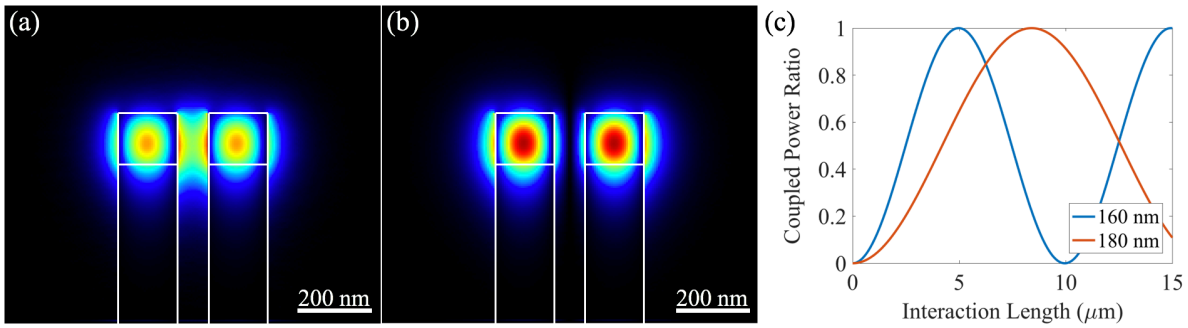

Figure 3.11: (a) Simulated transverse electric field magnitude for TE-polarized symmetric (bonding) eigenmode in 160 nm coupler. (b) Anti-symmetric (anti-bonding) eigenmode. (c) Simulated power coupling for 160 nm and 180 nm couplers.

number of parameters on which measurements would depend, and thus simplify the analysis. However, it is worth noting that particularly for a 50:50 splitting ratio, phase matching between the two un-coupled modes may not be desirable, as can be seen by examining the equation for power in the coupled mode:

$$P_c(z) = \frac{4|\kappa_{21}|^2}{(\beta_1 - \beta_2)^2 + 4\kappa_{12}\kappa_{21}} sin^2\left(\left(\sqrt{\left(\frac{\beta_1 - \beta_2}{2}\right)^2 + \kappa_{12}\kappa_{21}}\right) z\right), \tag{3.7}$$

where κ_{21} and κ_{12} are the infinitessimal coupling coefficients from the input mode to the coupled mode and vice-versa, and β_1 and β_2 are the propagation constants of the input and coupled modes, respectively (see Appendix A). For identical waveguides $\kappa_{21} = \kappa_{12}$ and

$\beta_1 = \beta_2$, and Eq. 3.7 reduces to:

$$P_c(z) = sin^2(\kappa_{21} z) \tag{3.8}$$

While this allows for arbitrary coupling via choice of interaction strength and interaction length, 50:50 splitting occurs at the point along the sinusoid that is most sensitive to errors in both of these design quantities. For this reason, future designs will likely make use of mismatched waveguide modes which satistfy:

$$\frac{4|\kappa_{21}|^2}{(\beta_1 - \beta_2)^2 + 4\kappa_{12}\kappa_{21}}) = C, \tag{3.9}$$

where C is the ideal coupled power for the application.

3.4 Y-Junctions

Y-junctions are useful for beam-splitting and in contrast to directional couplers, they are broadband and inherently symmetric in their splitting ratio. However, they are typically lossier than directional couplers when used as splitters, and as a 3-port device they are fundamentally lossy when used in reverse (2-into-1, as opposed to 1-into-2).

Y-junctions were designed as a combination of 3 tapers. A taper from the input waveguide width out to a maximum junction width was used to reduce scattering from the junction-point. Two symmetric tapers separated by a 50 nm junction-point reduce back down to the two output waveguides (see Fig. 3.12). All tapers were aimed at adiabatic mode expansion/compression. Junctions were designed for both 160 nm and 270 nm input/output waveguides. Losses in these devices are expected to be on the order of $\sim$1 dB based on simulation. This should be detectable in waveguide-coupled transmission measurements (Chapter 4, Section 4.2.4).

3.5 Summary

We have presented design methodologies for four types of integrated optical components useful for the development of NV-center-based quantum information processing in a GaP-

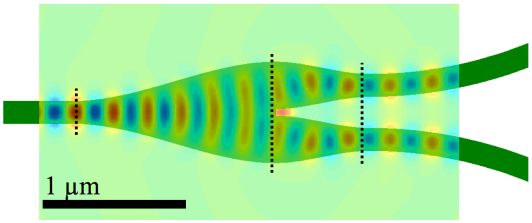

Figure 3.12: Scaled schematic top view of Y-junction for 160 nm waveguides, with overlaid plot of transverse electric field obtained from FDTD simulations. Dashed lines delineate component taper regions.

on-diamond platform. Further, we have selected designs for fabrication, with expected performance metrics relevant to quantum information applications and which can be measured in fabricated devices. The majority of these can be obtained from waveguide-coupled transmission measurements (Chapter 4), with the notable exception of total quantum efficiency for ZPL photons coupled into a waveguide mode, η_{wg}. Obtaining η_{wg} for fabricated devices requires single-photon measurements of ZPL emission from individual device-coupled NV centers (Chapter 5).

Chapter 4

LARGE-SCALE INTEGRATED PHOTONICS FOR NV CENTER-BASED QUANTUM INFORMATION

Here we detail chip-scale characterization of three key components of an integrated diamond photonics platform: waveguide-coupled disk resonators, directional couplers, and grating couplers (Fig. 4.1). We also present waveguide loss measurements for single-mode ridge waveguides and Y-junctions. The measured device performance suggests possible total quantum efficiency as high as $\eta = 5.5\%$ with off-chip coupling, and as high as $\eta_{wg} = 33\%$ into a traveling waveguide mode (on-chip). Further, demonstrated device yields and cross-chip uniformity should enable integration of more complex optical circuits in the platform, as discussed in Section 4.3. Sections 4.1 and 4.2 describe the measurement setup and experimental results, respectively.

4.1 Transmission Measurement Setup

Transmission measurements were taken using a custom-built microscope (see Fig. 4.2(a)). Excitation was provided by an LED with a peak wavelength of 640 nm, and with a relatively broad emission spectrum extending from approximately 630 nm to 645 nm. Input light was focused onto the sample with a commercially available microscope objective (Nikon, 60x, 0.7 NA). Transmitted light was collected through the same objective and focused through a 100-μm pinhole, corresponding to a 1.7-μm-diameter collection area on the sample. The light collected through the pinhole was either coupled into a photodetector or a grating spectrometer, or imaged onto a CCD camera. The input and collection optical paths were separated by a 50:50 beam-splitter.

Light was coupled to and from the chip by means of grating-couplers [53]. Throughout

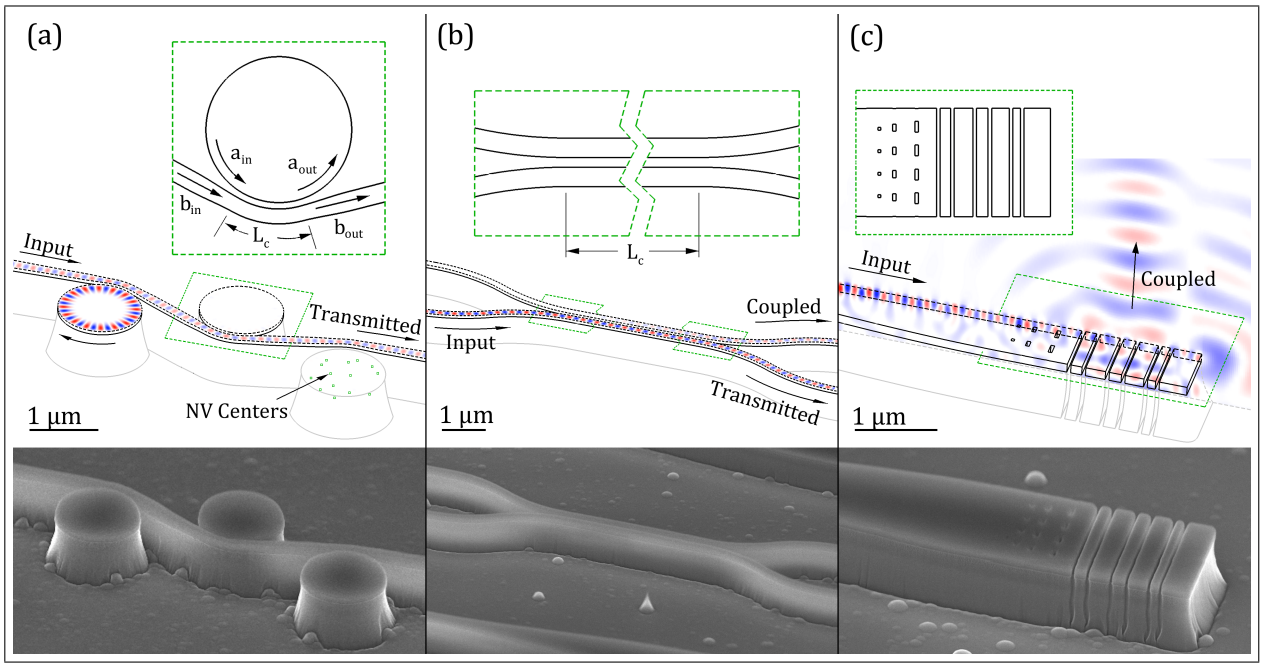

Figure 4.1: Schematic views with overlaid FDTD simulations, and SEM images of fabricated devices: (a) waveguide-coupled disk resonators; (b) directional coupler; (c) grating coupler (with schematic view halved for clarity). Figure by I. R. Christen.

this chapter, we will refer to sets of connected grating couplers as measurement loops (see Fig. 4.2(b)). In order to reduce collection of scattered light from the input grating, input and output gratings were defined at right angles to one another, and the input and collection paths of the microscope were cross-polarized. Input polarization was controlled via a half-wave plate on the objective side of the 50:50 beam-splitter, with all measurements being done for TE-polarized guided modes.

Microscope automation was crucial for obtaining the large amount of transmission data presented in the remainder of this section. Linear actuators and piezoelectric-controlled stages were used for large-scale and fine movement of the microscope objective over the chip, respectively. Galvo-controlled mirrors in the input beam path allowed scanning of the input beam while collecting from a fixed area. These elements, combined with a grid-based device

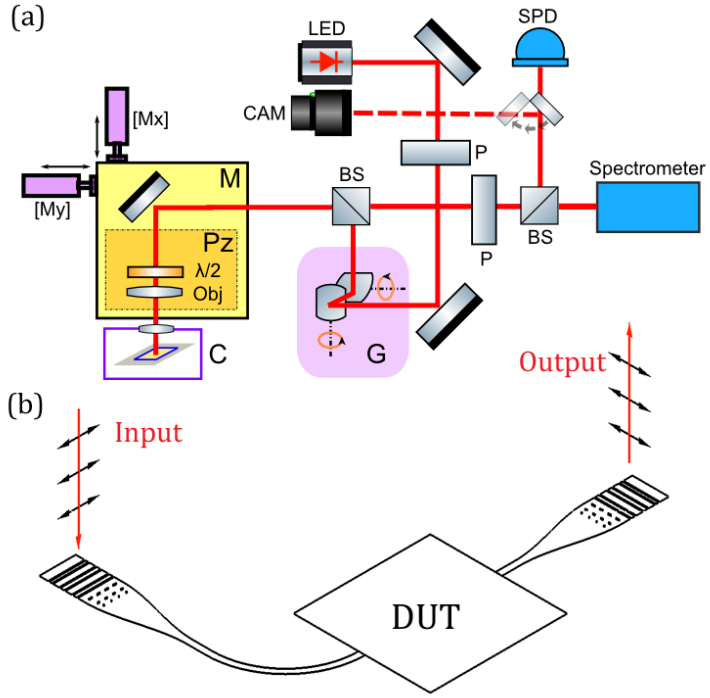

Figure 4.2: (a) Schematic of microscope setup, showing galvo mirror system (G), micrometer stage (M), and piezo stage (Pz) used for automated testing. Additional labels: P: polarizer; BS: beam-splitter; SPD: photodetector; C: cryostat sample chamber; $\lambda/2$: half-wave plate. (b) Schematic of transmission measurement for an arbitrary device-under-test (DUT). Figure by S. Chakravarthi and I. R. Christen.

layout, enabled automated testing of all devices of a certain class in a single testing run, robust to device-to-device variations.

4.2 Transmission Measurement Results

4.2.1 Waveguide-Coupled Disk Resonators

Because the success rate of measurement-based entanglement scales as the square of total quantum efficiency [18], and because demonstrated efficiencies have been low [27–29], there remains a great deal of room for improved entanglement rates through photonic integration.

In-plane resonant structures can be used to enhance emission into the ZPL through the Purcell effect [51]. Photonic crystal cavities built around NV centers have been demonstrated with Purcell factors as high as Fp = 69 [56], corresponding to ∼68% of emission into the ZPL. Further, for $F_p \gg 1$, nearly all ZPL photons are emitted into the resonator mode [46]. As can be seen from Eq. 3.2, the Purcell factor of an optical resonator scales linearly with the quality factor Q. Equally important for the purposes of NV-center based quantum information is that ZPL photon emission be coupled into a useful optical mode. Thus, a second important metric for a resonant device is the coupling efficiency to an output mode. The disk-to-waveguide out-coupling efficiency η_{out} of a coupled disk resonator scales as the square of the field coupling coefficient κ.

Waveguide-coupled disk resonators were fabricated in the GaP-on-diamond platform. The resonators consist of whispering-gallery mode disks, with a coupling region in which a ridge waveguide is brought into close proximity of the disk (see Fig. 4.1(a)). As discussed in Section 3.1, three types of coupling region were used, as defined by bus waveguide width and disk-to-bus spacing. For each type of coupler, disks were built in triplets along individual ridge waveguides, with the length of the coupling region, L_c, varying within each triplet. Disk diameter was also slightly varied (4 nm) within each triplet in order to distinguish individual disk resonances. An SEM image of a disk triplet is shown in Fig. 4.1(a). A summary of the different coupling geometries can be found in Table 4.1.

Type	**Bus Width (nm)**	**Spacing(nm)**	**Lengths (rad)**
1	160	80	0.1; 0.2; 0.3
2	140	80	0.175; 0.35; 0.525
3	130	100	0.475; 0.95; 1.425

Table 4.1: Resonator Coupling Geometries

Transmission measurements were taken on the disk resonators, with transmitted light

coupled to the spectrometer. Measurement loops were determined to be working by the presence of a measurable output from the output grating coupler. The yield for full measurement loops was 97 out of 109 (89%). Within working measurement loops, waveguide-coupled disks were determined to be working by the presence of an associated resonance dip in the normalized transmission spectrum. The yield for waveguide-coupled disks was 127 out of 219 (58%). A scaled top-view of a measurement loop is shown in Fig. 4.3(a). An example transmission spectrum for a measurement loop with 3 working disks is shown in Fig. 4.3(b).

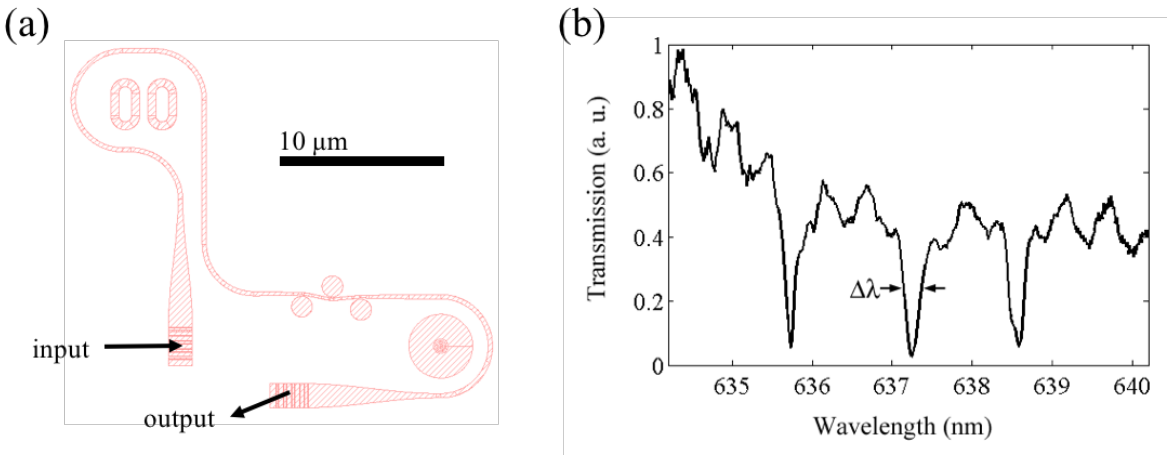

Figure 4.3: (a) Scaled top view of a resonator measurement loop. (b) Measured transmission spectrum for a disk measurement loop with 3 working disks. These devices used Coupler Type 2 (see Table 4.1).

The quality factor of a coupled disk resonator is a measure of its ability to store optical energy, and is limited both by intrinsic losses and out-coupling to the bus waveguide. Here, we define the quality factor in terms of measured quantities as:

$$\mathrm{Q} = \frac{\lambda_{res}}{\Delta\lambda}, \tag{4.1}$$

where λ_{res} is the resonant wavelength and $\Delta\lambda$ is the full width at half-power of the observed

resonance. The extinction ratio, r_{ext}, for a coupled disk resonator is a measure of how well coupled it is, and is defined in terms of measured quantities as:

$$r_{ext} = 1 - \frac{T_{res}}{T_0}, \tag{4.2}$$

where T_{res} and T_0 are the normalized transmission through the bus waveguide, on and off of resonance respectively. The field coupling coefficient, κ, for a waveguide-coupled disk can be calculated from the measured quality factor and extinction ratio. It is defined in terms of the behavior of the coupling region, for which the output fields are related to the input fields by:

$$\begin{bmatrix} a_{out} \\ b_{out} \end{bmatrix} = \begin{bmatrix} t & i\kappa \\ i\kappa & t \end{bmatrix} \begin{bmatrix} a_{in} \\ b_{in} \end{bmatrix}, \tag{4.3}$$

where a_{in}, b_{in}, a_{out} and b_{out} are the (disk and bus) input and output mode field coefficients, and t is the field transmission coefficient (see blue inset in Fig. 4.1(a)) [57].

Quality factors and extinction ratios were determined by fitting resonant dips in the measured transmission spectra. Fig. 4.4 shows box-and-whisker plots of the measured quality factors and extinction ratios, and calculated coupling coefficients. We note that the coupling coefficients for the fabricated devices are in close agreement with the design values presented in Chapter 3, Section 3.1.

For the weakest disk-to-bus coupling geometries (Coupler Type 1), all of the devices were clearly under-coupled. However among devices with stronger coupling geometry (Coupler Types 2 and 3), there were many near-critically-coupled and over-coupled devices. It is also worth noting that while Coupler Types 2 and 3 showed similar coupling coefficients, the average calculated intrinsic quality factor for devices using Coupler Type 3 was significantly higher (Qi = 11,700), than for those using Coupler Type 2 (Qi = 8,400). This is likely due to the wider disk-to-bus spacing used in Coupler Type 3, and suggests that excess loss in the coupling region is playing a role in limiting the intrinsic quality factors of the disks.

One of several promising devices for ZPL photon collection had a measured quality factor of Q = 5,100 and a measured extinction ratio of 67%. The device used Coupler Type 3

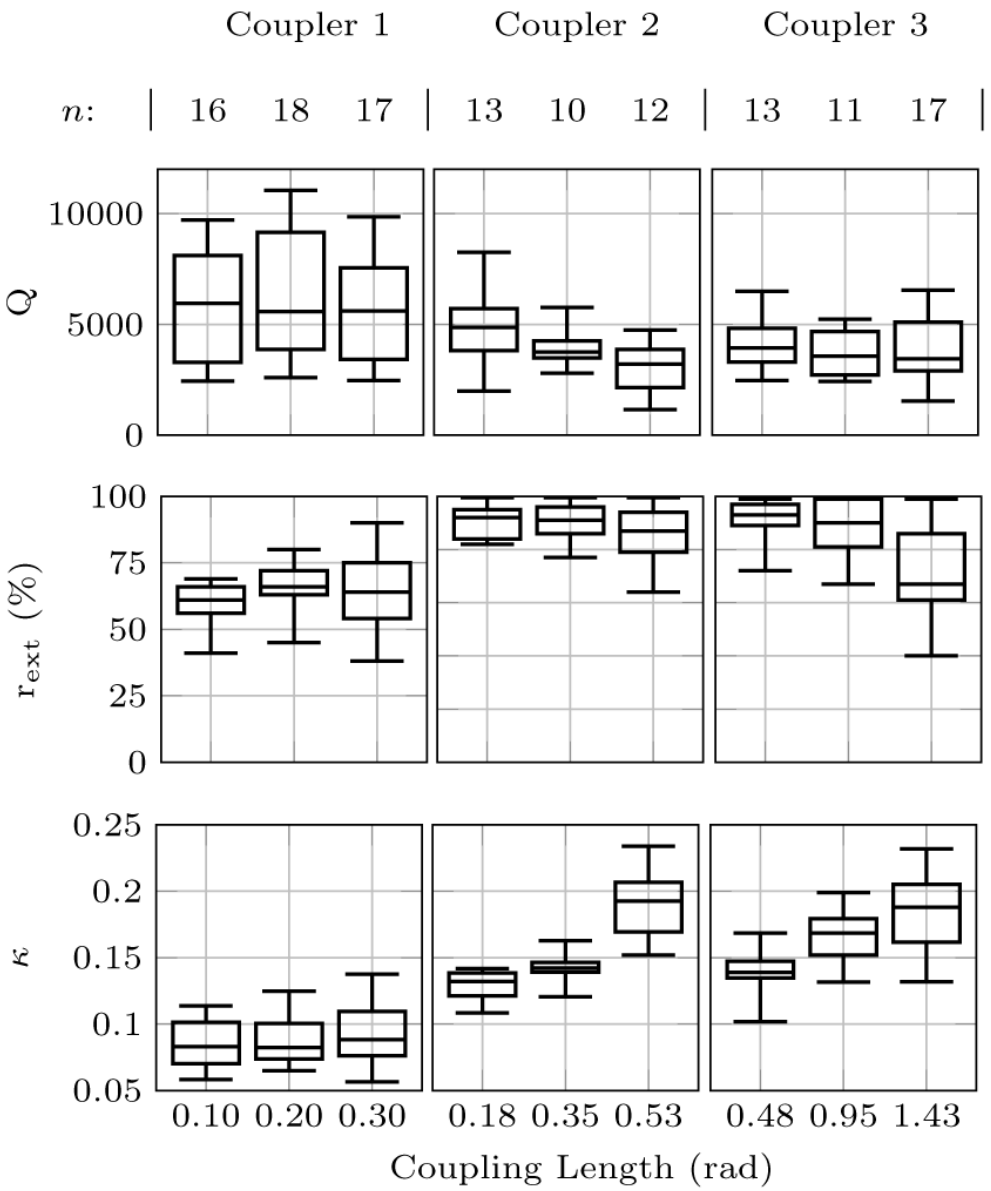

Figure 4.4: (a) Box-and-whisker plots showing the distribution in measured quality factor, measured extinction ratio, and calculated coupling coefficient for devices as a function of coupling geometry. Sample size for each coupling geometry is indicated at the top of the corresponding column.

with a coupling length of 1.425 radians, and was determined to be over-coupled based on the statistical behavior of similar devices. Given the simulated field distribution for the resonator mode, this would correspond to a Purcell factor of approximately 24 for an ideally oriented NV center at a depth of 20 nm below the diamond surface, or 44% of total photons emitted at the ZPL wavelength. 96% of these would emit into the resonator mode. The disk-to-bus coupling efficiency was calculated to be 79% for this device. The potential total quantum efficiency of ZPL photon collection into the bus waveguide is thus approximately 33%. This is over 200 times higher than what has been demonstrated using free-space optics.

4.2.2 Directional Couplers

As discussed in Section 3.3, directional couplers can be used to erase 'which-path' information when performing 2-qubit quantum protocols such as those described in [27–29], and are therefore highly desirable in an integrated system for NV center-based MBQC. Further, they can be used as beam samplers with arbitrary coupling ratios throughout an integrated system for testing. In both cases, well-defined coupling ratios and low excess insertion loss are desirable. In particular, a 50:50 coupling ratio is required to obtain a maximally entangled state without sacrificing efficiency when performing spin entanglement between NV centers [18]. However, devices with non-ideal coupling ratios can still be used to obtain a maximally entangled state, but with total quantum efficiency scaling as the lesser of either the coupling or transmission ratio. E.g. devices with either a 40:60 or 60:40 coupling-to-transmission ratio could be used to obtain maximally entangled states, but with total quantum efficiency scaled by a factor of 0.4.

Directional couplers were fabricated in the GaP-on-diamond platform, consisting of narrow ridge waveguide sections spaced closely together (Fig. 4.1(b)). Two types of couplers were fabricated and tested, based on 180 nm ridge waveguides and 160 nm ridge waveguides respectively. Both types had an 80 nm inter-waveguide spacing. For each type, 9 evenly distributed coupling lengths (L_c) were fabricated and organized into localized sets of 9.

Transmission measurements were taken on the directional couplers. Transmitted and

coupled optical modes were measured at two separate outputs, with output light being coupled into a photodetector (see Fig. 4.5(a)). Working measurement loops were defined as those with total output power (coupled + transmitted) at least 25% that of the lowest-loss devices. The yields were 76 out of 103 (74%) and 75 out of 104 (72%) for measurement loops with 180 nm ridge couplers and 160 nm ridge couplers, respectively.

Transmission and coupling ratios were obtained for each working loop, normalized to the total output. For sets with more than 5 working devices, the coupling ratios were fit to sinusoids in order to obtain a characteristic beat length. The beat length is defined as the distance required for power to couple completely from one mode to the other, and back again. Selected data and associated fits are shown for sets of each geometry in Fig. 4.5(b). The average beat lengths were 17.1 μm and 9.4 μm for the 180-nm ridge geometry and 160-nm ridge geometry, respectively. This is in close agreement with the designed beat lengths of 16.8 μm and 10.0 μm. A box-plot of calculated beat length for both geometries is shown in Fig. 4.5(c). The observed set-to-set variation in beat length suggests a 180 nm ridge-based coupler with a length of 4.4 μm can be expected to fall within the range of 0.4 to 0.6 coupling ratio approximately 60% of the time.

Excess loss in the couplers was determined to be 0.063 $\pm$ 0.015 dB/μm and 0.060 $\pm$ 0.025 dB/μm, for the 180-nm and 160-nm devices respectively. We can thus put an upper bound of 0.17 dB on the excess insertion loss for 180-nm ridge-based coupler with a length of 2.2 μm.

A low-loss directional coupler with a coupling ratio in the range of 0.4 to 0.6, when combined with a pair of resonators such as the one described at the end of Section 4.2.1, could be used for entanglement generation with a total quantum efficiency of 6.6% into a single on-chip guided mode. This represents nearly two orders of magnitude improvement in total quantum efficiency, compared with free-space. Based on the measured yields of the individual components and the probability of the directional coupler falling in the desired range, we can expect a yield of approximately 1 in 7 for such a system. I

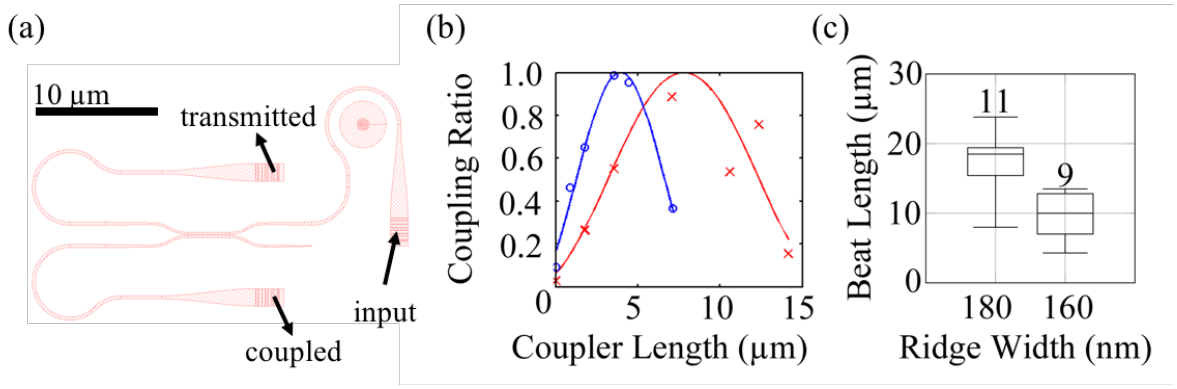

Figure 4.5: (a) Scaled top view of a directional coupler measurement loop. (b) Measured coupling ratios (markers) and sinusoidal fits (curves) for sets of 180 nm couplers (red, with X markers) and 160 nm couplers (blue, with circular markers). (c) A box-and-whisker plot showing the cross-chip distribution of estimated beat lengths for couplers of each type. The number of sets represented is noted above each distribution.

4.2.3 Grating Couplers

Grating couplers [53] are the primary method for coupling free-space light to on-chip guided modes in the platform. They are a crucial component for testing and development, and both high efficiency and cross-chip uniformity are desirable. Higher grating-coupler efficiency translates directly to stronger signals, and therefore shorter required measurement times. This is particularly true in the case of transmission measurements where the transmitted optical power scales as the square of grating coupler efficiency. Uniformity is important, as uncertainty in grating coupler performance can translate into uncertainty in the measurement.

Grating couplers were designed and fabricated on the GaP-on-diamond chip (see Fig. 4.1(c)), and transmission measurements were performed. The measurement loop structures were quite simple: two grating couplers joined by a short section of single-mode waveguide (see Fig. 4.6(a)). Output light was coupled into a spectrometer. The yield for measurement loops was 33 out of 42 (79%), where loops were determined to be working if the transmitted power

was within 2 standard deviations of the mean. We note that the yield for individual gratings is likely higher than that of the measurement loops since loop failures can be caused by the failure of a single grating or a failure in the bus waveguide.

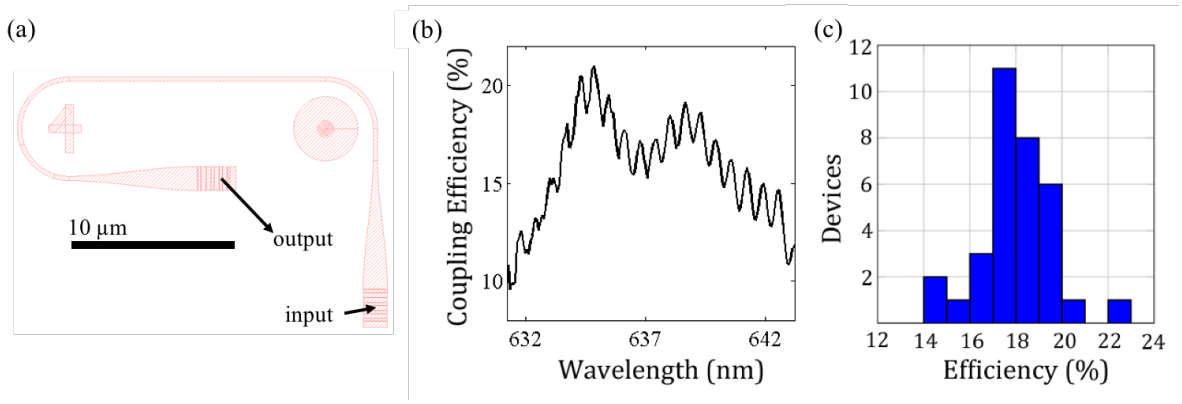

Figure 4.6: (a) Scaled top view of a grating coupler measurement loop. (b) A typical grating coupler efficiency spectrum. (c) A histogram showing the distribution of grating efficiencies at the ZPL wavelength (637.2 nm).

Fig. 4.6(b) shows a typical efficiency spectrum for a measurement loop, where coupling efficiency is taken as the square root of transmission. Fig. 4.6(c) shows a histogram of coupler efficiencies at the ZPL wavelength of 637.2 nm. The average coupling efficiency for the grating couplers at 637.2 nm was 17.0%, with a cross-chip standard deviation of 1.5%. This is slightly below the expected performance of 20.8% presented in Chapter 3, Section 3.2. Possible reasons for the discrepancy include waveguide loss and the use of a larger collection area in simulations as compared with the measured collection area.

The demonstrated cross-chip uniformity will in many cases be good enough to directly compare device performance across the chip, and local calibration can likely be used to improve uncertainty in grating performance when necessary. The measurement efficiencies, while well below unity, are sufficient for quantum device measurements including photon correlation measurement, resonant excitation spectroscopy, and measurement of Purcell enhancements. Ultimately this will be their primary role, as an eventual fully integrated

quantum information circuit should make use of on-chip photon detection [43, 58].

Nonetheless, when paired with a resonator such as the one described at the end of section 4.2.1, a grating coupler with average coupling efficiency would enable total off-chip quantum efficiency as high as 5.5%. This represents a factor of ∼5 improvement over the theoretical limit for free-space collection with SILs.

4.2.4 Y-Junctions

Y-junction measurement loops were designed as chains of 5 junctions in series, with one output arm of each junction terminating in a grating coupler and the other feeding into the input of the next junction (see Fig. 4.7(a)). Testing was primarily aimed at determining excess loss in the devices, and consisted of measuring the output power at each grating coupler (0 through 4). Fig. 4.7(b) and Fig. 4.7(c) show output power as a function of the number of excess junctions in the transmission path for 6 measurement loops, normalized to the first grating coupler in each set.

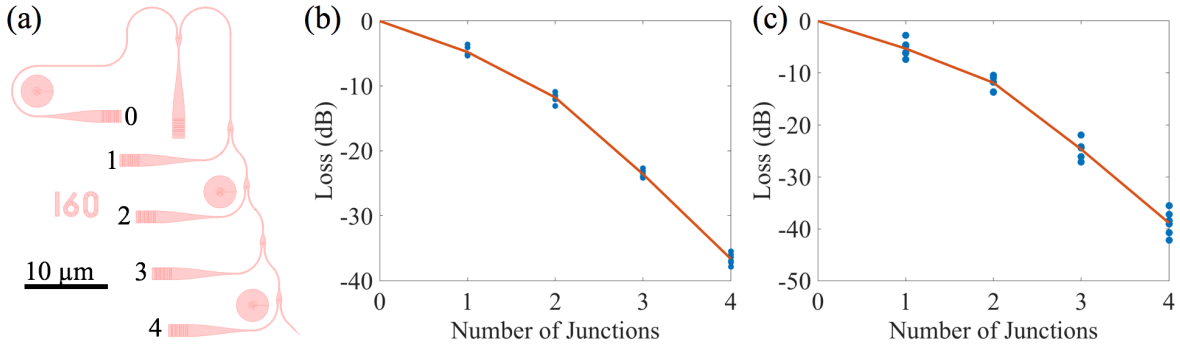

Figure 4.7: (a) Scaled top view of a Y-junction measurement loop. (b) Measurement results for 160 nm ridge junctions. The red curve represents the average. (c) Measurement results for 270 nm ridge junctions.

Surprisingly, single-device loss appears to increase with device number. Measured transmission values through the first excess junctions were -4.8 ± 0.7 dB and -5.3 ± 1.6 dB for

the 160 nm and 270 nm ridge width devices respectively. However, in both cases the single-junction transmission value decreases to below -13 dB by the final device in the chain. While the reasonable first-junction loss values indicate that single Y-junctions can likely be used safely in test circuits, the unexpected behavior of chained devices indicates an underlying problem with the device design. If these junctions are to be used in more complex photonic circuits, the cause of this behavior will need to be identified and suitably mitigated.

One possible explanation is that the junctions rotate the polarization of transmitted light. If combined with some polarization-dependent loss mechanism in the bus-waveguides and/or the junctions themselves, it is possible that this could result in the observed behavior. This theory is presented because it can (and should) be tested with the existing measurement setup and devices, by repeating the measurement with TM-polarized input light. This effect should also be observable in FDTD simulations.

4.2.5 Waveguide Loss

Waveguide run-out measurement loops with propagation distances on the order of 100 μm were fabricated in order to obtain a measure of waveguide propagation loss on the chip (see Fig. 4.8(a)). Fig. 4.8(b) shows transmission data from 270 nm ridge waveguide run-outs as a function of waveguide length. A linear fit indicates a waveguide propagation loss of 19 $\pm$ 2 dB/mm. 160 nm ridge waveguide runouts were also fabricated in order to help quantify the sources of loss (GaP vs. top/bottom sidewalls vs. lateral sidewalls), but the yield was too low (or the loss too high) to extract a meaningful loss value. It may still be possible to obtain these values with only the 270 nm ridges by repeating the measurement with TM-polarized light. However these measurements have not yet been carried out, and if the loss is much larger for TM modes it will be very difficult to extract meaningful results.

4.3 Summary

We have presented chip-scale transmission measurements of five key components of an integrated photonics platform for NV-center-based quantum information. This type of large-scale

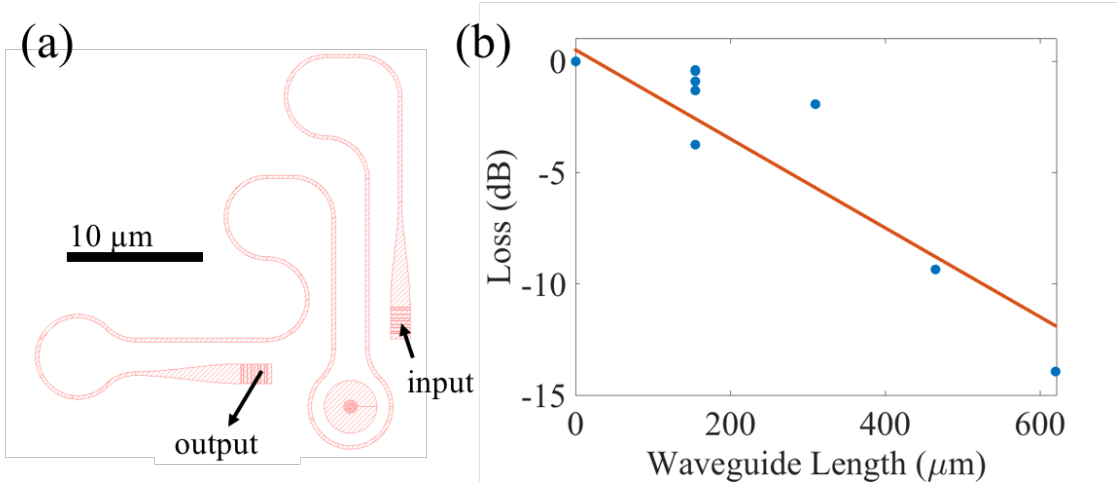

Figure 4.8: (a) Scaled top view of a waveguide-loss measurement loop. (b) Waveguide loss measurements obtained from 270 nm ridge run-outs. The red curve represents a linear fit.

integration and testing is expected to be critical to the development of scalable NV-center-based MBQIP. Yield and performance of integrated classical optical components will need to be well characterized and optimized in order to facilitate the more difficult-to-engineer coupling of single NV centers to individual resonators.

While the primary goal of this work was to set a benchmark for large-scale integration in the GaP-on-diamond material platform, the demonstrated device performance suggests there are already areas where the platform should provide large advantages relative to free-space techniques. The measured quality factors of the waveguide-coupled resonators, along with relatively large output coupling, should allow for total quantum efficiency into useful waveguide modes of around 33%. This represents a potential improvement by a factor of more than 200 over what has been demonstrated with free-space optics. Further, the combined yields and device performance of the three demonstrated components are sufficient to allow the integration of elements for a spin entanglement protocol, with significant total quantum efficiency advantages and reasonable yield.

Table 4.2 summarizes the expected total quantum efficiency (η) and full-circuit yield for

two simple systems. The first system consists of two separate collection channels, each made up of a waveguide-coupled resonator and an output grating. In order to generate entanglement with this system, both photon interference and single-photon detection would need to be performed off-chip. The second system consists of two waveguide-coupled resonators connected to a directional coupler, with a single grating coupler at one of the output ports. In this case, photon interference is performed on chip and single-photon detection could be performed on-chip by replacing the grating coupler with an integrated detector. This would enable leveraging of the higher on-chip total quantum efficiency (η_{wg}), compared with off-chip coupling. The reported yield and performance values for the second system assume that all four output ports would be fabricated, but require only that a single output port works. Schematics of both circuits are illustrated in Fig. 4.9.

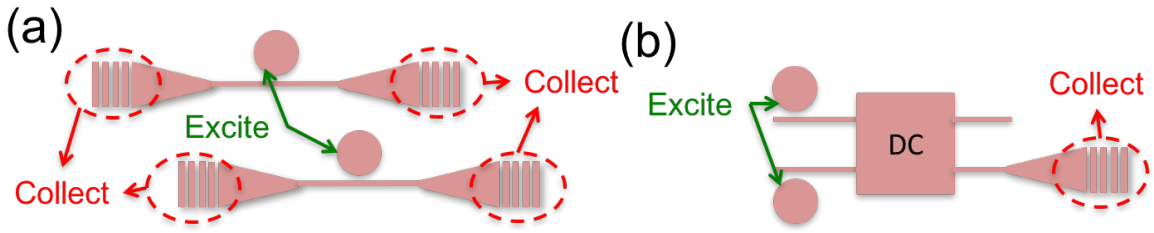

Figure 4.9: Schematic illustration of two small systems for which expected performance and yield values are presented in Table 4.2.

System	η	$\eta_{\mathbf{wg}}$ **(on-chip)**	Yield
(a)	5.5%	33%	15%
(b)	1%	6.5%	22%

Table 4.2: Expected yield and efficiency for simple two-qubit systems.

Chapter 5

WAVEGUIDE-COUPLED ZERO-PHONON-LINE PHOTONS FROM SINGLE NV CENTERS

5.1 Introduction

As discussed in previous chapters, one of the most important metrics for the GaP-on-diamond platform is the total quantum efficiency of ZPL photons collected into a waveguide mode (η). While calculations of theoretical η values such as the one presented in Chapter 4 are useful, direct measurements of waveguide-coupled photo-emission from single NV centers are required to confirm the potential of the fabricated devices. The remainder of this chapter details such measurements performed on waveguide-coupled disk resonators, indicating total quantum efficiencies as high as $\eta \approx 9\%$.

5.2 Measurement Setup

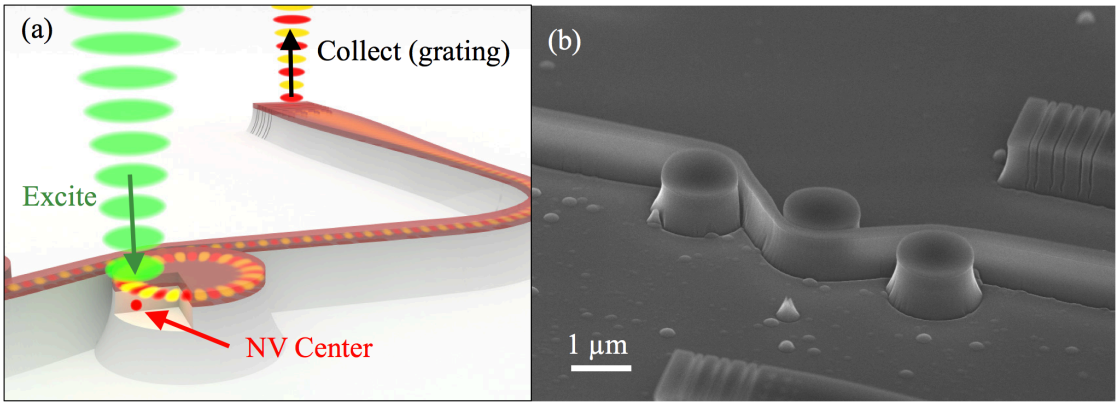

Figure 5.1: (a) Illustration of device measurement showing grating-collection. (b) Scanning electron microscope image of fabricated devices.

Measurements were performed with the fabricated devices cooled to 8 K. For each device, the resonator mode was first tuned to the ZPL resonance. Tuning was accomplished via xenon gas deposition, which causes the cavity modes to red-shift and provides a wavelength tuning range of $\sim$2 nm. For cavity tuning measurements, the sample was excited at normal incidence and fluorescence spectra were collected from the output grating coupler as illustrated in Fig. 5.1(a). An example tuning curve which shows clear NV-cavity coupling as the cavity is tuned to the NV ZPL resonance is shown in Fig. 5.2(a). This initial tuning measurement was performed on approximately 80 devices expected to lie within the cavity tuning range of the ZPL wavelength, for four different excitation locations around the perimeter of each disk. In this way, a subset of devices showing coupled ZPL emission were identified for further study. Three additional types of measurement were performed on devices in this subset: photon auto-correlation ($g^{(2)}$) on the grating-coupled ZPL emission to confirm the single-photon nature of the collected fluorescence, power dependence to determine saturated collection rates, and lifetime measurements to quantify the resonant enhancement of the ZPL emission. As we show below, the last two measurements enable two separate estimates of η for each device.

5.3 Results

5.3.1 Photon Autocorrelation Measurements

With a cavity mode tuned onto resonance with a selected ZPL, we first performed a $g^{(2)}$ measurement to verify the single-emitter nature of the source (see inset Fig. 5.2(b)). The grating-collected light was spectrally filtered around the selected ZPL wavelength before detection as depicted in Fig. 5.2(b). The $g^{(2)}$ measurement was performed on 4 of the brightest devices, all showing auto-correlation dips with $g^{(2)}(0) < 0.4$, indicating that in each device a majority of the collected photons are from a single emitter (see Table 5.1). Non-zero coincidence rates are the result of background fluorescence at the ZPL wavelength. This background fluorescence can be observed in the detuned-cavity spectrum (orange) in

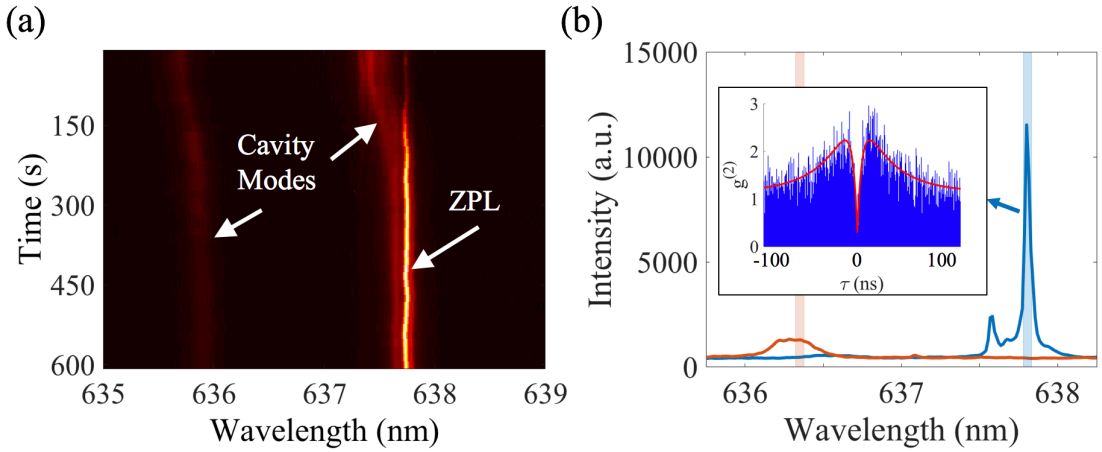

Figure 5.2: (a) Measured tuning curve showing two cavity modes as one is tuned onto resonance with a coupled NV center's ZPL. (b) Grating-collected spectra with cavity tuned onto selected ZPL (blue curve) and detuned from ZPL (orange curve), with wavelength integration range used for count rate calculation indicated by shaded rectangles. Inset: photon autocorrelation measured with cavity tuned onto ZPL, with bi-exponential fit shown in red.

Fig. 5.2(b).

5.3.2 Saturation Measurements and Count Rate Estimation

We next measured the excitation power dependence of the waveguide-coupled ZPL photon rate to determine saturated collection rates. This measurement was performed by sweeping the excitation power and measuring the grating-coupled detection rate, again spectrally filtered around the selected ZPL. After removal of the background fluorescence, measured with the cavity mode detuned from the ZPL, the data were fit to a saturation model: $\gamma(P) = \gamma_{sat}/(1 + P/P_{sat})$, where $\gamma(P)$ is the detection rate, γ_{sat} is the saturated detection rate, P is the excitation power and P_{sat} is the saturation power.

Power dependence data for 4 devices are shown in Fig. 5.3 (inset). Disk 1 shows a detected ZPL count rate of 1.2×10^4 s^{-1} after background subtraction. The fit indicates a saturated NV ZPL detection rate of 2.0×10^4 s^{-1}, and a saturation power of 3.4 mW. Using

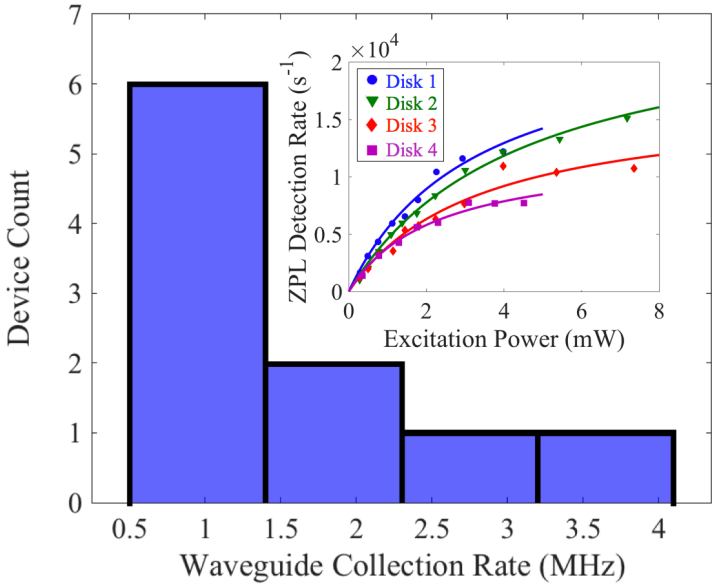

Figure 5.3: Histogram of estimated saturated collection rates into bus waveguides for 10 devices. Inset: power dependence of on-resonance NV ZPL detection rate for 4 selected devices, with background removed. Solid lines are fits to saturation model.

the measured collection path efficiency for each device and the known detector efficiency (see Section 5.3.5), we can estimate the saturated collection rate into the bus waveguide. In the case of Disk 1, the estimated on-chip collection rate is 2.5×10^6 s^{-1} from a single saturated NV center. Figure 5.3 shows a histogram of saturated on-chip collection rates for 10 devices with values exceeding 5×10^5 s^{-1}. We note that the estimated count rates for the three brightest devices are comparable to the best reported collection rates of NV ZPL photons into guided modes for all-diamond devices [40]. These count rates are also several times larger than the theoretical limit of approximately 3×10^5 s^{-1} in the absence of Purcell enhancement, calculated as 3% of a total saturated emission rate of 1×10^7 s^{-1} [59].

5.3.3 Lifetime Measurements and Determination of Purcell Factor

In order to quantify the achieved Purcell enhancement, the excited-state lifetimes of individual NV centers were measured using a directly modulated laser diode [60] with a measured fall time of 1 ns. Time-resolved measurements were taken on Disks 1-4, with the cavity on-resonance with a selected ZPL, as well as off-resonance. After careful subtraction of the background fluorescence waveform, the data were fit to exponential decay curves to obtain the lifetimes. Fig. 5.4 depicts measured on- and off-resonance time-resolved photoluminescence curves for Disks 1 and 2. Measured lifetimes under both resonance conditions were compared in order to determine the Purcell enhancement factor F_P of a given device. In the non-resonant case, the lifetime τ_0 is determined by $1/\tau_0 = \gamma_0 = \gamma_{ZPL} + \gamma_{PSB}$, in which γ_{ZPL} (γ_{PSB}) is the emission rate into the ZPL (phonon sidebands). In the resonant case, the lifetime τ_{res} is determined by $1/\tau_{res} = \gamma_{res} = (1 + F_P)\gamma_{ZPL} + \gamma_{PSB}$. For Disk 1, the measured on-resonance lifetime of 4.7 $\pm$ 0.4 ns is significantly shorter than the off-resonance lifetime of 8.7 $\pm$ 0.8 ns, with the ratio corresponding to a resonant Purcell factor of F_P = 26. This is close to the maximum possible $F_{P,max} \approx 30$ for this device geometry, given a measured quality factor of Q = 8200 [46]. We note that the off-resonance lifetimes in all four measured devices are significantly shorter than the NV lifetime in bulk diamond ($\sim$12 ns) [61,62]. The shorter lifetimes are consistent with a broadband enhancement effect caused by the NV centers' proximity to the diamond-GaP interface [63]. Modeling this effect for NV centers at distances of 0 to 20 nm from a diamond-GaP interface along a [100] plane, we expect reduced lifetimes from 8 ns to 10 ns, respectively.

The laser-diode used for lifetime measurements (PicoLas, Roithner) emitted at a wavelength of 520 nm. This was the longest wavelength laser diode commercially available to us below 600 nm. Unfortunately, the photon energy is larger than the GaP bandgap, resulting in a large increase in background fluorescence relative to NV center ZPL emission. For this reason, careful background removal was necessary in order to obtain accurate lifetime data for coupled NV centers.

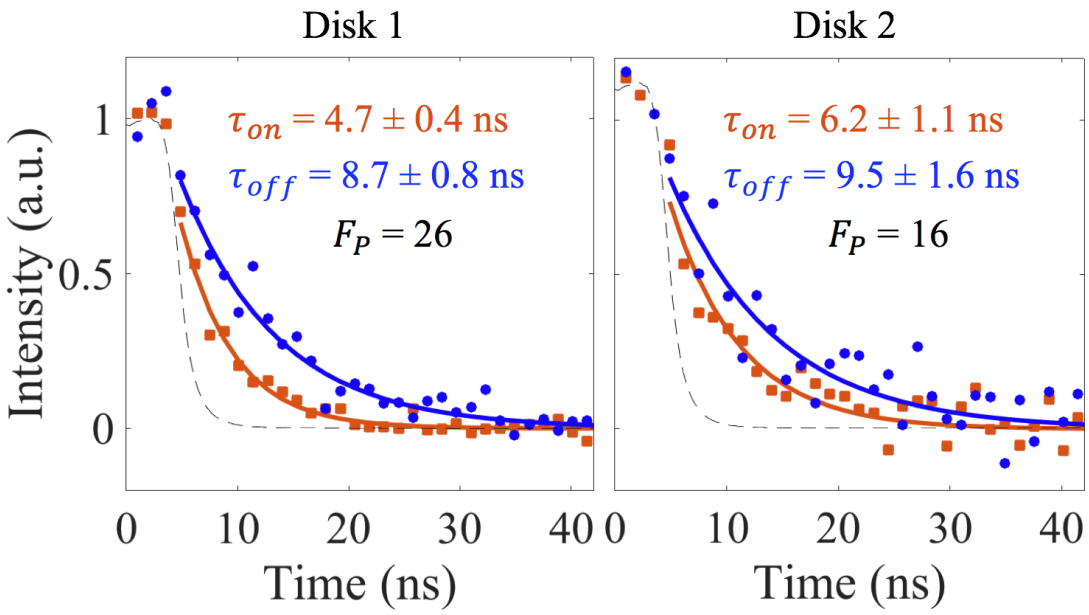

Figure 5.4: Fluorescence lifetime measurements for Disks 1 and 2, in both the resonant (orange) and off-resonant (blue) conditions. Thick lines represent exponential fits. The dashed black line is the measured system response for reflected excitation light.

Both full-signal and background-only time-resolved photoluminescence measurements were taken for each resonant state, for each device (Count Blue single-photon counting module, ID Quantique ID801). The background was then scaled to match the full-signal at times much longer than the NV lifetimes, as depicted in Fig. 5.5(a). For the on-resonance case, background-only data was taken as the cavity-mode fluorescence with the cavity detuned from the NV center's ZPL, while exciting at the NV center's location. The raw full-signal and scaled background histograms for Disk 1 (on-resonance, grating-collected) are shown in Fig. 5.5(a). Lifetimes were obtained using weighted exponential fits [64] after background removal (Fig. 5.5(b)).

The grating-collected cavity-mode background fluorescence showed two distinct lifetime scales, one on the order of a nanosecond (possibly measurement-limited) and a second on the order of ∼30 ns. This longer-lived background fluorescence is greatly reduced when

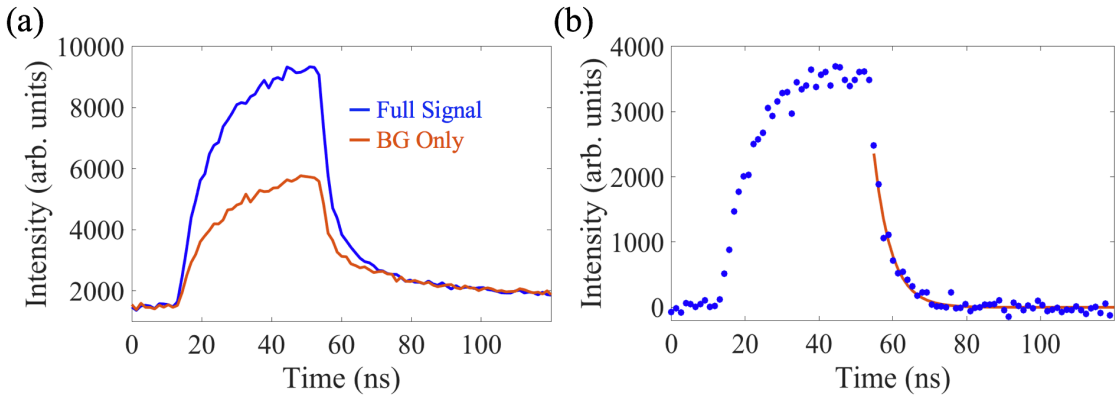

Figure 5.5: (a) Full signal time-resolved fluorescence data for Disk 1 (blue curve) and background-only data (orange curve). (b) Time-resolved fluorescence after background removal, with a single exponential fit (orange curve).

exciting on other parts of the disk off of the NV center's location, or when collecting at a wavelength away from the cavity mode resonance. This indicates the coupled NV center is the source of this long-lived fluorescence, which we tentatively attribute to device-coupled phonon-sideband emission associated with the NV center's neutral charge state [65]. The faster decaying component is likely the result of either recombination via deep levels in the GaP or fluorescence from the HSQ electron-beam resist.

Note that all measured NV signal lifetimes were between 4.7 ns and 10.2 ns, significantly shorter than the long-lived component of the background photoluminescence. Further, care was taken so that experimental conditions remained as consistent as possible between associated full-signal and background-only measurements. This ensured that only small amounts of scaling were applied to background measurements (scaling factors between 0.9 and 1.3), and that background removal did not rely heavily on data scaling or fitting. Combined, these two characteristics of the measured data enabled accurate identification and subtraction of background photoluminescence from full-signal measurements.

5.3.4 Total Quantum Efficiency

The total quantum efficiency η was estimated for Disks 1-4 by two different methods. In the first method, the total saturated emission rate including phonon sideband emission, γ_{tot}, is determined using the measured on-resonance lifetime of the selected NV center and a simple 5-level population density model [66]. It is assumed that the NV centers are in the useful negatively charged state ∼70% of the time under continuous wave 532 nm excitation [67]. For a saturated on-chip collection rate of γ_{wg}, η_1 is given by

$$\eta_1 = \frac{\gamma_{wg}}{\gamma_{tot}}. \tag{5.1}$$

In the case of Disk 1, the total saturated emission rate is calculated to be 2.85×10^7 s^{-1}. The estimated saturated on-chip collection rate of 2.48×10^6 s^{-1} thus corresponds to $\eta_1 \approx 9\%$.

The second method uses the total quantum efficiency into the disk resonator mode, η_{disk}, calculated from the measured Purcell enhancement factor; and the disk-to-waveguide out-coupling efficiency, determined from grating-coupled transmission measurements (see Section 5.3.5). In this case,

$$\eta_2 = \eta_{out}\eta_{disk} = \frac{\eta_{out}F_P}{F_P + \gamma_0/\gamma_{ZPL}}, \tag{5.2}$$

where η_{out} is the disk-to-waveguide out-coupling efficiency and $\gamma_0/\gamma_{ZPL} \approx 30$. We first use the measured Purcell factor to calculate the total quantum efficiency into the disk (η_{disk}) as:

$$\eta_{disk} = \eta_{ZPL}\eta_{mode} = \left(\frac{(F_P+1)\gamma_{ZPL}}{(F_P+1)\gamma_{ZPL} + \gamma_{PSB}}\right)\left(\frac{F_P}{F_P+1}\right) = \frac{F_P}{(F_P + \gamma_0/\gamma_{ZPL})}, \tag{5.3}$$

where η_{ZPL} is the proportion of photons emitting at the ZPL wavelength, η_{mode} is the proportion of ZPL photons emitting into the disk mode, F_P is the Purcell factor and $\gamma_0(\gamma_{ZPL}, \gamma_{PSB})$ is the total radiative emission rate (ZPL emission rate, phonon-sideband emission rate). Transmission measurements are used to obtain the disk-to-waveguide out-coupling efficiency η_{out},

$$\eta_{out} = \frac{Q}{Q_c}, \tag{5.4}$$

where Q is the measured quality factor. The coupling-limited quality factor Q_c can be calculated numerically using:

$$Q_c = Q\left(\frac{1-t}{1-\gamma t}\right), \tag{5.5}$$

$$\frac{T_{res}}{T_0} = \frac{(t-\gamma)^2}{(1-\gamma t)^2}, \tag{5.6}$$

where t (γ) is the field transmission coefficient through the coupling region (resonator mode round trip), and T_{res}/T_0 is the normalized transmission at the resonance-dip minimum. All 4 devices for which η_{out} was calculated were determined to be under-coupled based on large-scale transmission measurements [36]. In the case of Disk 1, η_{disk} was calculated to be 46% and η_{out} was determined to be 20%. The resulting estimated total quantum efficiency is $\eta_2 \approx 9\%$, in agreement with η_1. Table 5.1 summarizes the estimated total quantum efficiency obtained using both methods for 4 devices, showing reasonable agreement between the two.

Device	$\gamma_{\mathbf{tot}}(\mathbf{s^{-1}})$	$\gamma_{\mathbf{wg}}(\mathbf{s^{-1}})$	$\eta_{\mathbf{1}}$	F_P	$\eta_{\mathbf{out}}$	$\eta_{\mathbf{2}}$	$g^{(2)}(0)$
Disk 1	2.85×10^7	2.48×10^6	9%	26	20%	9%	0.30
Disk 2	2.15×10^7	2.17×10^6	10%	16	23%	8%	0.36
Disk 3	1.85×10^7	1.48×10^6	8%	12	12%	3%	0.19
Disk 4	2.49×10^7	9.72×10^5	4%	16	12%	4%	0.31

Table 5.1: Summary of key values for 4 selected devices.

For some disks, there is a discrepancy between the two estimation methods. Small discrepancies, as seen in Disk 2, can be attributed to uncertainty in both the NV center charge state ratio and the lifetime measurement. However in the case of Disk 3, the large discrepancy ($\eta_1 \approx 8\%$ vs. $\eta_2 \approx 3\%$) is primarily due to the input grating coupler being visibly broken. On-chip loss estimates assume that input and output coupling efficiencies are the same for a given grating coupler (see Section 5.3.5). This is a reasonable assumption for

devices well mode-matched to the input beam. However in the case of the broken input coupler for Disk 3, the grating output mode was not well matched to the microscope input beam, leading to an over-estimate of on-chip loss and an associated over-estimate of η_1.

5.3.5 Collection Path Efficiency

In order to obtain accurate estimates of waveguide collection rates, the collection path efficiency (η_{cp}) from the coupled section of the waveguide to the off-chip detector was measured for each device. The collection path can be separated into 2 main components: the chip and the microscope. The microscope collection path efficiency (η_{mic}) is assumed to be the same for all devices, and was measured by passing a laser beam ($\lambda \approx 640$ nm) through the system, and measuring the input and output power. The measured efficiency of the microscope was approximately $\eta_{mic} = 35\%$, with the majority of the losses coming from the grating spectrometer used for spectral filtering of the ZPL ($\eta_{spec} = 45\%$).

The chip efficiency (η_{chip}) was determined for each device individually. First, grating-coupled transmission measurements were performed and the results were normalized to power reflected from a polished diamond surface (Fig. 5.6(a)). In order to account for differences between the 'input-to-device' (η'_{chip}) and 'device-to-output' (η_{chip}) efficiencies, emission was measured from each grating coupler while exciting background fluorescence in the selected device (Fig. 5.6(b)). Using these two measurements, the chip efficiency (assuming collection through the output grating coupler) was determined as:

$$\eta_{chip} = \sqrt{TR}, \tag{5.7}$$

where $T = \eta_{chip}\eta'_{chip}$ is the measured transmission, and $R = \eta_{chip}/\eta'_{chip}$ is the ratio of background fluorescence intensity from the output/input grating couplers. In the case of Disk 1, the transmission at the ZPL wavelength (λ_{ZPL}) was determined to be $T = 0.01$, and the output-to-input ratio was $R = 1.65$, yielding an on-chip efficiency of $\eta_{chip} = 12.8\%$.

Combining the measured chip and microscope efficiencies, as well as the known spec-

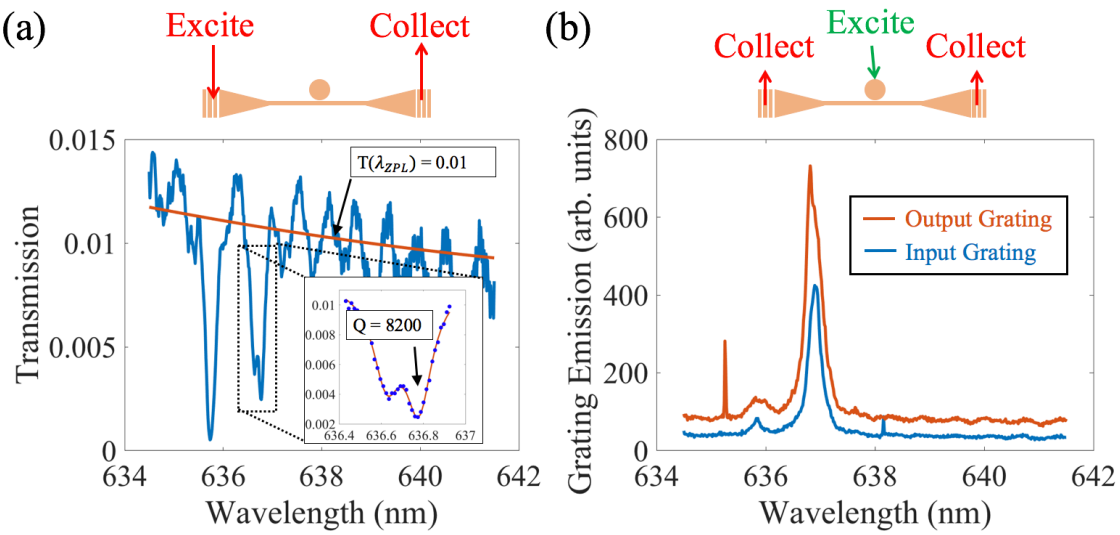

Figure 5.6: (a) Measured transmission spectrum for Disk 1 showing Mie splitting, a quality factor of Q = 8200, and a transmission value of 0.01 at the ZPL wavelength (λ_{ZPL}). A shorter-wavelength resonance dip visible at $\lambda = 635.8$ nm is due to another disk coupled to the same waveguide. (b) Emission spectra from input and output grating couplers, showing an output efficiency ratio R = 1.65. Top schematics: measurement setup in each case.

trometer CCD detection efficiency of $\eta_{det} = 0.4$, we determine the total optical loss in the measurement. The total collection-path efficiency for a photon collected into the waveguide is given by:

$$\eta_{cp} = \frac{1}{2}\eta_{chip}\eta_{mic}\eta_{det} \tag{5.8}$$

where the factor of 1/2 is included to account for the equal number of photons collected in the waveguide's counter-propagating mode. This assumes optical reciprocity and the electric dipole nature of NV-center emission. The total collection-path efficiency for Disk 1 calculated in this way is $\eta_{cp} = 0.9\%$.

5.4 Summary

We have shown that large η values are achievable in a GaP-on-diamond platform, using devices that can be readily integrated into larger on-chip photonic networks. A reasonable excitation repetition rate for NV-NV entanglement is 100 kHz, limited by the NV initialization time [28]. If all waveguide-coupled photons are detected and indistinguishable, the demonstrated collection efficiency of 9% would correspond to an NV-NV entanglement generation rate of 400 Hz, which significantly exceeds the $\sim$1 s electron spin decoherence rate [13]. We note that the GaP-on-diamond system is compatible with waveguide-coupled superconducting detectors, a technology which has already demonstrated detection efficiencies exceeding 90% for waveguide-coupled photons [44, 45].

The demonstrated Purcell factors, as high as 26, exceed what has been achieved in all-diamond waveguide-integrated platforms [40, 68]. This suggests that the primary disadvantage of the hybrid materials system for MBQIP, namely that the emitter cannot be placed at the guided-mode maximum, can be largely overcome with continued improvements in resonator quality factor. A greater challenge for all integrated platforms is the production of indistinguishable photons. Specifically, it will be necessary to improve the spectral stability of near-surface NV centers, which currently exhibit spectral diffusion up to 10 GHz [48]. We are encouraged by recent work in improving NV spectral stability via high-temperature annealing [69] and longer-wavelength excitation [28]. Moreover, even if device-integrated NV centers do not exhibit the spectral stability observed for bulk NV centers incorporated during diamond growth, the platform is compatible with Stark tuning for both active ZPL frequency stabilization [70] and tuning to a single platform resonance [27, 71].

Chapter 6

OUTLOOK

Previous chapters have detailed the development of the GaP-on-diamond platform, specifically the development of basic integrated photonic components necessary for the realization of on-chip quantum information processing. The two key results are the proof-of-principle measurement of high-efficiency on-chip collection of ZPL photons from device-coupled NV centers (Chapter 5), and the large-scale integration and testing of hundreds of component devices (Chapter 4). Importantly, both results were demonstrated on the same GaP-on-diamond chip.

Continued progress toward the long-term goal of on-chip entanglement generation will benefit greatly from improvements in demonstrated device performance and yield, and will require the development of several additional functionalities. The remainder of this chapter presents engineering goals in both catergories.

6.1 Performance and Yield Improvements

While demonstrated devices exhibited performance that should enable entanglement at rates far exceeding what is possible with free-space optics, further improvements will be highly desirable as more complex photonic circuits are integrated into the GaP-on-diamond platform. Probably the single most important metric to improve is the Purcell factor. Not only will increasing the Purcell factor enable higher quantum efficiency, but it will also improve the signal-to-background ratio which will reduce the spectral filtering requirements necessary for on-chip entanglement generation. Additionally, increases beyond the demonstrated value of $F_P = 26$ will cause a broadening of the lifetime-limited ZPL bandwidth, reducing the spectral stability requirements of implanted NV centers for Hong-Ou-Mandel photon-interference

experiments.

There are two clear paths to increasing the Purcell factor in our devices: optimizing resonant mode field distributions, and improving resonator quality factors. As can be seen in Fig. 3.3, a factor of >3 increase in Purcell factor may be possible through optimization of the resonant mode geometry. In particular, making use of a thinner GaP membrane will simultaneously increase NV-mode interaction and reduce mode volume. However, there will also be an increased mode interaction with the top and bottom GaP surfaces that may result in reduced quality factor. Future waveguide-loss experiments should allow for this tradeoff to be well-characterized.

Resonator quality factor can likely be improved in two ways. First, as indicated in Section 4.2.1, current devices appear to have excess loss in the coupling region. Intrinsic quality factors can likely be increased by at least 40% simply by increasing the disk-to-waveguide separation. Second, improvements in waveguide loss will translate directly to increased intrinsic quality factors. Un-coupled disk resonators with quality factors exceeding 200,000 have been demonstrated using similar GaP material [72], suggesting that large improvements should be possible through process engineering. In particular, the diamond surface on which our devices were fabricated had polish-marks visible to an SEM. This roughness is likely contributing to waveguide loss and can be improved with plasma etching [69]. It is also likely that lithography-induced lateral sidewall roughness is contributing to waveguide loss, and can be improved through lithography and resist reflow techniques. It should be noted that the latter is not compatible with the HSQ resist used in this work.

Improving device uniformity can be achieved through the use of larger-area substrates: the current 2-mm squares result in an uneven spin-coated resist layer due to surface-tension effects at the chip edges. Eventually moving to larger, commercially available 4.5 mm square diamond substrates should greatly improve the resist uniformity and as a result, the uniformity of fabricated devices.

Demonstrated device yields for key passive photonic components exceeded 50%, likely limited by mechanical damage and/or particulate matter deposited on the chip. These yields

can be increased with improvements in the fabrication process. The yield for resonators with well-coupled NV centers was significantly lower (∼12%), and was primarily limited by the low NV-to-disk coupling yield. In the near-term, this yield can be improved by increasing the surface density of NV centers. Longer-term, aligned implantation may lead to further improvements [69].

6.2 Additional Functionality

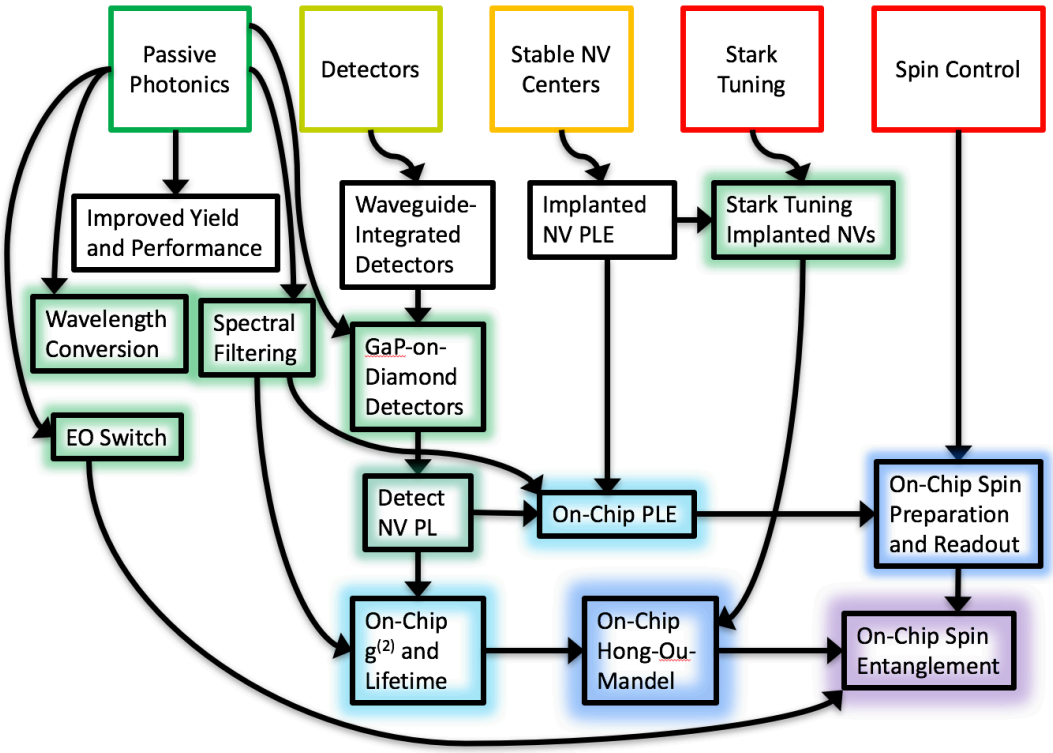

Figure 6.1: Flow-chart outlining future work and results. The top row of text-boxes represents the current state of the platform, with color indicating readiness for future steps (green represents fully ready and red represents not at all ready). Glowing boxes represent major steps, with glow color representing a rough estimate of time to result (from green representing ∼1 year, to violet representing >3 years).

The flow chart shown in Fig. 6.1 outlines additional functionalities that will benefit the

long-term goal of on-chip entanglement generation, how they relate to one another, and how desired future results may depend on them.The remainder of this section discusses the prospects for developing several of these functionalities including on-chip detection, spectrally stable photo-emission from implanted NV centers, integrated Stark tuning, and electro-optic switching.

6.2.1 Single Photon Detection

Two motivating factors for integrating photonics with NV centers are the large achievable ZPL photon collection efficiencies and the scalability of classical photonic infrastructure. Properly leveraging these advantages will require the integration of on-chip single-photon detection. One promising approach is to use waveguide-integrated superconducting nanowires [43–45, 58, 73]. Upon absorption of a photon, a section of the nanowire will briefly lose superconductivity. If a bias current is applied, this will result in a voltage pulse which can be read out electronically and counted as a photon detection event. Fig. 6.2(a) shows a schematic top-view of a waveguide-coupled superconducting nanowire single-photon detector. At the time of writing of this dissertation, superconducting nanowires had been fabricated on epitaxial GaP, and normal incidence photon detection had been observed in the lab (see Figs. 6.2(b-c)).

6.2.2 NV Center Spectral Stability

Photon-mediated spin entanglement generation has so far only been demonstrated with NV centers occurring during diamond growth, several microns away from any surface [27–29]. This is due to the large spectral diffusion (on the order of 10 GHz) typically observed with shallow implanted NV centers [48]. Indeed, shallow NV centers coupled to GaP-on-diamond devices have been observed to exhibit spectral diffusion as large as 30 GHz (see Fig. 6.3(a)). While entanglement generation is possible with such centers, it would require either spectral filtering or time-gated detection of emitted ZPL photons. The implementation of either of these strategies will reduce the achievable entanglement generation rate, and can treated

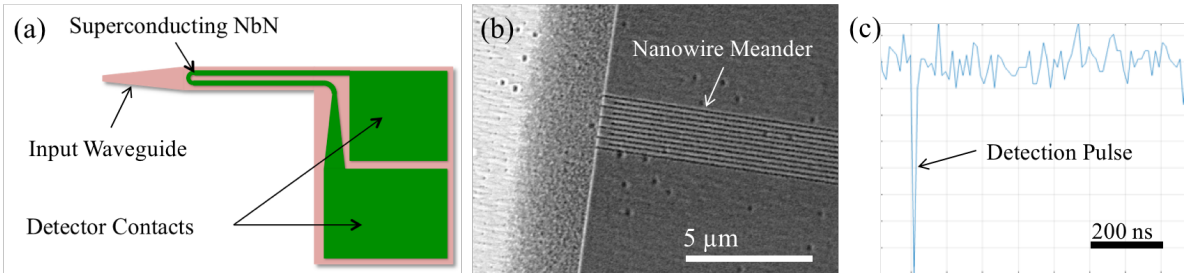

Figure 6.2: (a) Schematic top-view of proposed on-chip single-photon detector based on waveguide-coupled superconducting nanowire. (b) SEM image of preliminary superconducting nanowire meander on GaP, aimed at vertical incidence detection. (c) Oscilloscope waveform showing single-photon detection from devices shown in (b). Devices fabricated and tested by S. Chakravarthi.

as a reduced effective total quantum efficiency $\eta_{eff} \approx \eta/(1 + 2\pi\tau\Delta f_{sd})$, where τ is the NV center's lifetime and Δf_{sd} is the frequency spread due to spectral diffusion. In order to preserve high efficiency in an entanglement generation scheme, spectral diffusion will need to be made smaller than the lifetime-limited single-photon bandwidth. As mentioned in Section 6.1, broadening the lifetime-limited bandwidth through increased Purcell factors will help. However it is unlikely that lifetime-limited ZPL bandwidths greater than a few hundred MHz can be achieved in the platform.

There is thus a need to improve the spectral stability of implanted NV centers to <100 MHz. Promising results have been demonstrated in obtaining spectrally stable near-surface implanted NV centers by removing damage associated with surface polishing and implantation [69]. This is achieved through a combination of plasma etching to remove the top few μm from a polished diamond surface, and very high temperature annealing (1200° C). At the time of writing of this dissertation, initial experiments developing plasma etch recipes and annealing recipes have been performed.

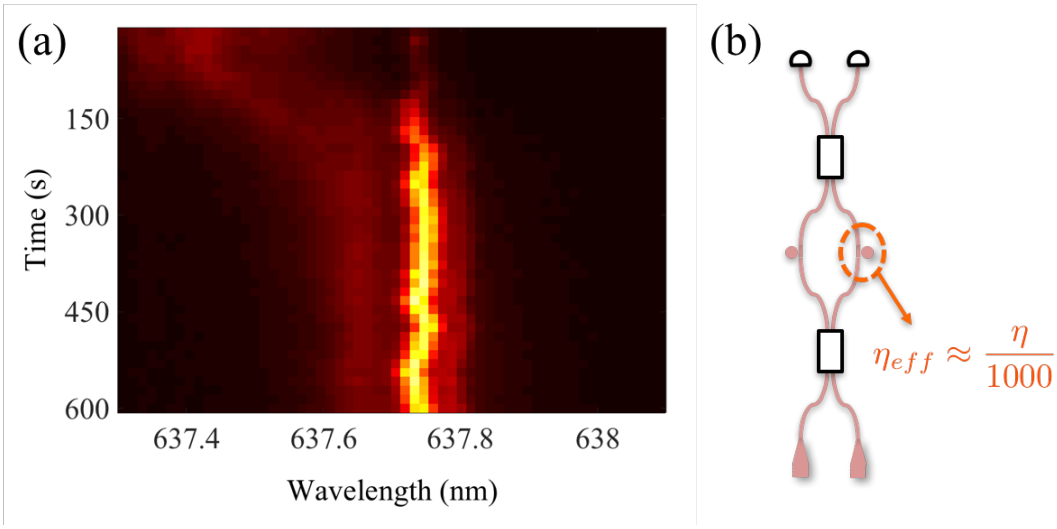

Figure 6.3: (a) Spectral zoom on tuning curve from Chapter 5 showing time-variation in the coupled ZPL wavelength (frequency). Here, a wavelength variation of $\Delta\lambda = 0.05$ nm corresponds to a frequency variation of $\Delta f = 37$ GHz. (b) Schematic of entanglement-generation circuit illustrating the effect of spectral diffusion, which can be treated as an effective total quantum efficiency η_{eff}.

6.2.3 Stark Tuning

Current device-coupled NV center measurements were enabled by tuning disk resonances to the selected emitter's ZPL. In this way, untuned resonator frequencies only needed to fall within ∼1 THz of a coupled emitter's ZPL. This was important given that ZPL frequencies varied by as much as 2 THz from device to device. However, this strategy will not be suitable for entanglement generation, as the targeted NV centers will need to have indistinguishable emission spectra. This could be accomplished in our platform by building identical cavities with resonances near the expected ZPL frequency, and independently tuning the coupled NV centers to the 'system frequency'. Specifically, we propose to tune NV centers using the Stark effect, wherein an applied DC electric field shifts the energy levels (and thus emission frequency) of a localized electron system (NV center). This effect has been used to tune the ZPL frequency of an NV center by 200 GHz, as well as to implement a frequency stabilizing

feedback system [70]. Implementing Stark tuning into the GaP-on-diamond platform will require fabricating metal electrodes around the NV-coupled devices, as illustrated in Fig. 6.4.

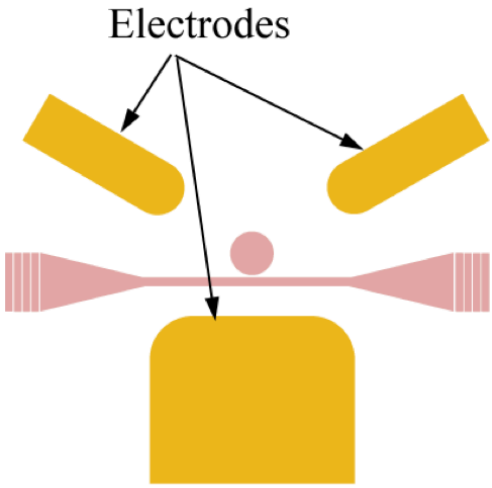

Figure 6.4: Schematic top-view of eventual device-integrated Stark tuning electrodes.

6.2.4 Electro-Optic Switching

On-chip optical switching will be important for at least two reasons: it will allow for mitigation of non-unity yield in critical devices by enabling post-selection (Fig. 6.5), and it should enable reconfigurability for efficient entanglement generation between multiple NV centers.

We propose to make use of the known electro-optic effect in GaP to fabricate electro-optic switches in the GaP-on-diamond platform. GaP exhibits an electro-optic coefficient $r_{41} \approx 1 \times 10^{12}$ m/V [42], and has a breakdown field of approximately 1×10^8 V/m [74]. Diamond can exhibit breakdown fields as high as 5×10^8 V/m [75]. Thus if we assume a well confined mode, an applied field strength of approximately 10% the breakdown field of GaP, and a $\langle 100 \rangle$ surface, we can obtain a reasonable estimate of the possible shift in effective

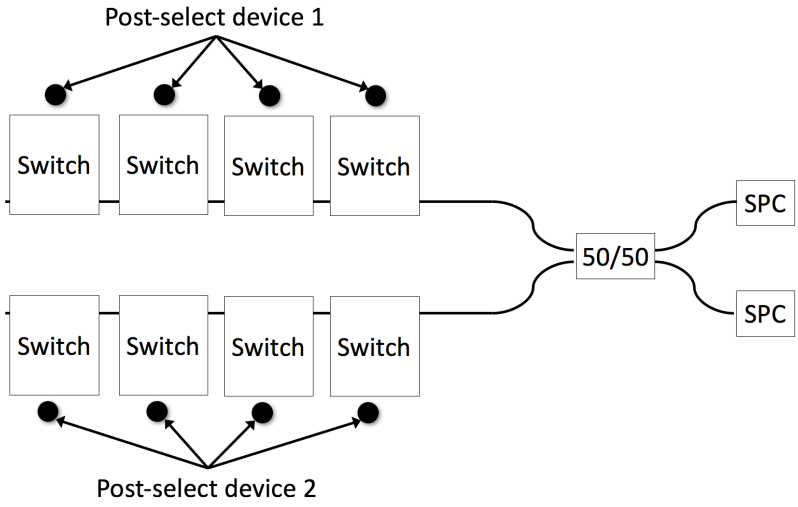

Figure 6.5: Schematic of circuit using candidate pools and switch-enabled post-selection for low-yield devices.

index. An expected possible index shift of $\sim 2 \times 10^{-4}$ is obtained, according to:

$$\Delta n_{eff} \approx \Delta n_{GaP} = \frac{1}{2} n_{GaP}^3 r_{41} E_{DC}, \tag{6.1}$$

where E_{DC} is the applied DC field. The shift in resonant wavelength for a resonator whose entire mode undergoes an equal index shift can be obtained using:

$$\Delta \lambda_{res} = \lambda_{res} \frac{\Delta n_{eff}}{n_{eff}} \tag{6.2}$$

For a resonant wavelength near 637 nm and a realistic effective index of $n_{eff} = 2.6$, the calculated change in effective index would correspond to an achievable shift in resonance of approximately 50 pm, and thus a total tuning range of 100 pm (using positive and negative bias voltages). This is enough to allow switching with an extinction ratio of 10, for device quality factors of Q $\geq$ 10,000. This should be achievable given 1.3-μm disks with measured quality factors exceeding 10,000.

Due to the nature of the non-linearity and the orientation of current GaP membranes, electro-optic switches will only be possible for TE-polarized modes, and out-of-plane applied

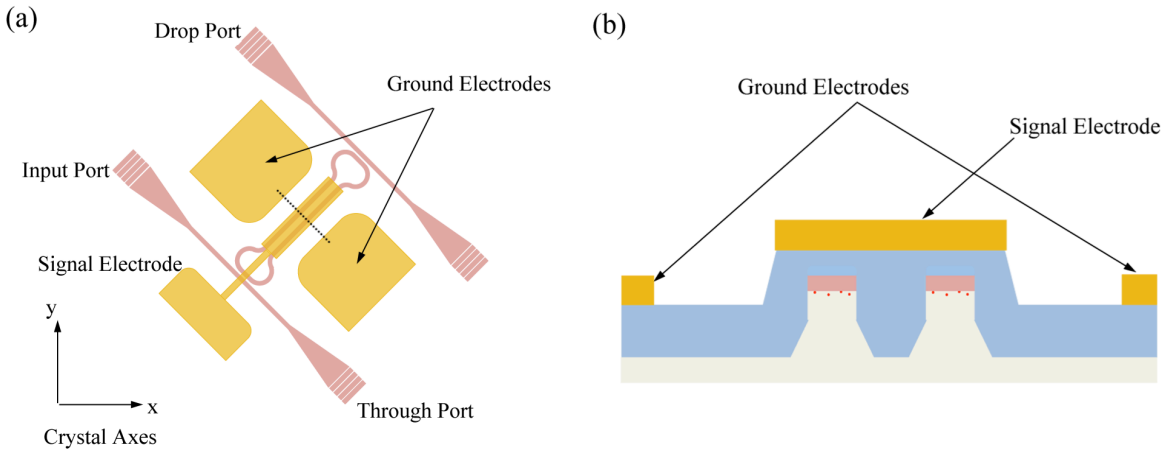

Figure 6.6: (a) Schematic top-view of preliminary electro-optic switch design. Note the specification of GaP crystal axes. (b) Schematic cross-section showing electrode height difference enabled by conformal oxide deposition, and facilitating vertical modulation fields.

fields. Furthermore resonators will need to be stretched along a single axis as much as possible; for in-plane propagation and a uniform out-of-plane applied field, light travelling along perpendicular axes will see equal and opposite shifts in refractive index. Thus a circular resonator under such an applied field would undergo local shifts in the refractive index, but no overall shift in its spectrum. Furthermore, the selection of the axis is important: a fundamental TE mode traveling along the [100] direction will not see a shift in effective index. However, the same TE mode traveling along the [110] direction will see the maximum possible shift. Fig. 6.6 shows a preliminary design for an electro-optic switch in the GaP-on-diamond platform.

6.3 Conclusion

A primary goal of this work was to demonstrate proof-of-principle devices for high-efficiency ZPL photon collection into single-mode waveguides. With demonstrated on-chip efficiencies as high as $\eta = 9\%$, we have shown that high total quantum efficiency is possible in a GaP-

on-diamond material system despite the evanescent nature of the NV-to-resonator coupling. Importantly, these efficiency values extend the limit for entanglement generation rate to ∼400 Hz, which should enable the realization of many-qubit cluster states. In addition to the photon-collection devices, large numbers of passive photonic components were fabricated on the same chip, indicating the potential for integration of single NV centers with larger photonic circuits such as the entanglement-generation circuit shown in Fig. 1.4.

As discussed in Section 6.1, improvements in yield and individual device performance will be desirable as the project moves toward the long-term goal of scalable on-chip entanglement generation. Here, we have laid the groundwork for this effort by demonstrating the fundamental passive photonic functionalities required. These results, combined with the potential for additional integrated functionality discussed in Section 6.2, position the GaP-on-diamond platform as a leading contender for the implementation of solid-state quantum networks.

Part II

A MAGNETO-OPTICAL MICROSCOPE FOR BIOLOGICAL SENSING AND IMAGING APPLICATIONS

Chapter 7

INTRODUCTION

7.1 Magnetometry with NV Centers

As mentioned in Part I, Chapter 1, NV centers can be used for high-sensitivity magnetometry. A number of sensing schemes have been demonstrated, including single NV sensing [11, 76, 77], scanning probe imaging [78] and AC and DC wide-field imaging [79–81]. An enabling characteristic of NV centers is that their photoluminescence can depend on the local magnetic field, which in particular allows for optical imaging of magnetic fields. Here, we exploit this property of NV centers to detect super-paramagnetic nanoparticles (SPNs) in wide-field photoluminescence images obtained using a conventional fluorescence microscope. This technology has applications in biology, wherein super-paramagnetic nanoparticles (SPNs) can be used as tags to detect and track bio-molecules. The main goal of this work was to demonstrate SPN detection, while keeping the system compatible with future biological integration. The principle, illustrated in Fig. 7.1, is to make use of a thin, dense sheet of near-surface NV centers to image magnetic field disturbances caused by SPNs.

SPNs offer several advantages over conventional fluorescent tags for biological applications. They are detected magnetically, and thus the biological system under investigation can theoretically be completely isolated from optical fields, reducing undesired optical and thermal interactions. Furthermore, while the majority of biological samples exhibit fluorescence, they typically do not exhibit magnetism, potentially allowing for higher background contrast in SPN-based sensing schemes. Finally, SPN tags may allow for spatial manipulation of tagged molecules and removal of unbound tags through the application of a magnetic field gradient [82, 83].

Several SPN detection schemes have previously been demonstrated, such as giant magneto-

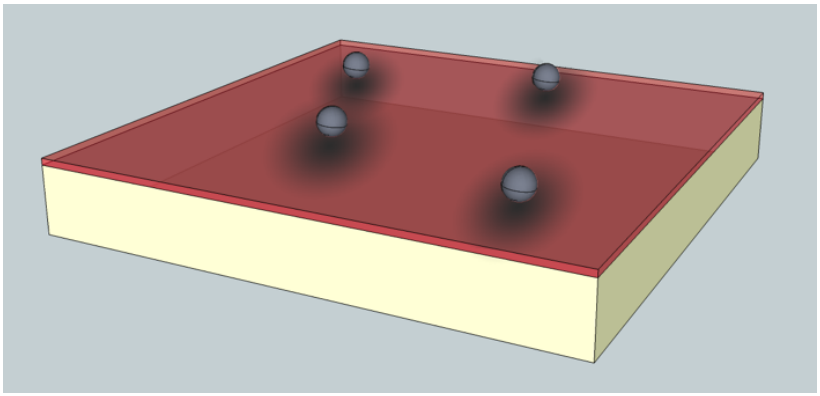

Figure 7.1: Illustration of thin sheet of near-surface NVs (red layer) in a diamond chip. Fields from the SPNs cause a change in photoluminescence emitted from layer, shown here as darker areas in the NV sheet. Note that illustration is not to scale and in reality, the areas of change in photoluminescence are much larger than the SPNs.

resistive (GMR) sensors [84, 85], magnetic force microscopy (MFM) [86], superconducting quantum interference devices (SQUIDs) [87], micro-Hall sensors [88,89] and magnetic tunnel junctions (MTJs) [90]. Of the methods listed above, detection of single magnetic particles with diameters under 1 μm has only been demonstrated with SQUIDS and MFM. SQUIDs require operation at cryogenic temperatures while MFM makes use of a nano-mechanical scanning probe in contact with the sensing surface. Thus, neither of these platforms is ideal for biological integration. In contrast, our system has been shown to detect single 19-nm SPNs at room temperature using wide-field imaging [91]. This is accomplished by making use of the high room-temperature magnetic sensitivity and optical spin readout provided by NV centers.

The remainder of Part II is divided into three chapters: Chapter 8 describes our magnetometry implementation; Chapter 9 details the detection results obtained with our system; and Chapter 10 discusses the outlook for this work.

Chapter 8

SYSTEM DESIGN

8.1 Optically Detected Magnetic Resonance Imaging

Magnetic detection in our system is achieved by performing optically detected magnetic resonance (ODMR) on an ensemble of NV centers. As mentioned in Chapter 1, the ground state for the NV center is a spin triplet. The $m_s = \pm 1$ spin states of the ground state triplet are degenerate under zero applied magnetic field, and split from the $m_s = 0$ spin state by an energy $E_{ss} = 11.9$ μeV due to spin-spin interactions [6, 7]. An applied DC magnetic field will cause the $m_s = \pm 1$ spin states to split with respective energy shifts of $\Delta E = \pm g\mu_B \vec{B} \cdot \hat{z}$ [80, 81], where g is the electron g-factor, μ_B is the Bohr magneton, $\vec{B}$ is the applied DC magnetic field and $\hat{z}$ is a unit vector aligned with the NV symmetry axis. Thus by detecting ΔE, the component of the applied field aligned with the NV axis can be determined.

Optical detection of ΔE is possible as a result of the decay path from the $m_s = \pm 1$ excited states, through two singlet states, to the $m_s = 0$ ground state [6, 10]. This causes the $m_s = \pm 1$ states to emit less photoluminescence (PL) relative to the $m_s = 0$ state, and also enables optical pumping to the $m_s = 0$ spin state. Under constant optical excitation, a radio-frequency (RF) magnetic field resonant with a ground state spin transition can be used to shift population to an $m_s = \pm 1$ spin state, resulting in a decrease in detected PL. An energy-level diagram and an experimental ODMR curve for an NV center under an applied magnetic field are shown in Fig. 8.1.

In this work, we performed ODMR measurements on 200-nm-thick, high-density sheets of NV centers near {111} surfaces of diamond chips. For all of these measurments, a strong uniform DC magnetic field of approximately 200 mT was applied at the sensing surface. The

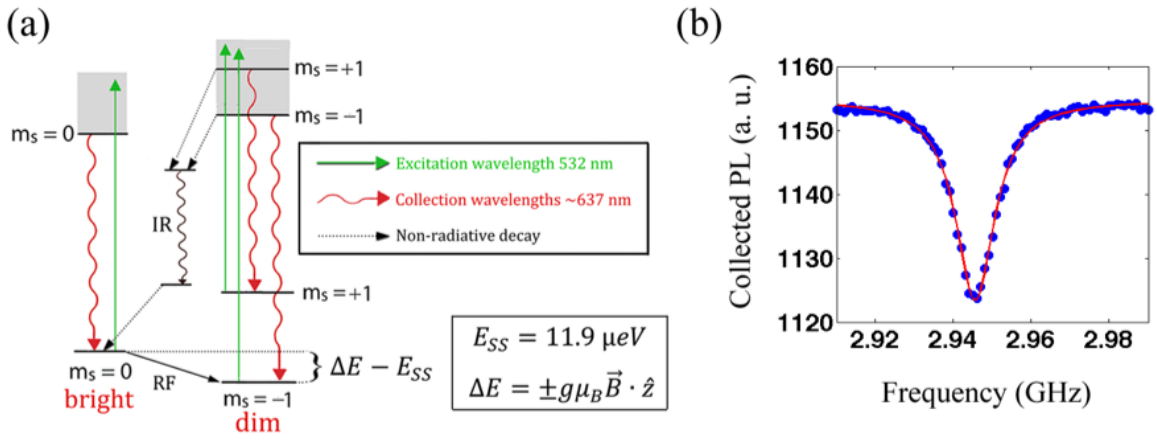

Figure 8.1: (a) Simplified energy level diagram for negatively charged nitrogen-vacancy center in diamond, under an applied DC magnetic field. Note that only zero-phonon decay is depicted and energy level spacings are not to scale. (b) Experimental ODMR curve taken under a 200 mT applied magnetic field. Blue circles are experimental data points and red curve is a Lorentzian fit.

field was aligned to the surface normal, and thus to one of the four distinguishable $\langle 111 \rangle$ NV orientations. The purpose of this applied field was twofold. First, it separated the $m_s = \pm 1$ energy levels of the NV centers aligned to the surface normal from those of the 3 other orientations. Second, it fully magnetized the magnetic material under investigation.

In order to obtain spatial distributions of the component of the magnetic field normal to the chip surface, we employed two imaging schemes, each depicted in Fig. 8.2. The first takes the difference between PL images with and without an applied RF magnetic field. We will refer to this scheme as single-frequency imaging. In the second scheme, we take the difference between PL images with the RF field applied at two different frequencies. We will refer to this scheme as two-frequency imaging.

In both cases, it can be seen that the highest small-field sensitivity is obtained by choosing f_1 (and f_2) at the steepest part(s) of the unperturbed ODMR curve, as illustrated in Fig. 8.3(a). However, for changes in magnetic field corresponding to shifts larger than the ODMR dip width, the signal is optimized by choosing f_1 at the magnetic resonance corre-

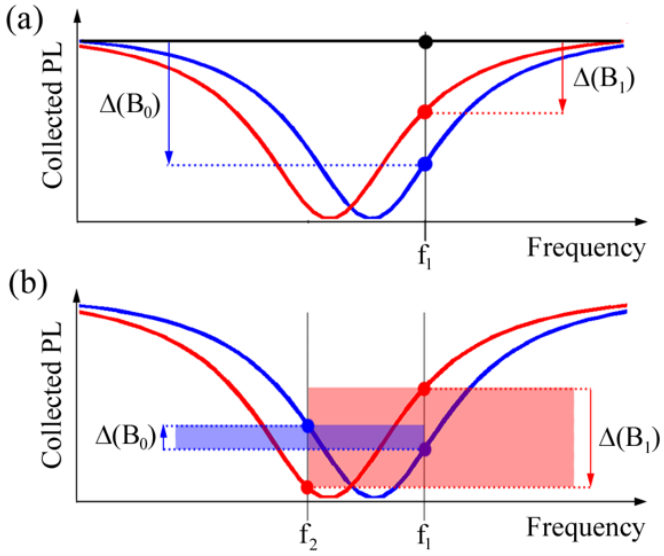

Figure 8.2: Illustrations of (a) single-frequency imaging and (b) two-frequency imaging. Blue curves represent ODMR under uniform applied field B_0; red curves represent ODMR under a field B_1, resulting from a small perturbation to the uniform applied field; and black curve represents full PL (no applied RF).

sponding to the uniform background field (and f_2 at the magnetic resonance corresponding to the perturbed field), as illustrated in Fig. 8.3(b). In general, we can expect optimized sensitivity to magnetic disturbances to be obtained somewhere between these two cases. Thus, assuming SPNs cause a small but finite shift in the magnetic resonance of nearby NV centers, optimized detection is obtained for f_1 chosen at a frequency higher than the unperturbed magnetic resonance, but below the high-frequency steepest point in the unperturbed ODMR curve. Similarly, in two-frequency imaging we can expect the optimal selection for f_2 to be at a slightly frequency than the low-frequency steepest point on the unperturbed ODMR curve.

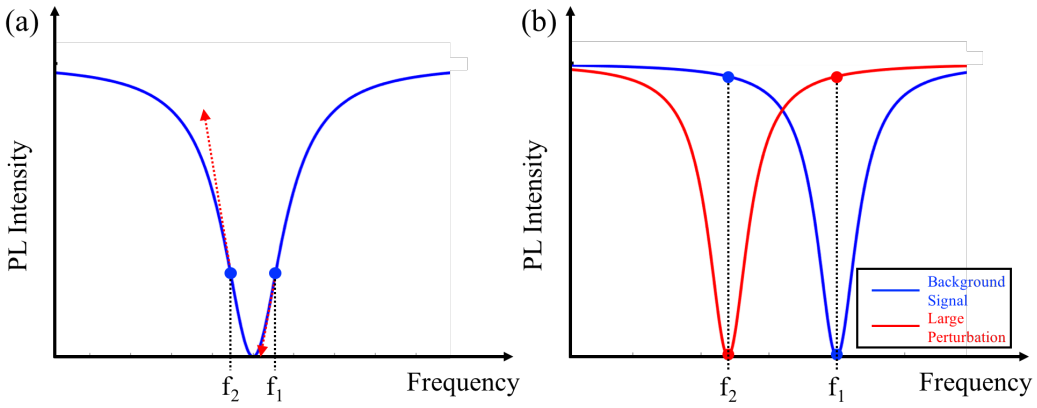

Figure 8.3: Illustrations of optimum frequency bias points for: (a) small-field sensitivity, using the highest slope points on the background ODMR curve; (b) detection of large changes in magnetic field.

8.2 Imaging System Hardware

Imaging ODMR experiments were carried out on a custom-built magneto-optical microscopy system. The system can be thought of as three sub-systems: a wide-field fluorescence microscope; a sensing chip; and an RF sub-system. The optical microscope enables optical excitation and imaging of the sensing chip, which in turn contains the near-surface NV centers on which we perform ODMR. The RF sub-system is required to address the RF spin transition between the m_s=0 and m_s=-1 ground states.

As depicted in Fig 8.4, the sensing chip sits on a co-planar transmission line, with a neodymium (Nd) magnet below, used to apply the uniform DC magnetic field. The magnet, transmission line and chip all sit on a manual x-y-z positioning stage beneath the objective of the optical microscope.

Our sensing chips were fabricated from 2-mm × 2-mm × 1-mm, type Ib, ⟨111⟩ diamond samples (Sumitomo) containing a high intrinsic concentration of nitrogen impurities (30-100 ppm). Shallow vacancies were created by implantation with 10^{11} and 10^{12} cm^{-2} N^+ ions at 50 keV. Subsequently, the chips were annealed at 900 °C for 1 hour under a 95% Ar/5%

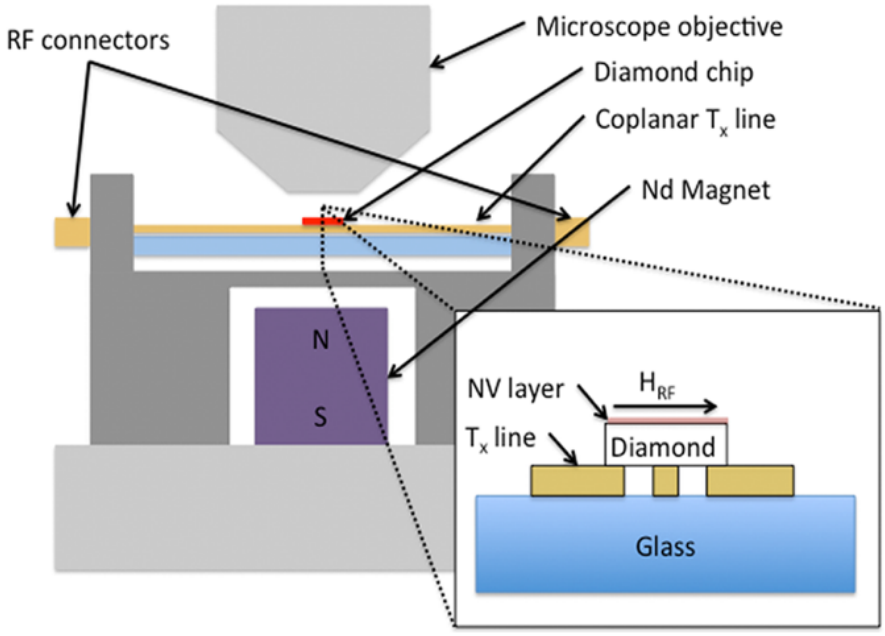

Figure 8.4: Schematic of setup under microscope objective. Inset shows cross-section of sensing chip sitting on transmission line.

H_2 atmosphere, followed by a 12-hour anneal at 450 °C in air. During the first annealing step, the vacancies diffuse to N sites, forming a layer of NV centers approximately 200 nm thick at the diamond surface [92]. The second step was used to convert neutral NV centers to the negatively charged NV centers required for this work [3, 48]. A final backside polish was performed, thinning the chips to approximately 100 μm for more efficient application of the RF magnetic field at the sensing surface, while still allowing for manual chip manipulation and mechanical stability.

The fluorescence microscope collects PL into a 0.9-numerical-aperture objective with 2-mm effective focal length (1-mm working distance). 532-nm excitation light in our system is provided by a solid-state laser, and is coupled to the microscope optics through a single-mode fiber in order to obtain a clean beam profile. The output from the fiber is focused onto the back of the microscope objective, resulting in an illuminated area with a diameter

of approximately 10 μm. A 532-nm dichroic mirror is used to separate the excitation path from the PL collection path. After passing through the dichroic mirror and a 560-nm long-pass filter, PL from the chip is imaged onto a cooled CCD. The resulting PL image has a resolution of approximately 500 nm.

The RF sub-system consists of a signal generator, a switch, a traveling-wave tube amplifier, a terminated circulator, and a custom-built co-planar transmission line. The output of the signal generator has a maximum frequency of 3.3 GHz, and is input to the semiconductor RF switch. The output of the RF switch is connected to the input of the tube amplifier, whose maximum output power is ~10 W. The terminated circulator sits between the output of the amplifier and the co-planar transmission line to absorb back-reflections.

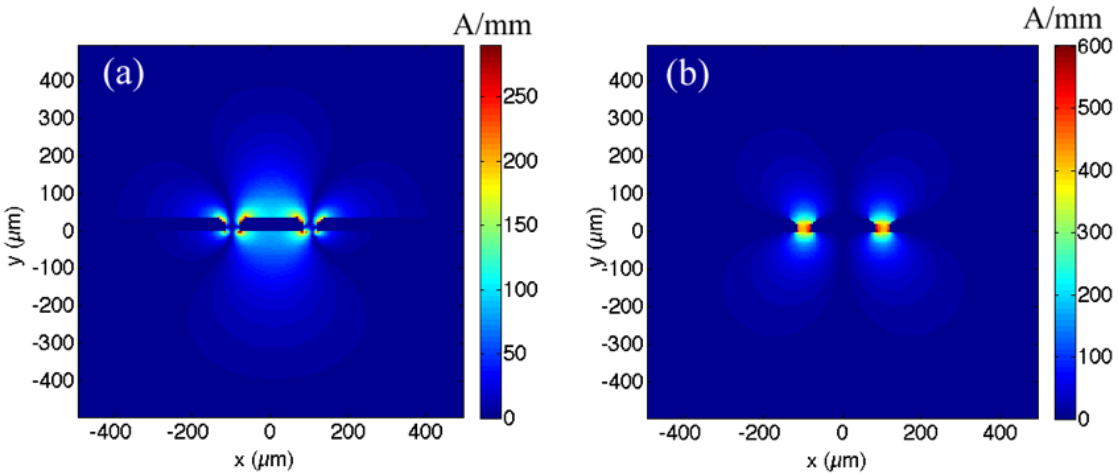

Figure 8.5: Transverse magnetic field distribution for RF transmission line structure, normalized to 1 W of power: (a) H_x. (b) H_y.

The co-planar transmission line design provides efficient application of the RF magnetic field parallel to the diamond surface (normal to the appropriate NV-axis). Field simulations were performed using in-house software (c code). The transmission line in this work was simulated to have an impedance of approximately 38 Ω, and a loss of approximately 31 dB/m

at 2.87 GHz. Fig. 8.5 shows the transverse magnetic field profile normalized to 1 W of power traveling along the transmission line. The x-component is the relevant component for our work. The line was fabricated in gold on a soda-lime glass substrate, using optical lithography and electron-beam evaporation to define a metal pattern. A subsequent electroplating step was used to achieve the desired metal thickness of approximately 35 μm. The line was widened at either end to allow for soldering to SMA connectors, which in turn were connected to the output of the RF amplifier and a 50 Ω termination, respectively.

Chapter 9

RESULTS

9.1 Iron Pattern Detection

In order to provide initial characterization of our system's ability to detect nano-scale magnetic material, we patterned the surface of one of our diamond sensing chips with iron nano-structures. The sensing surface used for this work was implanted with an N^+ ion implantation dose of 1×10^{11} cm^{-2}. Patterns were defined using electron-beam lithography. Poly-methyl-methacrylate (PMMA) was used as a resist on top of a silicon oxide layer previously deposited using plasma-enhanced chemical vapor deposition (PECVD). The purpose of the oxide layer was to provide an undercut layer for clean lift-off of sputtered iron. After development of the exposed PMMA, and a 180 s buffered oxide etch (BOE), 100 nm of iron and 3 nm of gold were deposited using an ion-beam sputtering (IBS) system. IBS depostion was performed in Kannan Krishnan's lab by Zheng Li. Upon removal of the un-exposed PMMA and a short ultra-sonic bath, only metal deposited in the defined pattern remained. Fig. 9.1 shows a scanning electron microscope (SEM) image of a resulting pattern. The smallest circle in the pattern (far right of bottom row) was defined as a 50-nm spot in the electron beam pattern.

The patterned diamond was then used as the sensing chip in our magneto-optical microscope. All magneto-optical images for the patterned iron were obtained using the single-frequency imaging scheme described in Section 8.1. Images were then processed to highlight areas with the highest sensitivity: difference values associated with each pixel were mapped to a narrow Gaussian. Each pixel in the resulting image has an intensity value

$$I = e^{\frac{-(S-S_0)^2}{2\sigma^2}}, \tag{9.1}$$

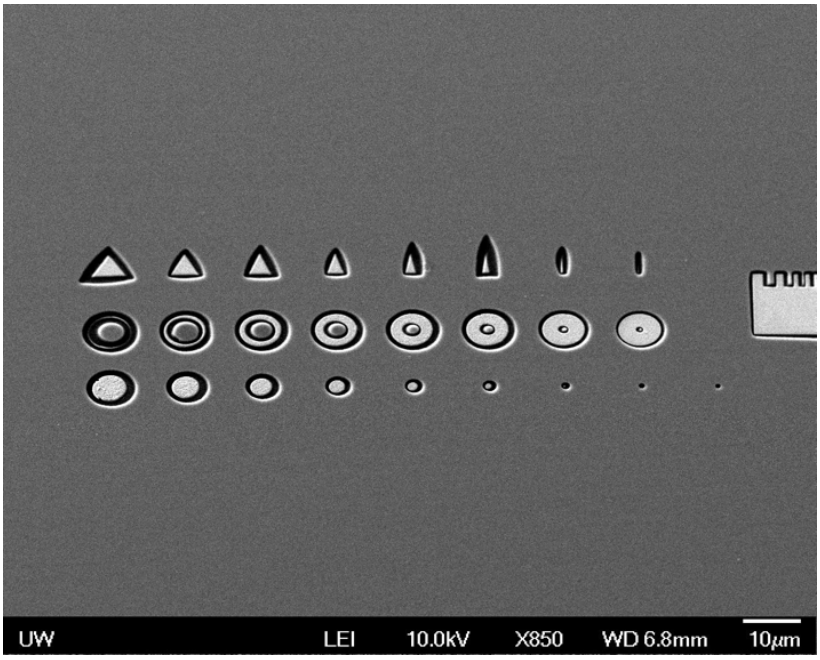

Figure 9.1: Scanning electron microscope (SEM) image of lithographically defined iron pattern on sensing chip surface. The unpatterned surface is a thin oxide layer, while the pattern is seen as iron (light) deposited in etched recessed in the oxide, so that it is sitting directly on the diamond surface (dark).

where S is the pixel's difference-image signal, S_0 is the difference-image signal corresponding to the steepest part of the sensor's ODMR curve, and σ is the spatial variation in difference-image signal under a uniform applied field.

We first looked at magneto-optical images of the field from a 2-μm diameter iron circle, shown in Fig. 9.2. The iron circle is located on the left of the field of view, as indicated by red dashed outlines. The images are taken at different frequencies, beginning with 2772 MHz in (a) and increasing by steps of 2 MHz (corresponding to magnetic field steps of 71 μT). It is clear that near the iron circle, the magnetic resonance is shifted to lower frequency with respect to the uniform applied field. This corresponds to a lower field outside the circle, as expected if the circle is considered to act similarly to a dipole aligned to the applied field. It can also be seen that the effect drops off smoothly with distance.

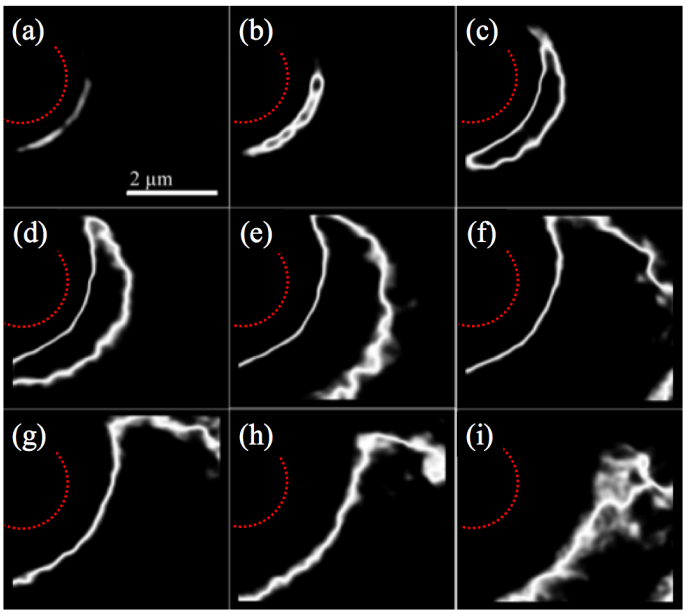

Figure 9.2: Magneto-optical images of field distribution from 2-μm diameter iron circle. Images were taken using single-frequency imaging, starting at 2772 MHz for (a) and increasing by steps of 2 MHz. Dashed red outlines indicate approximate location of iron material.

Next, we imaged a 50-nm diameter circle in the same manner. The resulting images are shown in Fig. 9.3. In this case, the iron circle is located at the spot seen in (a) and (b), and again we see that the field is lower in proximity to the circle and increases toward the background field with increasing distance. These images were taken with frequencies starting at 2782.25 MHz in (a) and increasing by steps of 0.25 MHz (corresponding to approximately 9 μT). Unambiguous detection of the 50-nm-diameter circle is demonstrated, indicating that nano-scale magnetic material can indeed be imaged in our system. This was the smallest defined feature in the fabricated magnetic pattern.

9.2 SPN Detection

The primary goal of this work was to demonstrate the system's ability to detect SPNs, as these are the proposed tags for biological applications. Toward this goal, magnetite SPNs

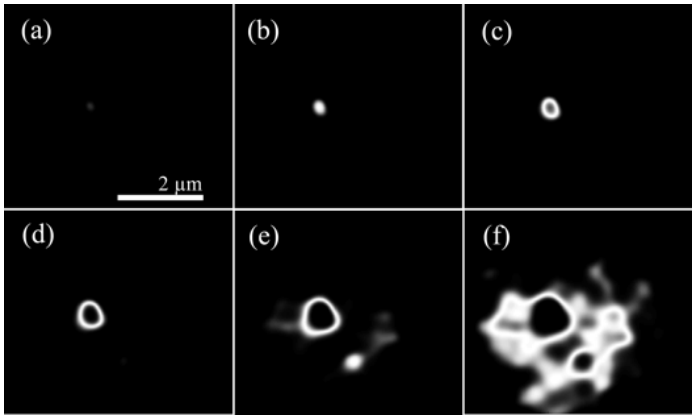

Figure 9.3: Magneto-optical image of fields from a 50-nm-diameter iron circle, starting with a frequency of 2782.25 MHz in (a) and increasing by steps of 0.25 MHz.

with a median core size of 16.9 ± 0.46 nm and a standard deviation of the log-normal distribution of 0.249 ± 0.036 were deposited on a sensing surface as isolated single particles and small groups. In this case, the sensing surface had an implantation dose of 1×10^{12} cm^{-2}. PL from this surface was approximately 4 times as bright as for the surface used in Section 9.1, and showed similar ODMR characteristics.

The SPNs were synthesized by Kannan Krishnan's group [93–95] and exhibited magnetic saturation for applied fields greater than ∼50 mT. Particle distributions were obtained by drying colloidal suspensions on lithographically defined patterns on the sensor surface, resulting in grid patterns with groups of particles at each grid point. A strong DC magnetic field on the order of 100 mT was applied during the particle deposition in order to align each particle's preferred magnetic axis normal to the chip surface [86]. Fig. 9.4(a) shows an SEM image of a group of approximately 65 particles.

Figs. 9.4(b-e) show magneto-optical images of the group for several RF frequencies (2835, 2839, 2844, and 2851 MHz, respectively). Each image was obtained using single-frequency imaging. In contrast to the magneto-optical images shown in Section 9.1, no Gaussian mapping has been applied to the difference values: these are simple difference images. Note

that a small ring is visible around the group of particles in which the magnetic resonance is shifted to lower frequencies, similar to the effect from the patterned iron structures presented in Section 9.1.

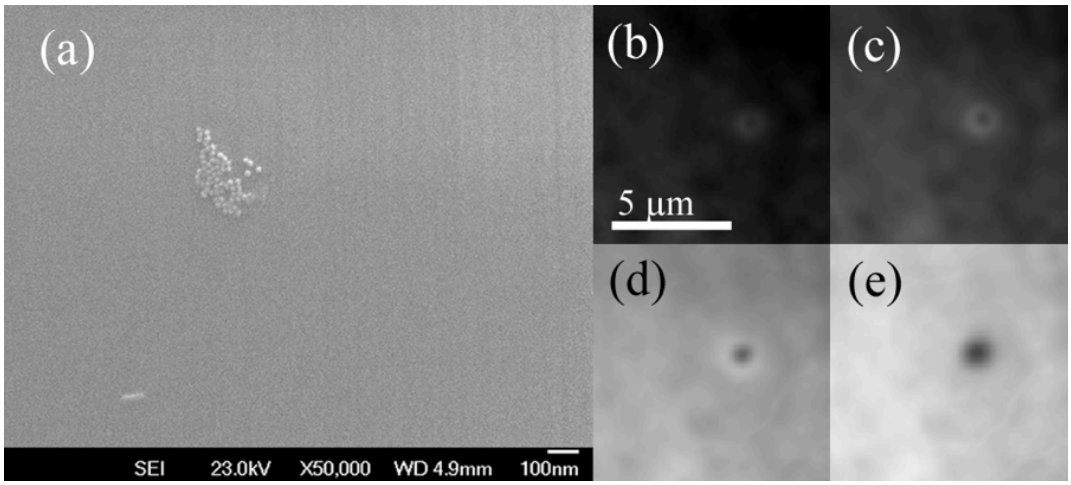

Figure 9.4: (a) SEM image of group of ∼65 SPNs. Single-frequency magneto-optical image of same group at (b) 2835 MHz, (c) 2839 MHz, (d) 2844 MHz and (e) 2851 MHz.

Fig. 9.5(a) shows an SEM image of a tight grid pattern, with smaller particle groups at each grid point. Fig. 9.5(b) shows a magneto-optical image of the SEM area. In this case, images are the result of the two-frequency imaging scheme described in Section 8.1. The total exposure time for each RF field state was 10 s, with no improvement in the signal-to-noise ratio (SNR, discussed in Section 9.3) observed for increased integration time. Single particles, indicated by black arrows, are visible as dark spots in the image. The upper left grid spot, indicated with a white arrow, contains no SPNs and there is correspondingly no detected signal. As expected, no particles or groups are visible in a PL image of the area, shown in Fig. 9.5(c).

Zoomed-in SEM images of both single-particle grid spots, as well as the empty grid spot, are shown in Figs. 9.5(d-f). Two grid spots containing two particles are also shown in Figs. 9.5(g-h). Horizontal line cuts through the particles show diameters close to 19 nm,

indicating their single-particle nature. A horizontal line cut through the center of the image is also included in Fig. 9.5(f) for comparison.

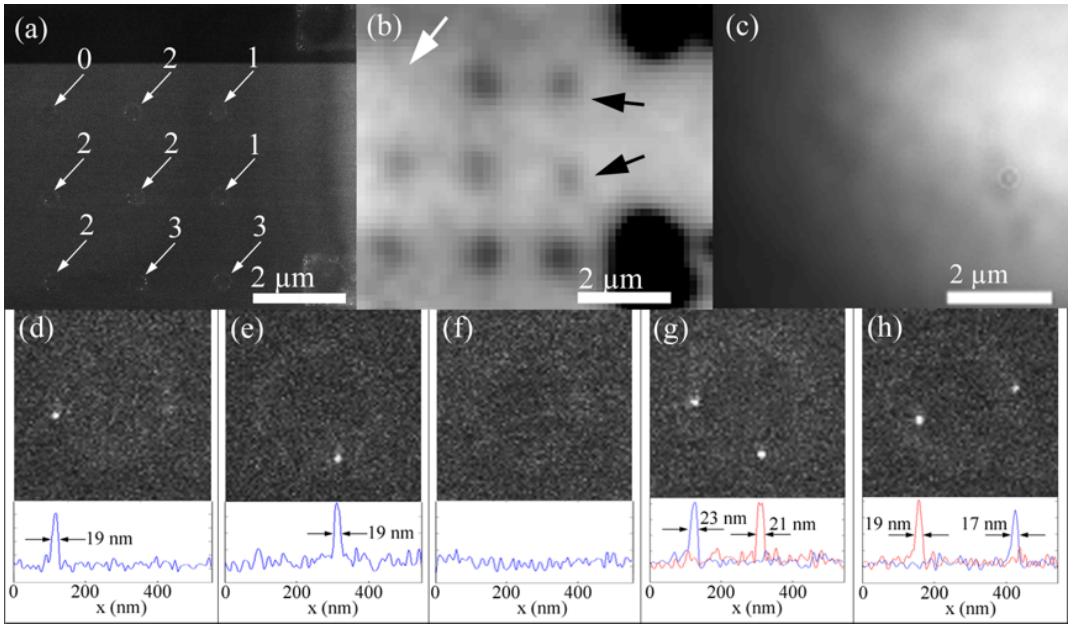

Figure 9.5: (a) SEM image of small groups of SPNs arranged in a tight grid pattern, with particle number noted for each group. (b) A magneto-optical image of SEM area. (c) PL image of imaging area. (d) SEM image of single particle in upper-right grid spot in (a), with horizontal cut data taken through the particle. (e) SEM image of single particle in center-right grid spot in (a), with horizontal cut data taken through the particle. (f) SEM image of empty grid spot (upper-left) in (a), with horizontal cut data taken through center of image. (g) SEM image of upper-middle grid spot in (a) containing two particles, with horizontal cut data taken through both particles. (h) SEM image of center-left grid spot in (a) containing two particles, with horizontal cut data taken through both particles.

The SEM images in Fig. 9.5 suggest a median particle diameter closer to 19 nm, slightly larger than the 16.9 nm obtained by Chantrell fitting [96] of vibrating-sample magnetometer (VSM) measurements. Analysis of a TEM image with a sample size of 56 particles yielded a similar result, showing a median diameter of 18.5 nm. We note that it is common for the 'magnetic-core size' of SPNs (measured by VSM) to be slightly smaller than the geometric size. This is typically attributed to surface effects [95, 96].

Including a second nearby imaging area with a similar grid pattern, a total of 18 grid spots containing between 0 and 5 particles were imaged. The detection of single particles and small groups is summarized in Fig. 9.6, where the signal-to-noise ratio for each group is plotted as a function of particle count. Importantly, all groups and single particles were detected with SNR values greater than 1.5, indicating that only a single particle is required within the field of view of the microscope for positive detection. For many applications, such as those requiring imaging of isolated single SPN-tagged biomolecules, this is an important capability. We note, however, that due to variations in signal between different groups of the same size, the system cannot currently be used for exact particle counting. The data suggests that particle number can at best be estimated to within ± 1 particle for group sizes of $n < 5$. The dominant source of variation in signal strength for a given group size is likely variation in particle size. In fact, the measured particle size variation corresponds to a variation in magnetic moment between a factor of 3.8 and 6.5 for individual particles. Neither a variation in the preferred-axis orientation of the SPNs, nor a variation in NV-particle distance is expected to be contributing significantly to the signal variation.

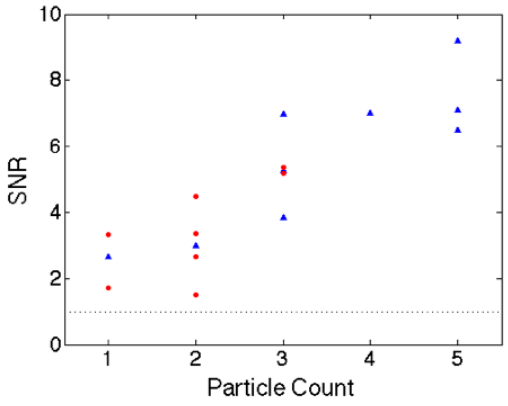

Figure 9.6: Plot of SNR as a function of particle count for all 17 non-zero groups in both tight-grid imaging areas. Red circles correspond to groups in the first imaging area (Fig. 9.5), while blue triangles represent groups in the second area. Dashed line is noise floor (SNR = 1).

9.3 Noise Considerations

In considering specific numbers for noise and sensitivity limits in our system, we will focus on the SPN detection result shown in Fig. 9.5. The definitions and concepts should apply to all other imaging results obtained on our system, as well as any other magneto-optical imaging making use of either of the two imaging schemes outlined in Section 8.1, provided that detector noise is not a limiting factor.

We begin by defining two types of pixel in our system. Camera pixels in our system correspond to 35-nm × 35-nm square areas on the diamond chip. However, image pixels are obtained by applying a weighted average centered at each camera pixel, using a two-dimensional Gaussian weight function with the same width as the optical resolution of the system (500 nm). This results in improved per-pixel noise without loss of optical resolution. For the remainder of this chapter "pixel" will refer to the image pixel resulting from this averaging, unless otherwise specified.

We define the magnetic-field limit of detection (LOD) as the magnetic field required to cause a change in pixel value equivalent to the 3-σ noise measured in a control area. The control area is chosen to be a 7-pixel × 7-pixel square near the particles under investigation. SNR values are also defined using the 3-σ noise, and the signal for a given group of particles is defined as the difference between the background average pixel value and the local pixel minimum associated with the group. This effectively measures the depth of the associated 2-dimensional dip in the image.

For the result shown in Fig. 9.5, we find that the standard deviation in pixel value is $\sigma = 0.0134\%$ (pixel values are reported as % difference between 'f_1' and 'f_2' images). The slope of the ODMR curve at the bias point is 0.3%/MHz. The field LOD corresponding to the 3-σ noise can be obtained as:

$$B_{LOD} = \frac{3\sigma h}{2mg\mu_B}, \tag{9.2}$$

where m is the slope of the ODMR curve, h is Planck's constant, σ is the standard deviation in pixel value, g is the electron g-factor and μ_B is the Bohr magneton. Plugging in the values

given above yields a magnetic field LOD of $B_{LOD} = 2.4\ \mu$T, in relatively good agreement with the expected value.

Calculation of the expected LOD is performed assuming optical shot-noise as the limiting factor in the system. In our PL images, the photon count rate for a 4 × 4 bin of camera pixels (146 nm × 146 nm) was $\sim 6.5 \times 10^5$ s^{-1}. For an optical resolution of 500 nm, this corresponds to $\sim 8.6 \times 10^6$ s^{-1} and thus a 1-σ shot noise of $\sim 2.94 \times 10^3$ s$^{-1/2}$, or $\sim 0.034\%/\sqrt{\text{Hz}}$ in a resolution-limited spot. Due to the image smoothing described above, we expect to achieve this same 1-σ shot noise percentage of $\sim 0.034\%/\sqrt{\text{Hz}}$ for each image pixel. Because our two-frequency imaging work is actually based on single-frequency imaging data, two-frequency images are composed of four separate exposures (f_1, f_2 and two images with RF-off). We expect photon shot noise in each of the four images to be uncorrelated, so the single-exposure noise should be multiplied by 2 to obtain the noise in a two-frequency image. This gives a per-pixel photon shot noise of $0.068\%/\sqrt{\text{Hz}}$. Plugging the photon shot noise into Eq. 9.2 as σ yields the magnetic field sensitivity. In this case we have a field sensitivity of S = 12.2 $\mu\text{T}/\sqrt{\text{Hz}}$. For an integration time of 10 s, this corresponds to an expected LOD of 3.8 μT.

We note that the use of four images is an artifact of our initial use of a single-frequency detection scheme during data collection and not inherent to the two-frequency scheme. Only the images with RF applied are required, and in fact we expect that an improvement in sensitivity by a factor of $\sqrt{2}$ should be obtained if only these images are used.

Similar analysis can be performed for single-frequency imaging, with one major difference: the formula for B_{LOD} (and S) will not have a factor of 2 in the denominator. From this, one advantage of two-frequency imaging over single-frequency imaging becomes clear: for the same per-pixel noise, we gain a factor of 2 in LOD (and sensitivity). A second important advantage of the two-frequency scheme is that it mitigates the effect of spatial fluctuations in ODMR characteristics that are symmetric about the resonance, such as variations in the depth and width of the ODMR curve.

Chapter 10

OUTLOOK

In summary, we have demonstrated room-temperature detection of single 19-nm magnetite SPNs (∼17-nm magnetic-core size) using wide-field optical microscopy. The significant advantage of this system over others capable of single-SPN detection is its relative simplicity; detection does not require cryogenic temperatures or nano-mechanical components, leaving it open to integration with biological and other nano-scale surface-based experiments. This marks a significant step forward in the detection of SPNs, and we expect that it will open the door to the development of biological tools capable of detecting single molecules. In fact, the project is currently focused on using the magneto-optical microscope to track DNA looping using larger magnetic beads as tags, of which single beads are easily detected in our system with integration times of only a few milliseconds. We also expect to develop SPN-tagged bio-assays capable of detecting a single molecular binding event using the current system.

Furthermore, improvements in sensitivity and LOD are possible. While two-frequency imaging mitigates the effect of spatial fluctuations in ODMR characteristics that are symmetric about the resonance, the system remains susceptible to variations that are anti-symmetric about the resonance. For example, strain variation within the chip may cause local shifts in the frequency of the spin transitions [6, 7, 97]. We expect to be able to mitigate this effect and further improve the LOD of the system by carefully measuring the ODMR spectrum of each pixel in the imaging area prior to any sensing experiments, allowing for subsequent computational image correction. Other possible sources of spatial noise are systematic spatial and thermal shifts between RF states, which could be reduced by mechanical and thermal isolation of RF components from the rest of the system. Additional paths to improved detection include using samples with longer spin-dephasing times [98], improved PL collec-

tion efficiency, NV layer thickness tailored to the strength of the magnetic dipoles under investigation, as well as increased optical and RF excitation fields.

Perhaps the lowest-hanging fruit is simply to increase the intensity of the NV-center PL by increasing the optical excitation power. While there is a limit to this set by the finite decay rate of the NV centers, we expect that at least an order of magnitude brighter PL can be obtained from the samples used in this work. For the magneto-optical imaging results presented in this document, we were limited by the maximum power of our laser. However, in order to maintain the depth of the ODMR curve with increased optical power, the RF field at the NV centers must also be increased. Toward this end we designed RF cavities, the details of which can be found in Appendix D.

A second way to increase the magnetic sensitivity of our system is to make use of a nanostructured diamond surface to increase PL collection efficiency. Similar work has been done to improve collection from single NVs in diamond [99]. The fundamental idea is to etch nano-scale pillars into the top surface of the diamond, which act as optical waveguides with propagation constants normal to the chip surface. This both inhibits emission into free-space modes and increases the effective collection angle of the microscope objective, resulting in significantly improved PL collection efficiency (>45% should be possible). The light can then be collected using a microscope system similar to the one used in this work. Initial testing of this idea would consist of simple PL intensity measurements, with subsequent magnetic detection experiments similar to those described in Chapter 9.

BIBLIOGRAPHY

[1] C. Schreyvogel, V. Polyakov, R. Wunderlich, J. Meijer, and C. E. Nebel, "Active charge state control of single NV centres in diamond by in-plane Al-Schottky junctions.," *Scientific reports*, vol. 5, p. 12160, jul 2015.

[2] J. R. Weber, W. F. Koehl, J. B. Varley, A. Janotti, B. B. Buckley, C. G. Van de Walle, and D. D. Awschalom, "Quantum computing with defects," *Proceedings of the National Academy of Sciences*, vol. 107, pp. 8513–8518, may 2010.

[3] L. Rondin, G. Dantelle, A. Slablab, F. Grosshans, F. Treussart, P. Bergonzo, S. Perruchas, T. Gacoin, M. Chaigneau, H.-C. Chang, V. Jacques, and J.-F. Roch, "Surface-induced charge state conversion of nitrogen-vacancy defects in nanodiamonds," *Physical Review B*, vol. 82, p. 115449, sep 2010.

[4] M. V. Hauf, B. Grotz, B. Naydenov, M. Dankerl, S. Pezzagna, J. Meijer, F. Jelezko, J. Wrachtrup, M. Stutzmann, F. Reinhard, and J. A. Garrido, "Chemical control of the charge state of nitrogen-vacancy centers in diamond," *Physical Review B*, vol. 83, p. 081304, feb 2011.

[5] B. Grotz, M. V. Hauf, M. Dankerl, B. Naydenov, S. Pezzagna, J. Meijer, F. Jelezko, J. Wrachtrup, M. Stutzmann, F. Reinhard, and J. A. Garrido, "Charge state manipulation of qubits in diamond," *Nature Communications*, vol. 3, p. 729, mar 2012.

[6] A. Lenef and S. Rand, "Electronic structure of the N-V center in diamond: Theory," *Physical Review B*, vol. 53, no. 20, 1996.

[7] N. Manson, J. Harrison, and M. Sellars, "Nitrogen-vacancy center in diamond: Model of the electronic structure and associated dynamics," *Physical Review B*, vol. 74, p. 104303, sep 2006.

[8] J. R. Maze, A. Gali, E. Togan, Y. Chu, A. Trifonov, E. Kaxiras, and M. D. Lukin, "Properties of nitrogen-vacancy centers in diamond: the group theoretic approach New Journal of Physics Properties of nitrogen-vacancy centers in diamond: the group theoretic approach," *New J. Phys. New Journal of Physics New Journal of Physics*, vol. 13, no. 13, pp. 25025–25025, 2011.

[9] M. W. Doherty, N. B. Manson, P. Delaney, and L. C. L. Hollenberg, "The negatively charged nitrogen-vacancy centre in diamond: the electronic solution," *New Journal of Physics*, vol. 13, p. 025019, feb 2011.

[10] V. Acosta, A. Jarmola, E. Bauch, and D. Budker, "Optical properties of the nitrogen-vacancy singlet levels in diamond," *Physical Review B*, vol. 82, p. 201202, nov 2010.

[11] L. Robledo, L. Childress, H. Bernien, B. Hensen, P. F. A. Alkemade, and R. Hanson, "High-fidelity projective read-out of a solid-state spin quantum register.," *Nature*, vol. 477, pp. 574–8, sep 2011.

[12] G. Balasubramanian, P. Neumann, D. Twitchen, M. Markham, R. Kolesov, N. Mizuochi, J. Isoya, J. Achard, J. Beck, J. Tissler, V. Jacques, P. R. Hemmer, F. Jelezko, and J. Wrachtrup, "Ultralong spin coherence time in isotopically engineered diamond.," *Nature materials*, vol. 8, pp. 383–7, may 2009.

[13] N. Bar-Gill, L. M. Pham, a. Jarmola, D. Budker, and R. L. Walsworth, "Solid-state electronic spin coherence time approaching one second.," *Nature communications*, vol. 4, p. 1743, jan 2013.

[14] M. V. Gurudev Dutt, L. Childress, L. Jiang, E. Togan, J. Maze, F. Jelezko, A. S. Zibrov, P. R. Hemmer, and M. D. Lukin, "Quantum register based on individual electronic and nuclear spin qubits in diamond," *Science*, vol. 316, no. 5829, pp. 1312–1316, 2007.

[15] G. Waldherr, Y. Wang, S. Zaiser, M. Jamali, T. Schulte-Herbuggen, H. Abe, T. Ohshima, J. Isoya, J. Du, P. Neumann, and J. Wrachtrup, "Quantum error correction in a solid-state hybrid spin register," *Nature*, vol. 506, pp. 204–207, 2014.

[16] M. S. Blok, N. Kalb, A. Reiserer, T. H. Taminiau, and R. Hanson, "Towards quantum networks of single spins: analysis of a quantum memory with an optical interface in diamond," *Faraday Discuss.*, vol. 184, pp. 173–182, 2015.

[17] R. Raussendorf and H. J. Briegel, "A one-way quantum computer," *Phys. Rev. Lett.*, vol. 86, p. 5188, 2001.

[18] S. D. Barrett and P. Kok, "Efficient high-fidelity quantum computation using matter qubits and linear optics," *Physical Review A*, vol. 71, p. 060310, jun 2005.

[19] Y. Li and S. C. Benjamin, "High threshold distributed quantum computing with three-qubit nodes," *New Journal of Physics*, vol. 14, p. 093008, sep 2012.

[20] S. Benjamin, B. Lovett, and J. Smith, "Prospects for measurement-based quantum computing with solid state spins," *Laser & Photonics Review*, vol. 3, pp. 556–574, nov 2009.

[21] S. C. Benjamin, D. E. Browne, J. Fitzsimons, and J. J. L. Morton, "Brokered graph-state quantum computation," *New Journal of Physics*, vol. 8, pp. 141–141, aug 2006.

[22] P. C. Maurer, G. Kucsko, C. Latta, L. Jiang, N. Y. Yao, S. D. Bennett, F. Pastawski, D. Hunger, N. Chisholm, M. Markham, D. J. Twitchen, J. I. Cirac, and M. D. Lukin, "Room-temperature quantum bit memory exceeding one second.," *Science (New York, N.Y.)*, vol. 336, pp. 1283–6, jun 2012.

[23] F. Dolde, I. Jakobi, B. Naydenov, N. Zhao, S. Pezzagna, C. Trautmann, J. Meijer, P. Neumann, F. Jelezko, and J. Wrachtrup, "Room-temperature entanglement between single defect spins in diamond," *Nature Physics*, vol. 9, pp. 139–143, feb 2013.

[24] T. van der Sar, Z. H. Wang, M. S. Blok, H. Bernien, T. H. Taminiau, D. M. Toyli, D. A. Lidar, D. D. Awschalom, R. Hanson, and V. V. Dobrovitski, "Decoherence-protected quantum gates for a hybrid solid-state spin register," *Nature*, vol. 484, pp. 82–86, apr 2012.

[25] A. Reiserer, N. Kalb, M. S. Blok, K. J. M. M. Van Bemmelen, T. H. Taminiau, R. Hanson, D. J. Twitchen, and M. Markham, "Robust Quantum-Network Memory Using Decoherence-Protected Subspaces of Nuclear Spins," *Physical Review X*, vol. 6, p. 021040, jun 2016.

[26] C. Cabrillo, J. I. Cirac, P. García-Fernández, and P. Zoller, "Creation of entangled states of distant atoms by interference," *Physical Review A*, vol. 59, p. 1025, 1999.

[27] H. Bernien, B. Hensen, W. Pfaff, G. Koolstra, M. S. Blok, L. Robledo, T. H. Taminiau, M. Markham, D. J. Twitchen, L. Childress, and R. Hanson, "Heralded entanglement between solid-state qubits separated by three metres.," *Nature*, vol. 497, pp. 86–90, may 2013.

[28] W. Pfaff, B. Hensen, H. Bernien, S. B. van Dam, M. S. Blok, T. H. Taminiau, M. J. Tiggelman, R. N. Schouten, M. Markham, D. J. Twitchen, and R. Hanson, "Unconditional quantum teleportation between distant solid-state quantum bits," *Science*, vol. 345, pp. 532–535, may 2014.

[29] B. Hensen, H. Bernien, A. E. Dreau, A. Reiserer, N. Kalb, M. S. Blok, J. Ruitenberg, R. F. L. Vermeulen, R. N. Schouten, C. Abellan, W. Amaya, V. Pruneri, M. W. Mitchell, M. Markham, D. J. Twitchen, D. Elkouss, S. Wehner, T. H. Taminiau, and

R. Hanson, "Loophole-free Bell inequality violation using electron spins separated by 1.3 kilometres," *Nature*, vol. 526, pp. 682–686, oct 2015.

[30] S. D. Barrett, P. Kok, K. Nemoto, R. G. Beausoleil, W. J. Munro, and T. P. Spiller, "A symmetry analyser for non-destructive bell state detection using weak nonlinearities," vol. 71, p. 60302, 2005.

[31] P. E. Barclay, K.-M. C. Fu, C. Santori, A. Faraon, and R. G. Beausoleil, "Hybrid Nanocavity Resonant Enhancement of Color Center Emission in Diamond," *Physical Review X*, vol. 1, p. 011007, sep 2011.

[32] G. Davies, "Vibronic spectra in diamond," *J. Phys. C: Solid State Phys.*, vol. 7, no. 20, pp. 3797–3809, 1974.

[33] P. Siyushev, V. Jacques, I. Aharonovich, F. Kaiser, T. Müller, L. Lombez, M. Atatüre, S. Castelletto, S. Prawer, F. Jelezko, and J. Wrachtrup, "Low-temperature optical characterization of a near-infrared single-photon emitter in nanodiamonds," *New Journal of Physics*, vol. 11, p. 113029, 2009.

[34] M. Gould, E. R. Schmidgall, S. Dadgostar, F. Hatami, and K.-M. C. Fu, "Efficient Extraction of Zero-Phonon-Line Photons from Single Nitrogen-Vacancy Centers in an Integrated GaP-on-Diamond Platform," *Physical Review Applied*, vol. 6, p. 011001, jul 2016.

[35] J. P. Hadden, J. P. Harrison, A. C. Stanley-Clarke, L. Marseglia, Y.-L. D. Ho, B. R. Patton, J. L. O'Brien, and J. G. Rarity, "Strongly enhanced photon collection from diamond defect centers under microfabricated integrated solid immersion lenses," *Applied Physics Letters*, vol. 97, p. 241901, dec 2010.

[36] M. Gould, S. Chakravarthi, I. R. Christen, N. Thomas, S. Dadgostar, Y. Song, M. L. Lee, F. Hatami, and K.-M. C. Fu, "Large-scale GaP-on-diamond integrated photonics platform for NV center-based quantum information," *Journal of the Optical Society of America B*, vol. 33, p. B35, jan 2016.

[37] M. Lončar and A. Faraon, "Quantum photonic networks in diamond," *MRS Bulletin*, vol. 38, pp. 144–148, feb 2013.

[38] M. Burek, Y. Chu, M. Liddy, P. Patel, J. Rochman, S. Meesala, W. Hong, W. Quan, M. Lukin, and M. Locar, "High quality-factor optical nanocavities in bulk single-crystal diamond," *Nature Communications*, vol. 5, p. 5718, 2014.

[39] B. Khanaliloo, M. Mitchell, A. C. Hryciw, and P. E. Barclay, "High-q/v monolithic diamond microdisks fabricated with quasi-isotropic etching," *Nano Letters*, vol. 15, no. 8, pp. 5131–5136, 2015.

[40] A. Faraon, C. Santori, Z. Huang, K. M. C. Fu, V. M. Acosta, D. Fattal, and R. G. Beausoleil, "Quantum photonic devices in single-crystal diamond," *New Journal of Physics*, vol. 15, 2013.

[41] B. J. M. Hausmann, B. Shields, Q. Quan, P. Maletinsky, M. McCutcheon, J. T. Choy, T. M. Babinec, A. Kubanek, A. Yacoby, M. D. Lukin, and M. Loncar, "Integrated diamond networks for quantum nanophotonics," *Nano Letters*, vol. 12, no. 3, pp. 1578–1582, 2012.

[42] D. F. Nelson, "Electro-optic and Piezoelectric Coefficients and Refractive Index of Gallium Phosphide," *Journal of Applied Physics*, vol. 39, p. 3337, nov 1968.

[43] J. P. Sprengers, A. Gaggero, D. Sahin, S. Jahanmirinejad, G. Frucci, F. Mattioli, R. Leoni, J. Beetz, M. Lermer, M. Kamp, S. Höfling, R. Sanjines, and A. Fiore, "Waveguide superconducting single-photon detectors for integrated quantum photonic circuits," *Applied Physics Letters*, vol. 99, p. 181110, nov 2011.

[44] M. K. Akhlaghi, E. Schelew, and J. F. Young, "Waveguide integrated superconducting single-photon detectors implemented as near-perfect absorbers of coherent radiation.," *Nature communications*, vol. 6, p. 8233, jan 2015.

[45] W. H. P. Pernice, C. Schuck, O. Minaeva, M. Li, G. N. Goltsman, A. V. Sergienko, and H. X. Tang, "High-speed and high-efficiency travelling wave single-photon detectors embedded in nanophotonic circuits.," *Nature communications*, vol. 3, p. 1325, jan 2012.

[46] N. Thomas, R. J. Barbour, Y. Song, M. L. Lee, and K.-M. C. Fu, "Waveguide-integrated single-crystalline GaP resonators on diamond.," *Optics express*, vol. 22, pp. 13555–64, jun 2014.

[47] N. Thomas, *Single-crystalline GaP waveguide-integrated resonators on diamond for future quantum information processing applications*. PhD thesis, University of Washington, 2014.

[48] K.-M. C. Fu, C. Santori, P. E. Barclay, and R. G. Beausoleil, "Conversion of neutral nitrogen-vacancy centers to negatively charged nitrogen-vacancy centers through selective oxidation," *Applied Physics Letters*, vol. 96, p. 121907, mar 2010.

[49] M. Volatier, D. Duchesne, R. Morandotti, R. Arès, and V. Aimez, "Extremely high aspect ratio GaAs and GaAs/AlGaAs nanowaveguides fabricated using chlorine ICP etching with N2-promoted passivation.," *Nanotechnology*, vol. 21, p. 134014, apr 2010.

[50] J. W. Lee, M. W. Devre, B. H. Reelfs, D. Johnson, J. N. Sasserath, F. Clayton, D. Hays, and S. J. Pearton, "Advanced selective dry etching of GaAs/AlGaAs in high density inductively coupled plasmas," *Journal of Vacuum Science & Technology A: Vacuum, Surfaces, and Films*, vol. 18, p. 1220, jul 2000.

[51] E. M. Purcell, "Spontaneous emission probabilities at radio frequencies," *Physical Review*, vol. 69, p. 681, 1946.

[52] E. D. Palik, *Handbook of Optical Constants of Solids*. Elsevier, 1998.

[53] L. Hope, "Theory of Optical Grating Couplers," *Optics Communications*, vol. 5, pp. 179–182, jun 1972.

[54] E. A. J. Marcatili, "Dielectric Rectangular Waveguide and Directional Coupler for Integrated Optics," *Bell System Technical Journal*, vol. 48, pp. 2071–2102, sep 1969.

[55] B. Jalali, S. Yegnanarayanan, and P. Trinh, "Integrated optical directional couplers in silicon-on-insulator," *Electronics Letters*, vol. 31, pp. 2097–2098, nov 1995.

[56] A. Faraon, C. Santori, Z. Huang, V. M. Acosta, and R. G. Beausoleil, "Coupling of Nitrogen-Vacancy Centers to Photonic Crystal Cavities in Monocrystalline Diamond," *Physical Review Letters*, vol. 109, p. 033604, jul 2012.

[57] C. Manolatou, M. Khan, S. Fan, P. Villeneuve, H. Haus, and J. Joannopoulos, "Coupling of modes analysis of resonant channel add-drop filters," *IEEE Journal of Quantum Electronics*, vol. 35, no. 9, pp. 1322–1331, 1999.

[58] C. Schuck, W. H. P. Pernice, and H. X. Tang, "Waveguide integrated low noise NbTiN nanowire single-photon detectors with milli-Hz dark count rate.," *Scientific reports*, vol. 3, p. 1893, jan 2013.

[59] F. Jelezko and J. Wrachtrup, "Single defect centres in diamond: A review," *physica status solidi (a)*, vol. 203, pp. 3207–3225, oct 2006.

[60] T. Oeckinghaus, R. Stöhr, R. Kolesov, J. Tisler, F. Reinhard, and J. Wrachtrup, "A compact, diode laser based excitation system for microscopy of nv centers," *Review of Scientific Instruments*, vol. 85, no. 7, 2014.

[61] A. Batalov, C. Zierl, T. Gaebel, P. Neumann, I.-Y. Chan, G. Balasubramanian, P. R. Hemmer, F. Jelezko, and J. Wrachtrup, "Temporal coherence of photons emitted by single nitrogen-vacancy defect centers in diamond using optical Rabi-oscillations.," *Physical review letters*, vol. 100, p. 077401, mar 2008.

[62] A. T. Collins, M. F. Thomaz, and M. I. B. Jorge, "Luminescence decay time of the 1.945 eV centre in type Ib diamond," *Journal of Physics C: Solid State Physics*, vol. 16, pp. 2177–2181, apr 1983.

[63] W. Lukosz and R. E. Kunz, "Light emission by magnetic and electric dipoles close to a plane interface I Total radiated power," *Journal of the Optical Society of America*, vol. 67, p. 1607, dec 1977.

[64] D. A. Turton, G. D. Reid, and G. S. Beddard, "Accurate Analysis of Fluorescence Decays from Single Molecules in Photon Counting Experiments," *Analytical Chemistry*, vol. 75, pp. 4182–4187, aug 2003.

[65] G. Liaugaudas, G. Davies, K. Suhling, R. U. A. Khan, and D. J. F. Evans, "Luminescence lifetimes of neutral nitrogen-vacancy centres in synthetic diamond containing nitrogen.," *Journal of physics. Condensed matter : an Institute of Physics journal*, vol. 24, p. 435503, oct 2012.

[66] L. Robledo, H. Bernien, T. van der Sar, and R. Hanson, "Spin dynamics in the optical cycle of single nitrogen-vacancy centres in diamond," *New Journal of Physics*, vol. 13, p. 025013, feb 2011.

[67] N. Aslam, G. Waldherr, P. Neumann, F. Jelezko, and J. Wrachtrup, "Photo-induced ionization dynamics of the nitrogen vacancy defect in diamond investigated by single-shot charge state detection," *New Journal of Physics*, vol. 15, p. 013064, jan 2013.

[68] A. Faraon, P. E. Barclay, C. Santori, K.-M. C. Fu, and R. G. Beausoleil, "Resonant enhancement of the zero-phonon emission from a colour centre in a diamond cavity," *Nat. Photonics*, vol. 5, p. 301, 2011.

[69] Y. Chu, N. P. de Leon, B. J. Shields, B. Hausmann, R. Evans, E. Togan, M. J. Burek, M. Markham, A. Stacey, A. S. Zibrov, A. Yacoby, D. J. Twitchen, M. Loncar, H. Park, P. Maletinsky, and M. D. Lukin, "Coherent optical transitions in implanted nitrogen vacancy centers.," *Nano letters*, vol. 14, pp. 1982–6, jan 2014.

[70] V. M. Acosta, C. Santori, A. Faraon, Z. Huang, K.-M. C. Fu, A. Stacey, D. A. Simpson, K. Ganesan, S. Tomljenovic-Hanic, A. D. Greentree, S. Prawer, and R. G. Beausoleil, "Dynamic Stabilization of the Optical Resonances of Single Nitrogen-Vacancy Centers in Diamond," *Physical Review Letters*, vol. 108, p. 206401, may 2012.

[71] L. C. Bassett, F. J. Heremans, C. G. Yale, B. B. Buckley, and D. D. Awschalom, "Electrical tuning of single nitrogen-vacancy center optical transitions enhanced by photoinduced fields," *Phys. Rev. Lett.*, vol. 107, p. 266403, Dec 2011.

[72] M. Mitchell, A. C. Hryciw, and P. E. Barclay, "Cavity optomechanics in gallium phosphide microdisks," *Applied Physics Letters*, vol. 104, p. 141104, apr 2014.

[73] H. A. Atikian, A. Eftekharian, A. Jafari Salim, M. J. Burek, J. T. Choy, A. Hamed Majedi, and M. Lončar, "Superconducting nanowire single photon detector on diamond," *Applied Physics Letters*, vol. 104, p. 122602, mar 2014.

[74] S. M. Sze, "Avalanche Breakdown Voltages of Abrupt and Linearly Graded p-n Junctions in Ge, Si, GaAs, and GaP," *Applied Physics Letters*, vol. 8, p. 111, nov 1966.

[75] R. Trew, J.-B. Yan, and P. Mock, "The potential of diamond and SiC electronic devices for microwave and millimeter-wave power applications," *Proceedings of the IEEE*, vol. 79, pp. 598–620, may 1991.

[76] N. Zhao, J. Honert, B. Schmid, and M. Klas, "Sensing single remote nuclear spins," *Nature nanotechnology*, vol. 7, no. September, pp. 657–662, 2012.

[77] P. Neumann, J. Beck, M. Steiner, F. Rempp, H. Fedder, P. R. Hemmer, J. Wrachtrup, and F. Jelezko, "Single-shot readout of a single nuclear spin.," *Science (New York, N.Y.)*, vol. 329, pp. 542–4, jul 2010.

[78] C. L. Degen, "Scanning magnetic field microscope with a diamond single-spin sensor," *Applied Physics Letters*, vol. 92, no. 24, p. 243111, 2008.

[79] S. Steinert, F. Dolde, P. Neumann, A. Aird, B. Naydenov, G. Balasubramanian, F. Jelezko, and J. Wrachtrup, "High sensitivity magnetic imaging using an array of spins in diamond.," *The Review of scientific instruments*, vol. 81, p. 043705, apr 2010.

[80] L. Pham and D. L. Sage, "Magnetic field imaging with nitrogen-vacancy ensembles," *New Journal of Physics*, vol. 13, p. 045021, apr 2011.

[81] B. J. Maertz, A. P. Wijnheijmer, G. D. Fuchs, M. E. Nowakowski, and D. D. Awschalom, "Vector magnetic field microscopy using nitrogen vacancy centers in diamond," *Applied Physics Letters*, vol. 96, no. 9, p. 092504, 2010.

[82] K. S. Kim and J.-K. Park, "Magnetic force-based multiplexed immunoassay using superparamagnetic nanoparticles in microfluidic channel.," *Lab on a chip*, vol. 5, pp. 657–64, jun 2005.

[83] C. Hoffmann, E. Mazari, S. Lallet, R. Le Borgne, V. Marchi, C. Gosse, and Z. Gueroui, "Spatiotemporal control of microtubule nucleation and assembly using magnetic nanoparticles.," *Nature nanotechnology*, vol. 8, pp. 199–205, mar 2013.

[84] G. Li, V. Joshi, R. L. White, S. X. Wang, J. T. Kemp, C. Webb, R. W. Davis, and S. Sun, "Detection of single micron-sized magnetic bead and magnetic nanoparticles using spin valve sensors for biological applications," *Journal of Applied Physics*, vol. 93, no. 10, p. 7557, 2003.

[85] R. S. Gaster, L. Xu, S.-J. Han, R. J. Wilson, D. a. Hall, S. J. Osterfeld, H. Yu, and S. X. Wang, "Quantification of protein interactions and solution transport using high-density GMR sensor arrays.," *Nature nanotechnology*, vol. 6, pp. 314–320, may 2011.

[86] T. Nocera, J. Chen, C. Murray, and G. Agarwal, "Magnetic anisotropy considerations in magnetic force microscopy studies of single superparamagnetic nanoparticles," *Nanotechnology*, vol. 23, p. 495704, dec 2012.

[87] C. Thirion, W. Wernsdorfer, and D. Mailly, "Switching of magnetization by nonlinear resonance studied in single nanoparticles," *Nature materials*, vol. 2, pp. 524–527, aug 2003.

[88] M. Gabureac, L. Bernau, G. Boero, and I. Utke, "Single superparamagnetic bead detection and direct tracing of bead position using novel nanocomposite Hall sensors," *IEEE Transactions on Nanotechnology*, vol. 12, no. 5, pp. 668–673, 2013.

[89] G. Mihajlovic and P. Xiong, "Detection of single magnetic bead for biological applications using an InAs quantum-well micro-Hall sensor," *Applied Physics Letters*, vol. 87, no. 11, p. 112502, 2005.

[90] W. Shen, X. Liu, D. Mazumdar, and G. Xiao, "In situ detection of single micron-sized magnetic beads using magnetic tunnel junction sensors," *Applied Physics Letters*, vol. 86, no. 25, p. 253901, 2005.

[91] M. Gould, R. J. Barbour, N. Thomas, H. Arami, K. M. Krishnan, and K.-M. C. Fu, "Room-temperature detection of a single 19nm super-paramagnetic nanoparticle with an imaging magnetometer," *Applied Physics Letters*, vol. 105, p. 072406, aug 2014.

[92] C. Santori, P. Barclay, K.-M. Fu, and R. Beausoleil, "Vertical distribution of nitrogen-vacancy centers in diamond formed by ion implantation and annealing," *Physical Review B*, vol. 79, p. 125313, mar 2009.

[93] H. Arami and R. Ferguson, "Size-dependent ferrohydrodynamic relaxometry of magnetic particle imaging tracers in different environments," *Medical Physics*, vol. 40, p. 071904, jul 2013.

[94] R. M. Ferguson, A. P. Khandhar, and K. M. Krishnan, "Tracer design for magnetic particle imaging (invited).," *Journal of applied physics*, vol. 111, pp. 7B318–7B3185, apr 2012.

[95] A. P. Khandhar, R. M. Ferguson, H. Arami, and K. M. Krishnan, "Monodisperse magnetite nanoparticle tracers for in vivo magnetic particle imaging.," *Biomaterials*, vol. 34, pp. 3837–45, may 2013.

[96] R. Chantrell, J. Popplewell, and S. Charles, "Measurements of particle size distribution parameters in ferrofluids," *IEEE Transactions on Magnetics*, vol. 14, pp. 975–977, sep 1978.

[97] P. Olivero, F. Bosia, B. a. Fairchild, B. C. Gibson, a. D. Greentree, P. Spizzirri, and S. Prawer, "Splitting of photoluminescent emission from nitrogen–vacancy centers in diamond induced by ion-damage-induced stress," *New Journal of Physics*, vol. 15, p. 043027, apr 2013.

[98] E. E. Kleinsasser, M. M. Stanfield, J. K. Q. Banks, Z. Zhu, W.-D. Li, V. M. Acosta, H. Watanabe, K. M. Itoh, and K.-M. C. Fu, "High density NV sensing surface created via He^(+) ion implantation of (12)^C diamond," p. 5, feb 2016.

[99] T. M. Babinec, B. J. M. Hausmann, M. Khan, Y. Zhang, J. R. Maze, P. R. Hemmer, and M. Loncar, "A diamond nanowire single-photon source.," *Nature nanotechnology*, vol. 5, pp. 195–9, mar 2010.

Appendix A

COUPLED DISK ANALYSIS

A.1 Infinitesimal Coupling Coefficients

In order to define the infinitesimal coupling coefficients between guided modes in two separate waveguides, I consider them first as orthogonal (completely decoupled, separated by an infinite distance), and then consider each waveguide as a perturbation to the guided mode of the other as they are brought together. I write out Maxwell's equations for the de-coupled modes as follows:

$$\hat{H}|\Psi\rangle = i\hat{A}\hat{\beta}|\Psi\rangle \tag{A.1}$$

Taking the standard basis as the de-coupled modes of each waveguide ψ_1 and ψ_2, we can write out the operators as:

$$\hat{H} = \begin{bmatrix} \hat{H}_1 & 0 \\ 0 & \hat{H}_2 \end{bmatrix} \tag{A.2}$$

$$\hat{A} = \hat{A}_0 \begin{bmatrix} 1 & \frac{\langle\psi_1|\hat{A}_0|\psi_2\rangle}{\langle\psi_2|\hat{A}_0|\psi_2\rangle} \\ \frac{\langle\psi_2|\hat{A}_0|\psi_1\rangle}{\langle\psi_1|\hat{A}_0|\psi_1\rangle} & 1 \end{bmatrix} \tag{A.3}$$

$$\hat{\beta} = \hat{I} \begin{bmatrix} \beta_1 & 0 \\ 0 & \beta_2 \end{bmatrix} \tag{A.4}$$

where β_n are the propagation constants for each mode, and the subspace operators $\hat{H}_n$ and $\hat{A}_0$ act on the electromagnetic fields of a single mode as:

$$\hat{H}_n|\psi\rangle = \begin{bmatrix} i\omega\epsilon_{xn}\epsilon_0 & 0 & 0 & 0 & 0 & \delta_y \\ 0 & i\omega\epsilon_{yn}\epsilon_0 & 0 & 0 & 0 & -\delta_x \\ 0 & 0 & i\omega\epsilon_{zn}\epsilon_0 & -\delta_y & \delta_x & 0 \\ 0 & 0 & -\delta_y & i\omega\mu_{xn}\mu_0 & 0 & 0 \\ 0 & 0 & \delta_x & 0 & i\omega\mu_{yn}\mu_0 & 0 \\ \delta_y & -\delta_x & 0 & 0 & 0 & i\omega\mu_{zn}\mu_0 \end{bmatrix} \begin{bmatrix} E_x \\ E_y \\ E_z \\ H_x \\ H_y \\ H_z \end{bmatrix} \tag{A.5}$$

$$\hat{A}_0|\psi\rangle = \begin{bmatrix} 0 & 0 & 0 & 0 & 1 & 0 \\ 0 & 0 & 0 & -1 & 0 & 0 \\ 0 & 0 & 0 & 0 & 0 & 0 \\ 0 & -1 & 0 & 0 & 0 & 0 \\ 1 & 0 & 0 & 0 & 0 & 0 \\ 0 & 0 & 0 & 0 & 0 & 0 \end{bmatrix} \begin{bmatrix} E_x \\ E_y \\ E_z \\ H_x \\ H_y \\ H_z \end{bmatrix} \tag{A.6}$$

where the permittivity and permeability distributions in $\hat{H}_n$ are for the waveguide supporting mode ψ_n. $\hat{I}$ is the single-mode identity. Note that both $\hat{H}$ and $\hat{\beta}$ are diagonal in the $\{\psi_1, \psi_2\}$ basis. Now we consider coupling as a small perturbation to $\hat{H}\Psi$, and allow for small changes to $\hat{\beta}$ and Ψ so that Maxwell's equations remain satisfied:

$$(\hat{H} + \Delta\hat{H})(\Psi + \Delta\Psi) = i\hat{A}(\hat{\beta} + \Delta\hat{\beta})(\Psi + \Delta\Psi) \tag{A.7}$$

Multiplying both sides of equation (7) by $\langle(\Psi + \Delta\Psi)$, and keeping only zero- and first-order terms we can obtain:

$$i\langle\Psi|\hat{A}\Delta\hat{\beta}|\Psi\rangle = \langle\Psi|\hat{H}|\Delta\Psi\rangle + \langle\Delta\Psi|\hat{H}|\Psi\rangle + \langle\Psi|\Delta\hat{H}|\Psi\rangle - i\langle\Psi|\hat{A}\hat{\beta}|\Delta\Psi\rangle - i\langle\Delta\Psi|\hat{A}\hat{\beta}|\Psi\rangle \tag{A.8}$$

Using equation (1), we can remove two terms:

$$i\langle\Psi|\hat{A}\Delta\hat{\beta}|\Psi\rangle = \langle\Psi|\hat{H}|\Delta\Psi\rangle + \langle\Psi|\Delta\hat{H}|\Psi\rangle - i\langle\Psi|\hat{A}\hat{\beta}|\Delta\Psi\rangle \tag{A.9}$$

Knowing that $\hat{H}$ is anti-hermitian, $\hat{A}$ is hermitian and $\hat{\beta}$ is diagonal, the two remaining $\Delta\Psi$ terms can be shown to cancel out, and we are left with:

$$i\langle\Psi|\hat{A}\Delta\hat{\beta}|\Psi\rangle = \langle\Psi|\Delta\hat{H}|\Psi\rangle \tag{A.10}$$

Noting that we did not put any restrictions on Ψ within the space spanned by ψ_1 and ψ_2, we have that:

$$\hat{A}\Delta\hat{\beta} = -i\Delta\hat{H} \tag{A.11}$$

So, writing out the operators in the 2-mode basis we can obtain:

$$\hat{A}_0\Delta\hat{\beta} = \frac{-i\langle\psi_1|\hat{A}_0|\psi_1\rangle\langle\psi_2|\hat{A}_0|\psi_2\rangle}{\langle\psi_1|\hat{A}_0|\psi_1\rangle\langle\psi_2|\hat{A}_0|\psi_2\rangle - \langle\psi_1|\hat{A}_0|\psi_2\rangle\langle\psi_2|\hat{A}_0|\psi_1\rangle} \begin{bmatrix} 1 & -\frac{\langle\psi_1|\hat{A}_0|\psi_2\rangle}{\langle\psi_2|\hat{A}_0|\psi_2\rangle} \\ -\frac{\langle\psi_2|\hat{A}_0|\psi_1\rangle}{\langle\psi_1|\hat{A}_0|\psi_1\rangle} & 1 \end{bmatrix} \begin{bmatrix} \Delta\hat{H}_1 & 0 \\ 0 & \Delta\hat{H}_2 \end{bmatrix} \tag{A.12}$$

Matrix multiplication leads to:

$$\hat{A}_0\Delta\hat{\beta} = \frac{-i\langle\psi_1|\hat{A}_0|\psi_1\rangle\langle\psi_2|\hat{A}_0|\psi_2\rangle}{\langle\psi_1|\hat{A}_0|\psi_1\rangle\langle\psi_2|\hat{A}_0|\psi_2\rangle - \langle\psi_1|\hat{A}_0|\psi_2\rangle\langle\psi_2|\hat{A}_0|\psi_1\rangle} \begin{bmatrix} \Delta\hat{H}_1 & -\Delta\hat{H}_2\frac{\langle\psi_1|\hat{A}_0|\psi_2\rangle}{\langle\psi_2|\hat{A}_0|\psi_2\rangle} \\ -\Delta\hat{H}_1\frac{\langle\psi_2|\hat{A}_0|\psi_1\rangle}{\langle\psi_1|\hat{A}_0|\psi_1\rangle} & \Delta\hat{H}_2 \end{bmatrix} \tag{A.13}$$

Letting $\Delta\hat{\beta}$ be proportional to the mode-subspace identity, we can solve for the individual elements of beta by left- and right-multiplying both sides of equation (13) by appropriate bra's and ket's. Furthermore, assume that the de-coupled modes ψ_n are $\hat{A}_0$-normalized (this is equivalent to power normalization):

$$\Delta\hat{\beta}_{mn} = \frac{-i\langle\psi_m|\Delta\hat{H}_n|\psi_n\rangle}{1 - \langle\psi_1|\hat{A}_0|\psi_2\rangle\langle\psi_2|\hat{A}_0|\psi_1\rangle}, m = n \tag{A.14}$$

$$\Delta\hat{\beta}_{mn} = \frac{i\langle\psi_m|\Delta\hat{H}_n|\psi_n\rangle}{1 - \langle\psi_1|\hat{A}_0|\psi_2\rangle\langle\psi_2|\hat{A}_0|\psi_1\rangle}, m \neq n \tag{A.15}$$

Now in the case of directional coupling between two separate waveguides, we define the perturbation to each mode as:

$$\Delta\hat{H}_n|\psi\rangle = \begin{bmatrix} i\omega\Delta\epsilon_{xn}\epsilon_0 & 0 & 0 & 0 & 0 & 0 \\ 0 & i\omega\Delta\epsilon_{yn}\epsilon_0 & 0 & 0 & 0 & 0 \\ 0 & 0 & i\omega\Delta\epsilon_{zn}\epsilon_0 & 0 & 0 & 0 \\ 0 & 0 & 0 & i\omega\Delta\mu_{xn}\mu_0 & 0 & 0 \\ 0 & 0 & 0 & 0 & i\omega\Delta\mu_{yn}\mu_0 & 0 \\ 0 & 0 & 0 & 0 & 0 & i\omega\Delta\mu_{zn}\mu_0 \end{bmatrix} \begin{bmatrix} E_x \\ E_y \\ E_z \\ H_x \\ H_y \\ H_z \end{bmatrix}$$
$$= i\omega \begin{bmatrix} \epsilon_0\Delta\hat{\epsilon_r} & 0 \\ 0 & \mu_0\Delta\hat{\mu_r} \end{bmatrix} \begin{bmatrix} \vec{E} \\ \vec{H} \end{bmatrix} \quad \text{(A.16)}$$

Noting that $\Delta\hat{H}_n$ is only non-zero in the region of the other waveguide core, it is clear that the diagonal elements of $\Delta\hat{\beta}$ will be small compared to the off-diagonals for well-confined, well-separated modes. We will thus ignore the change in diagonal elements for the remainder of this document and write the coupled propagation matrix as:

$$\hat{\beta}_c = \hat{I} \begin{bmatrix} \beta_1 & \kappa_{12} \\ \kappa_{21} & \beta_2 \end{bmatrix} \quad \text{(A.17)}$$

where

$$\kappa_{ij} = \frac{-\omega \left(\epsilon_0 \iint (\vec{E_i^*} \cdot \Delta\hat{\epsilon}_j \vec{E_j}) \mathrm{d}A + \mu_0 \iint (\vec{H_i^*} \cdot \Delta\hat{\mu}_j \vec{H_j}) \mathrm{d}A \right)}{1 - \left| \iint \left(E_{xi}^* H_{yj} - E_{yi}^* H_{xj} + H_{yi}^* E_{xj} - H_{xi}^* E_{yj} \right) \mathrm{d}A \right|^2} \quad \text{(A.18)}$$

A.2 Finite Coupling Coefficient

Beginning with the result from the previous section, we have that:

$$\frac{\mathrm{d}}{\mathrm{d}z}|\Psi\rangle = i \begin{bmatrix} \beta_1 & \kappa_{12} \\ \kappa_{21} & \beta_2 \end{bmatrix} \begin{bmatrix} c_1|\psi_1\rangle \\ c_2|\psi_2\rangle \end{bmatrix} \quad \text{(A.19)}$$

where β_i are the propagation constants of the modes of the de-coupled waveguides and κ_{ij} are the infinitesimal coupling constants derived in Section A.1. Solving the differential equation (19) yields:

$$\begin{bmatrix} c_1 \\ c_2 \end{bmatrix} = e^{i\frac{(\beta_1+\beta_2)}{2}z} \begin{bmatrix} iAsin\left(\sqrt{\left(\frac{\beta_1-\beta_2}{2}\right)^2+\kappa_{12}\kappa_{21}}z\right)+Bcos\left(\sqrt{\left(\frac{\beta_1-\beta_2}{2}\right)^2+\kappa_{12}\kappa_{21}}z\right) \\ iBsin\left(\sqrt{\left(\frac{\beta_1-\beta_2}{2}\right)^2+\kappa_{12}\kappa_{21}}z\right)+Acos\left(\sqrt{\left(\frac{\beta_1-\beta_2}{2}\right)^2+\kappa_{12}\kappa_{21}}z\right) \end{bmatrix} \tag{A.20}$$

In the limiting case of all power being initially in one mode (a close approximation of our cases of interest), we obtain the following solutions for power carried by each mode:

$$|c_1|^2 = \frac{1}{(\beta_1-\beta_2)^2+4\kappa_{12}\kappa_{21}}\left((\beta_1-\beta_2)^2+4\kappa_{12}\kappa_{21}cos^2\left(\sqrt{\left(\frac{\beta_1-\beta_2}{2}\right)^2+\kappa_{12}\kappa_{21}}z\right)\right) \tag{A.21}$$

$$|c_2|^2 = \frac{4|\kappa_{21}|^2}{(\beta_1-\beta_2)^2+4\kappa_{12}\kappa_{21}}sin^2\left(\sqrt{\left(\frac{\beta_1-\beta_2}{2}\right)^2+\kappa_{12}\kappa_{21}}z\right) \tag{A.22}$$

For very small total coupling (which is what we want for high-Q resonators), the arguments of the sinusoids are much smaller than one. To second order in the arguments of the sinusoids, we then have that:

$$|c_1|^2 = 1-\kappa_{12}\kappa_{21}L^2 \tag{A.23}$$

$$|c_2|^2 = \kappa_{21}^2L^2 \tag{A.24}$$

where L is the coupling length. Thus, what matters most to us for collection of NV- PL into resonator modes is the resonator out-coupling coefficient $\kappa_{21}L$ (remember we have assumed much more power in mode 1, and so mode 1 corresponds to the resonator mode). However, by power conservation there must be some coupling to other modes (possibly un-guided) for

$\kappa_{12} \leq \kappa_{21}$. This can be modeled as a decaying exponential (imaginary part of β_i). To second order, this has no effect on coupled power ($|c_2|^2$) in the weak coupling regime (equation (24)), but equation (23) is corrected to:

$$|c_1|^2 = 1 - \kappa_{12}\kappa_{21}L^2 - \kappa_{21}\Delta L^2 = 1 - \kappa_{21}^2 L^2 \tag{A.25}$$

where $\Delta = \kappa_{21} - \kappa_{12}$. In this case, power is conserved in the weak coupling regime. On the other hand, when $\kappa_{12} > \kappa_{21}$ and barring any gain in the system, the coupling must be lossy. And so a secondary consideration should be to ensure that $\kappa_{12} \leq \kappa_{21}$. This is the case for current devices. The remainder of this document will assume this is the case and that the coupling is lossless, and we define the finite coupling and transmission coefficients for circular resonators:

$$\kappa = \kappa_{21} L_{eff} \tag{A.26}$$

$$t = \sqrt{1 - \kappa_{21}^2 L_{eff}^2} \tag{A.27}$$

where L_{eff} is an effective coupling length that scales with the diameter of the resonator and again κ_{21} is the infinitesimal resonator-to-bus coupling coefficient.

A.3 Power Flow and Quality Factor

A.3.1 Transmission Spectrum

Here, we consider the power transmission spectrum of a general circular resonator coupled to a bus waveguide, as shown in Fig. A.1

Let us assume a lossless directional coupler with finite coupling coefficient κ:

$$\begin{bmatrix} a_2 \\ b_2 \end{bmatrix} = e^{i\phi} \begin{bmatrix} t & i\kappa \\ i\kappa & t \end{bmatrix} \begin{bmatrix} a_1 \\ b_1 \end{bmatrix} \tag{A.28}$$

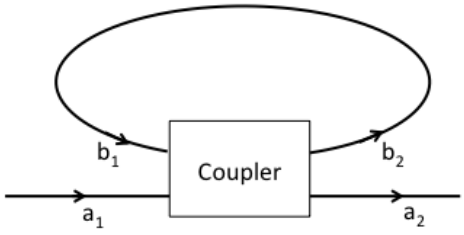

Figure A.1: Drawing of setup for transmission behavior of bus waveguide and circulating resonator with directional coupling.

where $t = \sqrt{1-\kappa^2}$ is the transmission coefficient of the directional coupler. Now letting b_2 be related to b_1 by some positive, real scaling factor $\gamma \leq 1$, and an acquired phase θ:

$$b_1 = \gamma e^{i\theta} b_2 \tag{A.29}$$

It is easy to show that $\gamma = \sqrt{1-\alpha}$ where α is the round-trip power loss. From equations (28) and (29), and setting $a_1 = 1$ for unity input power, we can obtain:

$$a_2 = e^{i\phi}\left(\frac{te^{-i(\theta+\phi)} - \gamma}{e^{-i(\theta+\phi)} - t\gamma}\right) \tag{A.30}$$

and thus an expression for the transmitted power:

$$T = |a_2|^2 = \frac{t^2 + \gamma^2 - 2t\gamma cos(\theta+\phi)}{1 + t^2\gamma^2 - 2t\gamma cos(\theta+\phi)} \tag{A.31}$$

On resonance ($\theta + \phi = 2m\pi$), we have:

$$T_{res} = |a_2|^2_{res} = \frac{(t-\gamma)^2}{(1-t\gamma)^2} \tag{A.32}$$

A.3.2 Quality Factor

In order to determine the quality factor, we will look at circulating power. The quality factor is then taken as the ratio of resonance center to FWHM of the power spectrum:

$$|b_2| = \frac{e^{i\phi}\kappa}{1 - t\gamma e^{i(\theta+\phi)}} \tag{A.33}$$

$$|b_2|^2 = \frac{\kappa^2}{1 + t^2\gamma^2 - 2t\gamma cos(\theta + \phi)} \tag{A.34}$$

On resonance, we have that:

$$|b_2|^2_{res} = \frac{\kappa^2}{(1 - t\gamma)^2} \tag{A.35}$$

From here, consolidating the total phase as $\Theta = \theta + \phi$ and setting circulating power to half the maximum:

$$2(1 - t\gamma)^2 = 1 + t^2\gamma^2 - 2t\gamma cos(\Theta) \tag{A.36}$$

Assuming $|\Phi| = |\Theta - 2m\pi| << 1$, we can expand $cos(\Phi)$ to second order as $1 - \Phi^2$ and solve for Θ:

$$\Theta = 2m\pi \pm \frac{1 - t\gamma}{\sqrt{t\gamma}} \tag{A.37}$$

Now we consider an angular effective index such that $\lambda = \frac{4\pi^2\tilde{n}_{eff}}{\Theta}$, as well as a first order gradient $\frac{d\tilde{n}_{eff}}{d\lambda}$. On resonance, we have that:

$$\lambda_0 = \frac{2\pi\tilde{n}_{eff}}{m} \tag{A.38}$$

And at the half-power points, we have:

$$\lambda_+ = \frac{4\pi^2\tilde{n}_+}{2m\pi - \left(\frac{1-t\gamma}{\sqrt{t\gamma}}\right)}; \lambda_- = \frac{4\pi^2\tilde{n}_-}{2m\pi + \left(\frac{1-t\gamma}{\sqrt{t\gamma}}\right)} \tag{A.39}$$

After a bunch of algebra, and assuming $\tilde{n}_+ + \tilde{n}_- = 2\tilde{n}_{eff}$, we can obtain an expression for the quality factor:

$$Q = \frac{\lambda_0}{\Delta\lambda} = \frac{\frac{16\pi^4 t\gamma \tilde{n}_{eff}\tilde{n}_g}{\lambda_0^2} - (1-t\gamma)^2}{\frac{8\pi^2\tilde{n}_{eff}}{\lambda_0}\sqrt{t\gamma}(1-t\gamma)} \tag{A.40}$$

where $\tilde{n}_g = \tilde{n}_{eff} - \lambda_0 \frac{d\tilde{n}_{eff}}{d\lambda}$ is the group angular index of the resonator, analogous to the group index of a straight waveguide. With the simplifying assumptions that $(1-t\gamma)^2 << \frac{16\pi^4 t\gamma\tilde{n}_{eff}\tilde{n}_g}{\lambda_0^2}$ and $\sqrt{t\gamma} \approx 1$:

$$Q = \frac{\tilde{n}_g m\pi}{\tilde{n}_{eff}(1-t\gamma)} \tag{A.41}$$

A.3.3 Out-Coupling

Let's now consider a similar setup, but with an emitter in the resonator path

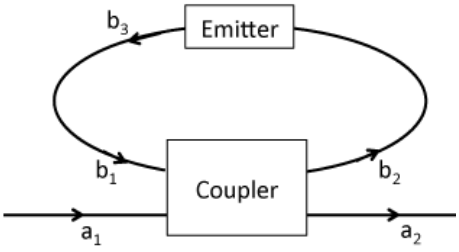

Figure A.2: Drawing of setup for behavior of directional coupled circular resonator with embedded emitter.

The problem setup is very similar to the simple transmission case, but now we account for the emitter with b_3:

$$b_3 = b_2 + 1 \tag{A.42}$$

$$b_1 = \gamma e^{i\theta} b_3 \tag{A.43}$$

From equations (28) and (43), and setting $a_1 = 0$ for no input power, we can obtain:

$$a_2 = e^{i\phi}\left(\frac{i\kappa\gamma}{e^{-i(\theta+\phi)} - t\gamma}\right) \tag{A.44}$$

and thus an expression for power out-coupling:

$$P_{out} = |a_2|^2 = \frac{\kappa^2\gamma^2}{1 + t^2\gamma^2 - 2t\gamma cos(\theta+\phi)} \tag{A.45}$$

On resonance ($\theta + \phi = 2m\pi$), we have:

$$P_{out,res} = |a_2|^2_{res} = \frac{\kappa^2\gamma^2}{(1-t\gamma)^2} \tag{A.46}$$

Appendix B

DETAILED FABRICATION RECIPES

B.1 GaP Membrane Preparation

1. Begin with epitaxial GaP-on-AlGaP.

2. Clean. **Do not allow solvents to dry on surface.**

   (a) Sonicate in acetone for 5 minutes.

   (b) Soak in IPA for 5 minutes.

   (c) Rinse with DI water and immediately blow dry with N_2.

3. Lithography.

   (a) Bake on hotplate at 110 °C for 5 minutes.

   (b) Spin coat AZ1512 resist (2 s ramp to 500 rpm and hold for 5 s; 3 s ramp to 5500 rpm and hold for 40 s).

   (c) Softbake on hotplate 1t 110 °C for 60 s.

   (d) (Optional) Cleave into pieces for different membrane patterns.

   (e) Expose membrane pattern using ABM aligner for 4 s. Use a silicon backing wafer under the GaP piece, and use alignment microscope to align corners of GaP piece to mask pattern.

   (f) Develop exposed pattern in 1:4 AZ340:H_2O (60 s).

   (g) De-scum in barrel etcher (75 W, 120 s).

   (h) Use alpha-step to measure resist thickness. It should be $\sim$1 μm.

4. Cleave into single-membrane pieces.

5. Etch in Oxford Chlorine ICP-RIE tool, using recipe "NT_Thin_GaP_Etch/Strike/R"

   (a) Run recipe for 15 minutes on bare carrier wafer or clean dummy wafer to condition chamber.

   (b) Run recipe on selected GaP pieces for 40 s.

   (c) Allow system to return samples to load-lock.

   (d) Repeat 40 s etch and return to loadlock twice (total 3 $\times$ 40 s etching).

6. Final checks:

   (a) Use alpha-step to measure etch depth. Total step size (resist thickness + etch depth) should be $\sim$2.2 μm.

   (b) Examine under optical microscope.

B.2 GaP Membrane Transfer to Diamond

1. Begin with prepared GaP membrane(s) (see Section B.1) and implanted/annealed diamond chip(s). Image diamond chip(s) face-up for later reference.

2. Place GaP piece into dilute HF.

   (a) Prepare 1.5% dilution of HF in HF-safe dish **(NOT glass)**. Make sure dish is large enough and liquid-level is high enough to submerge PTFE bucket tool.

   (b) Using HF-safe tweezers (plastic or coated), place GaP piece face-up in bottom of HF dish.

   (c) Lift-off typically takes $\sim$1 hour.

3. Prepare diamond

(a) Scrub with cleanroom wipes, using acetone, IPA, water in order to remove macroscopic dirt.

(b) Place diamond chip(s) face-up in 96% H_2SO_4.

(c) Heat to fuming (200 °C hotplate).

(d) Add 1 g KNO_3 per 20 mL of H_2SO_4.

(e) Wait 10-15 minutes before turning off hotplate.

(f) Turn off hotplate, and allow cleaning solution to cool.

(g) Carefully transfer diamond into water rinse dish.

(h) N_2 blow-dry.

(i) HMDS treatment in automated oven.

4. Transfer membrane.

(a) After 1 hour of soaking in HF solution, bring GaP pieces to surface and resubmerge. This will typically release the GaP membrane.

(b) Allow membrane to float at surface of HF solution for ∼5 minutes to remove any remaining AlGaP.

(c) Use PTFE bucket tool to capture membrane with a small amount of HF solution, and transfer to water dish.

(d) With diamond chip clamped into bottom of aluminum bucket tool, use tool to capture membrane from water dish.

(e) Carefully drain as much water from tool by removing it from water dish.

(f) Use cleanroom wipes to wick away remaining water.

(g) Remove diamond chip from bucket tool, and place under microscope with full illumination power to dry any stray water droplets.

5. Final checks:

   (a) Examine under optical microscope.

   (b) Place in double-membrane box (with cleanroom wipes) for at least 48 hours prior to further processing.

B.3 GaP-on-Diamond Photonics Process

1. Begin with prepared GaP-on-diamond chip (see Section B.2).

2. Remove AZ1512 resist from GaP.

   (a) Heat dish of EKC-830 resist remover on hotplate at 80 °C.

   (b) Place GaP-on-diamond chip in EKC for 20 minutes. **Use metal tweezers**.

   (c) Agitate chip (move it around) with tweezers every 5 minutes.

   (d) Rinse with IPA and N_2 blow-dry.

3. Electron-beam lithography.

   (a) Evaporate 5 nm SiO_2 for HSQ adhesion. Use electron-beam evaporator (PECVD changes charge state of implanted NV centers).

   (b) 5 minutes on hotplate at 150 °C.

   (c) Spin 6% HSQ solution (1 s ramp to 500 rpm and hold for 1 s, 1 s ramp to 7500 rpm and hold for 45 s). Try to center GaP membrane on spindle.

   (d) Softbake at 80 ° for 4 minutes.

   (e) Expose pattern in JEOL JBX-6300FS with dose of 2350 $\mu C/cm^2$. Make sure to use appropriate proximity correction in pattern file preparation.

   (f) Develop pattern in 25% TMAH solution for 4 minutes.

   (g) Rinse in de-ionized water with some agitation. Optionally follow with IPA rinse.

(h) N_2 blow-dry.

4. Etch.

   (a) **Check developed pattern in SEM before etching GaP**.

   (b) Etch GaP in Oxford Instruments Chlorine ICP-RIE tool. Use automated recipe "MAG_GaP_Etch" (Recipe 6 from Chapter 2). DC voltage should be ∼235 V during etch.

   (c) **Check GaP etch in SEM before etching diamond**.

   (d) Etch diamond in Oxford Instruments Chlorine ICP-RIE tool. Use automated recipe "NT_Diamond_Etch". DC voltage should be ∼65 V during etch.

5. Final checks:

   (a) Examine under optical microscope.

   (b) Examine under SEM

   (c) Place in Gelpak for transport to lab!

Appendix C

POLARIZATION HYBRIDIZATION IN DISKS

Under the experimental configuration used for waveguide-coupled single photon measurements (see Fig. 5.1(a)), it is possible to determine the polarization character (TE vs. TM) of linearly-polarized resonator modes using the collection-path polarizer on the microscope. As an example, Fig. C.1 shows background emission measurements taken on a 650-nm-radius disk resonator on the initial device chip (see Section 3.1). With no polarization optics in the collection path, a grating-collected spectrum shows the presence of two resonator modes. However when a linear polarizer is placed in the collection path, transmission of either mode can be blocked with the appropriate polarizer angle. Moreover, the angles of maximum extinction were very close to 0° and 90° with respect to the grating coupler, indicating the TE/TM nature of the resonator modes. Note that grating couplers on the initial device chip performed quite poorly, but showed comparable off-chip coupling efficiencies for both TE and TM waveguide modes.

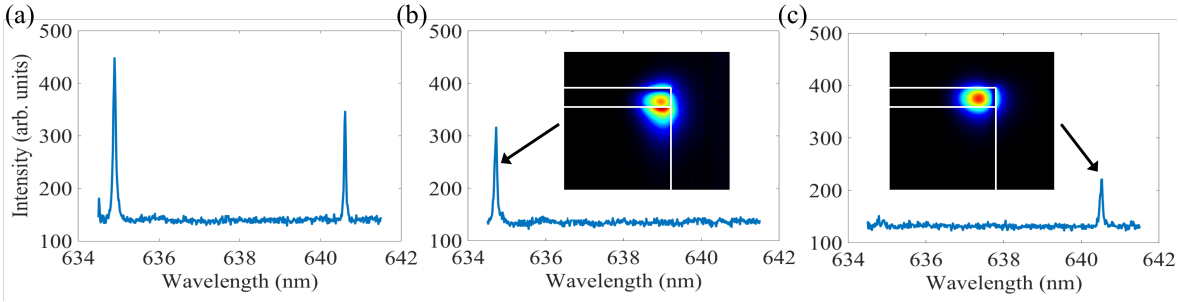

Figure C.1: Grating-collected PL from a 650-nm-radius disk resonator from the initial device chip. (a) Un-polarized. (b) TM-polarized. (c) TE-polarized. Insets show dominant electric field component distributions for the two disk modes.

In contrast to the 650-nm-radius disks, disks with radii around ∼430 nm exhibit grating-collected resonator modes that cannot be well blocked with a linear polarizer. This is in reasonable agreement with simulations of resonator mode index vs. disk radius, which show an anti-crossing between the TE and TM modes occurring for disk radii between ∼375 nm and ∼450 nm. Eigenmodes in the anti-crossing region have hybrid polarization character, meaning that they have both TE and TM field components. While these modes are linearly polarized within the resonator, each of them couples to both TE and TM modes in the bus waveguide. TE and TM waveguide modes have different propagation constants. As a result, the output from the grating coupler will generally be elliptically polarized, resulting in free-space modes that cannot be well blocked with a linear polarizer. Fig. C.2 shows a top-collected spectrum from a 438-nm-radius disk, as well as a TE-polarized grating-collected spectrum. Where in larger devices one of the modes would undergo a large extinction, here both modes are transmitted.

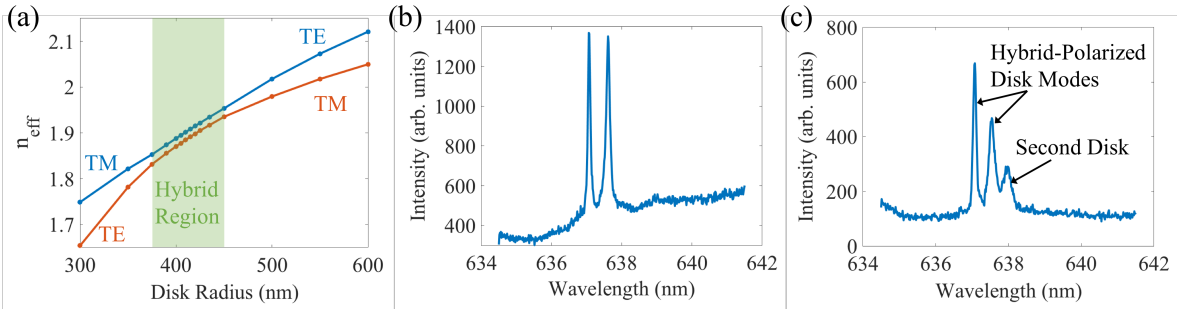

Figure C.2: (a) Simulated effective indices for resonator modes as a function of disk radius showing an anti-crossing between ∼375 nm and ∼450 nm. (b) Spectrum collected directly from a 438-nm-radius disk showing two modes. (c) TE-polarized grating-collected spectrum taken while exciting the same disk, showing both modes. A third mode is likely from an adjacent disk coupled to the same waveguide.

This effect is primarily of interest as something to be avoided in the single-emitter devices, effectively setting a minimum radius for disks somewhere near ∼500 nm. Although hybrid-polarization disk modes can couple to single NV centers, it is generally good practice to pick

either TE or TM polarization for all component device designs in order to simplify the design of larger circuits. However, there may be some applications for hybrid-polarization devices for on-chip polarization control.

Appendix D

RF TRANSMISSION LINE CAVITIES FOR MAGNETOMETRY

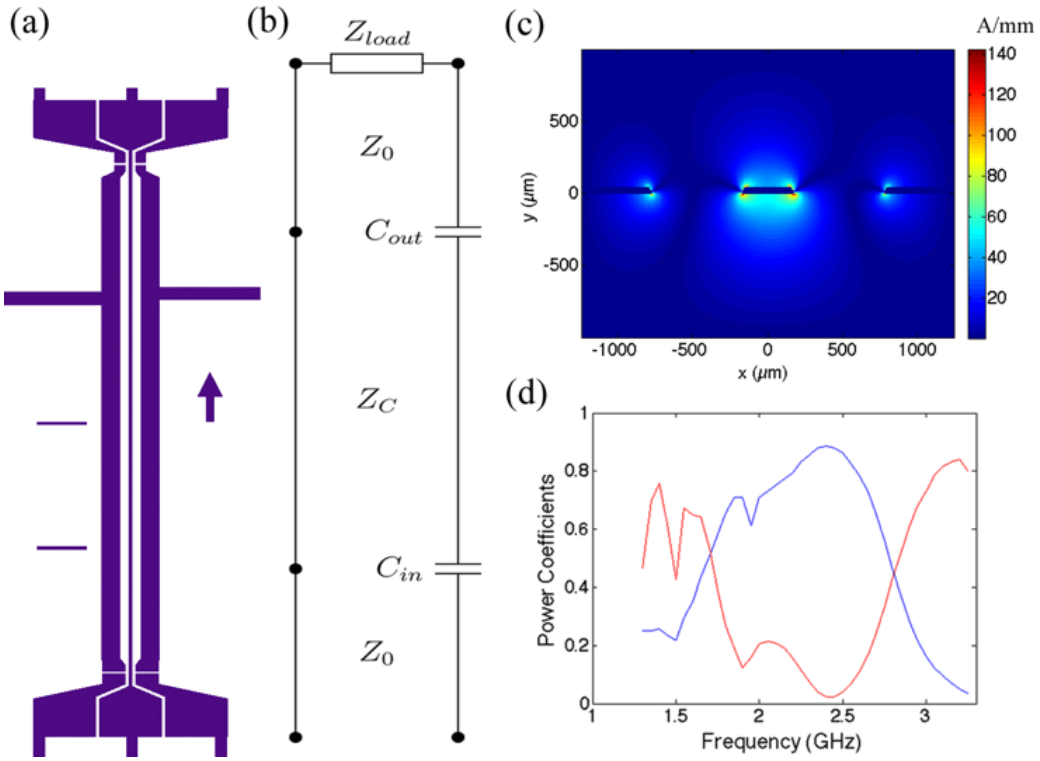

Figure D.1: (a) Scaled top view of fabricated RF cavity. (b) Transmission line model of cavity. (c) Spatial distribution of H_x for cavity transmission line mode. (d) Measured power transmission (blue curve) and reflection (red curve) for cavity.

The cavities were designed as sections of transmission line with capacitive in-coupling and out-coupling, as shown in Fig. D.1. Unfortunately, the first round of RF cavities provided performance comparable to the simple transmission line described in Section 8.2. The

primary reason for this was that simulations were performed with an assumed relative permittivity of 6 for the soda-lime glass substrate. However, measurements suggest a considerably higher value of permittivity around 12, based on both lower-than-expected quality factor, and lower-than-expected resonant frequency. The higher-than-expected permittivity resulted in higher-than-expected capacitive coupling at the ends of the cavity, ultimately resulting in a considerably lower-than-designed quality factor of $\sim$5. Measured transmission and reflection spectra are shown in Fig. D.1(d). The main resonance appears to be at $\sim$2.45 GHz. We suspect the lower-frequency resonance seen at $\sim$1.9 GHz is due to a parallel transmission line mode supported between the signal line of the coplanar structure and the metal holder.

The measured quality factor of 5 corresponds to a magnetic field enhancement of only $\sim$1.8. Given the reduced field strength for the cavity transmission line mode with respect to the simple transmission line due to a wider signal line (Fig. D.1(c)), the expected field seen by NV centers is only 44 A/mm for 1 W of input RF power. NV centers on the simple transmission line are expected to see 48 A/mm. This is in good agreement with the comparable performance seen in ODMR experiments. Based on what was learned from the first round of devices, we expect future RF cavities to achieve field enhancements larger than a factor of 4 with respect to the simple line, while maintaining a broad operating bandwidth of $\sim$100 MHz.